



Technische Universität München
Fakultät für Physik

Abschlussarbeit im Masterstudiengang Physik

SIMULATION OF ANYON DYNAMICS

Simulation der Dynamik von Anyonen

Nico Kirchner

16. November 2021

Erstgutachter: Prof. Dr. Frank Pollmann

Zweitgutachter: Prof. Dr. Michael Knap

Abstract

The field of quantum computing has been one of the most aspiring research areas in physics in recent years. Especially the potential possibility of constructing fault-tolerant quantum computers by using non-abelian anyons is of major interest.

Even apart from the quantum computational context, non-abelian anyons are studied. However, it turns out that there is currently no known numerical method that can be used in order to examine the dynamics of non-abelian anyons if all of them are to move freely on a lattice. In this thesis, we will thus present a newly developed algorithm that is capable of simulating arbitrary abelian and non-abelian anyon models on a lattice, where the anyons move according to a tight-binding Hamiltonian that only accounts for their statistics.

In order to achieve the above goal, we first briefly review already known algorithms for simulating abelian anyons both on a lattice and in continuous space. After introducing the basic formalism of anyon models, the new, generalized algorithm is discussed, where we also touch upon the construction of momentum states.

Using the above methods for semions and Fibonacci anyons, we study the thermalization and relaxation behavior. For the former, the energy level spacings are examined, which reveals Wigner-Dyson statistics. For the relaxation behavior, the density distribution following a quench is studied, which shows relaxation to a homogeneous density distribution. These results suggest that thermalization is present in both of the anyonic systems.

Finally, the threshold behavior of the spectral function for semions is studied for long-range interactions. It is revealed that for fast decaying interactions, the threshold behavior remains unaffected. For slowly decaying interactions however, it is changed. For the critical decay that separates these two regimes, the change in the threshold behavior is also non-zero and can be computed analytically. It is further shown that for slowly decaying interactions and small enough interaction strengths, the non-interacting expectation is recovered within a certain energy range.

Lastly, we study the spectral function for non-interacting Fibonacci anyons and relate the distribution of the wave function components to the observed threshold behavior.

Zusammenfassung

Quantum Computing gehört schon seit einigen Jahren zu den aufstrebendsten Forschungsgebieten in der Physik. Vor allem die potentielle Möglichkeit der Konstruktion von fehlertoleranten Quantencomputern durch die Nutzung von nichtabelschen Anyonen ist von großem Interesse. Aber auch abseits von diesem Kontext werden nichtabelsche Anyonen studiert. Es stellt sich jedoch heraus, dass es aktuell keinen bekannten Algorithmus gibt, mit dem man die Dynamik von nichtabelschen Anyonen untersuchen kann, wenn sich diese frei auf einem Gitter bewegen sollen. Aus diesem Grund werden wir in dieser Arbeit einen neu entwickelten Algorithmus vorstellen, der beliebige abelsche und nichtabelsche Anyon-Modelle simulieren kann, wobei sich die Anyonen gemäß eines tight-binding Hamiltonians bewegen, welcher ausschließlich die anyonische Statistik berücksichtigt.

Um das genannte Ziel zu erreichen, stellen wir zuerst bereits bekannte Algorithmen, mit denen abelsche Anyonen auf einem Gitter und im kontinuierlichen Raum simuliert werden können, vor. Nachdem der Formalismus zur Beschreibung von Anyon-Modellen eingeführt wurde, wird der neue, verallgemeinerte Algorithmus diskutiert, wobei wir auch auf die Konstruktion von Impulszuständen eingehen.

Mit diesen Methoden wird die Thermalisierung und das Relaxationsverhalten von Semionen und Fibonacci-Anyonen studiert. Für Ersteres wird die statistische Verteilung der Abstände aufeinanderfolgender Energien des Hamiltonians untersucht, was eine Wigner-Dyson-Statistik offenbart. Für das Relaxationsverhalten wird die Dichteverteilung nach einem Quench untersucht, welche zu einer homogenen Verteilung relaxiert. Diese Ergebnisse deuten auf Thermalisierung in beiden anyonischen Systemen hin.

Anschließend wird noch das Threshold-Verhalten der Spektralfunktion für Semionen mit langreichweitigen Wechselwirkungen untersucht. Es zeigt sich, dass das Threshold-Verhalten für schnell abfallende Wechselwirkungen nicht beeinflusst wird. Für langsam abfallende Wechselwirkungen wird es hingegen verändert. Für die kritisch abklingenden Wechselwirkungen, die die anderen zwei Bereiche trennen, wird das Threshold-Verhalten ebenfalls beeinflusst, wobei die Änderung analytisch berechnet werden kann. Es wird außerdem gezeigt, dass sich selbst für langsam abklingende Wechselwirkungen Energiebereiche finden lassen, in denen das für nicht-wechselwirkende Teilchen erwartete Verhalten wiedergefunden werden kann, falls die Wechselwirkungsstärke nicht zu stark ist.

Zum Schluss betrachten wir noch die Spektralfunktion von nicht-wechselwirkenden Fibonacci-Anyonen und erklären, wie die Verteilung der Wellenfunktionskomponenten das Threshold-Verhalten beeinflussen.

Acknowledgements

I would like to express my gratitude to Professor Frank Pollmann and Dr. Adam Smith for giving me the chance to persue the topic of this thesis. Without their guidance, their constructive feedback and all the fruitful discussions we had, this work would not have been possible.

I would also like to thank my family and my friends for their unconditional support and encouragement during this entire time.

Contents

Abstract	i
Zusammenfassung	ii
Acknowledgements	iii
1. Introduction	1
2. Simulations for Abelian Anyons	3
2.1. Lattice Simulations for Abelian Anyons	3
2.1.1. The Braid Group	3
2.1.2. Simulation Algorithm	5
2.1.3. Momentum States	7
2.2. Adding Interactions	10
2.3. Continuous Simulations from Differential Equations	12
3. Basic Formalism for Anyon Models	15
3.1. Basic Properties	15
3.2. Fusion Diagrams: Basis States	18
3.3. The Semion and Fibonacci Anyon Model	21
4. Lattice Simulations for Non-abelian Anyons	22
4.1. Preparatory Considerations	22
4.2. The Algorithm	25
4.2.1. Translations in the Bulk	26
4.2.2. Translations over the Cuts	28
5. Thermalization of Anyons	35
5.1. Energy Level Spacing Statistics	35
5.2. Quench Dynamics	37
6. The Spectral Function	42
6.1. Definition and Basic Properties	42
6.2. The Effect of Interactions on the Spectral Function's Threshold Behavior	47
6.2.1. The Case $\epsilon = 0$	47
6.2.2. The Case $\epsilon > 0$	48
6.2.3. The Case $\epsilon < 0$	52

6.3. Fibonacci Anyons	57
7. Conclusion	60
A. Momentum States for the Generalized Algorithm	62
A.1. Momentum States in x -Direction	62
A.2. Momentum States in x - and y -Direction	66
B. Equivalence of the Generalized Algorithm to the Algorithm in Section 2.1 for Abelian Anyons	72
C. Derivation of Equation (6.9)	76
D. Changes in the Asymptotic Behavior Due to Interactions of the Form $U/r^{2+\epsilon}$	78
List of Figures	80
References	83

1. Introduction

One of the most fundamental properties of particles in quantum mechanics is that upon exchanging two identical (point-like) particles, the wave function describing these particles acquires a phase $e^{i\theta}$. It is well-known that for three-dimensional (3D) systems, these phases are restricted to $\theta = 0$ and $\theta = \pi$, corresponding to bosons and fermions, respectively. Two-dimensional (2D) systems on the other hand may feature quasiparticle excitations, so-called anyons, that obey more complex fractional exchange statistics that are classified by the representations of the braid group [1]. The braid group itself consists of elements that correspond to possibly multiple, successive, clockwise or counter-clockwise exchanges of these particles [2]. If the braid group can be represented such that upon exchanging two anyons the wave function simply gains a phase $e^{i\theta}$, i.e., the representation is one-dimensional (1D), the anyons are referred to as being abelian [1, 2]. If the latter is not the case, the system features non-abelian anyons [1].

These non-abelian anyons are of special interest in quantum computing since they might be used in order to create a fault-tolerant topological quantum computer [1, 3–5]. One of the most prominently studied non-abelian anyons in this field are the so-called Fibonacci anyons [3, 6–8] that are actually universal for quantum computing [9].

Even when focusing on the anyons themselves, rather than on their potential usage for quantum computing, it is found that the field of interacting anyonic quantum systems is an active area of research [7, 10–15]. However, there are only comparably few simulations that exclusively focus on the dynamics/properties of 2D anyonic systems that are solely governed by their statistics. Examples include lattice simulations of abelian anyons on a torus or an annulus, where the Hamiltonian of the system is given by a tight-binding Hamiltonian that only accounts for the anyonic exchange statistics [16–18]. In other work, matrix product states were used to simulate essentially the same Hamiltonian for quasi-1D systems, where the anyons were also allowed to be non-abelian and only one anyon was mobile [19]. From the restrictions in these examples, it is apparent that there is a need to develop a new, intuitive algorithm that allows to simulate non-abelian anyons on a general 2D lattice with multiple mobile anyons. By choosing the simulated Hamiltonian to be the corresponding anyonic tight-binding Hamiltonian that incorporates the anyons' statistics and imposing periodic boundary conditions (PBC), this new algorithm can be thought of as a generalization of the algorithm that simulates abelian anyons on a torus [17].

The construction of such a generalized algorithm is the main goal of this thesis. It will be presented together with some simulation results including energy level spacing statistics, quench dynamics and examinations of the spectral function's threshold behavior.

The thesis is structured as follows. First, we review already existing numerical methods in section 2. These include the above mentioned algorithm [17] for simulating abelian anyons that

are governed by a tight-binding Hamiltonian on a 2D periodic lattice (section 2.1), a method to efficiently compute long-range interactions in lattice simulations (section 2.2) and the usage of differential equations in order to obtain continuous simulations of abelian anyons (section 2.3). Then, in section 3, we briefly review the formalism that is used to describe anyon models and introduce the models to be studied later on. In section 4, the newly developed, generalized algorithm is discussed. A technical discussion about the construction of momentum states can be found in appendix A. Further, we prove in appendix B that the generalized algorithm reproduces the algorithm for abelian anyons when choosing the appropriate anyon model, i.e., it is indeed a generalization.

With all these considerations, we are able to simulate (non-)interacting abelian and non-abelian anyons on a lattice, which may be complemented for abelian anyons with continuous simulations. In section 5, first simulation results for anyons on lattices are discussed, where our main focus are the energy level statistics and the time-dependent density distribution after a quench for both semions and Fibonacci anyons in order to see the thermalization and relaxation behavior. For this purpose, the lattice was taken to be a 2D ladder with two rows.

In section 6.1, we introduce the final quantity to be studied using both the lattice and the continuous simulations: the spectral function. Knowing that the threshold behavior depends on the statistics for abelian anyons [20], we examine two things. Firstly, the effect of long-range interactions on the threshold behavior for abelian anyons (especially semions) and fermions is studied in section 6.2, where it is found that there are three cases to be distinguished. The two appendices C and D contain some calculations that are of importance for this part but harm the text flow. Secondly, in section 6.3, we take a look at the spectral function for Fibonacci anyons and analyze its threshold behavior, where it should be noted that for Fibonacci anyons, there are currently no predictions for the spectral function's behavior close to the threshold. The thesis is closed in section 7 with a summary of the most important insights and an outlook on potential future projects of interest.

2. Simulations for Abelian Anyons

Following [17] and [21], we first discuss some basic aspects of the braid group for anyons. Using these insights, a known algorithm for simulating abelian anyons on periodic lattices based on [17] and partly [18] is presented, where we also address its limitations. After that, we also touch upon an efficient way to compute two-body interactions on periodic lattices, which can in fact also be used for the generalized algorithm that is presented later in section 4.

Finally, we briefly discuss continuous simulations for a pair of anyons that are obtained by numerically solving differential equations. While this part has no apparent connection to the discrete lattice simulations, it will turn out to be very useful for the discussion of the spectral function's threshold behavior in section 6.2, as it complements the lattice simulations.

2.1. Lattice Simulations for Abelian Anyons

In this section, the primary objective is to mainly follow Ref. [17] and present the algorithm therein, which simulates abelian anyons on a 2D lattice with PBC and is applicable to multiple anyons of the same charge. The simulated Hamiltonian corresponds to a tight-binding Hamiltonian that accounts for the anyons' statistics. We note that the algorithm discussed in [18] is very similar but focused on semions, whereas [17] allows general abelian anyons. We therefore follow the latter. In the former, however, the construction of momentum states is discussed, which will be adapted in order to construct momentum states for the other (slightly different and more general) algorithm.

2.1.1. The Braid Group

To start, we take a closer look at the braid group, following both [17] and [21]. The braid group of the torus for N identical particles $B_N(\mathcal{T})$ consists of elements corresponding to exchanges between the particles. These exchanges may be clockwise or anti-clockwise and an element may correspond to a chain of successive exchanges [2]. An anti-clockwise exchange is illustrated in Fig. 2.1, which is based on similar depictions found in [17] and [21]. The corresponding operation that exchanges particles i and $i + 1$ is denoted by the operator $\tilde{\sigma}_i$, where no particles are localized within the region defined by the trajectories of the two particles to be exchanged and $i \in \{1, 2, \dots, N - 1\}$. Clockwise exchanges correspond to inverse counter-clockwise exchanges and are thus denoted by $\tilde{\sigma}_i^{-1}$. Here, we assumed that the particles in the system are numbered from 1 to N .

It turns out that due to PBC, there are additional operations besides direct exchanges of two particles: On an annulus for example, the particles can also be translated around in the periodic

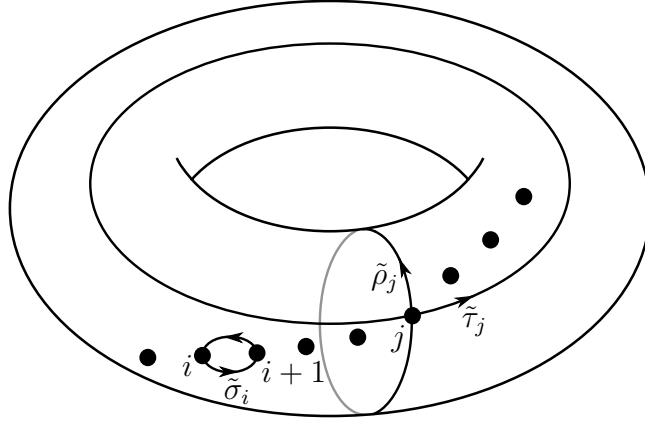


Figure 2.1.: Generators $\tilde{\sigma}_i$, $\tilde{\rho}_j$ and $\tilde{\tau}_j$ of $B_N(\mathcal{T})$. The particles are numbered from the left to the right.

direction, i.e., along a closed, non-contractible loop such that their initial and final positions are identical [16]. In our case, i.e., on the torus, the particles can be translated like this in both directions, which is also depicted in Fig. 2.1. $\tilde{\rho}_j$ and $\tilde{\tau}_j$ ($j \in \{1, 2, \dots, N\}$) translate the j -th particle along the (periodic) y - and x -direction such that its final position agrees with its initial one without exchanging any particles on the way. The operators $\tilde{\sigma}_i$, $\tilde{\rho}_j$ and $\tilde{\tau}_j$ together generate the braid group $B_N(\mathcal{T})$.

Some of the most important relations involving the above operators are

$$\tilde{\sigma}_i \tilde{\sigma}_j = \tilde{\sigma}_j \tilde{\sigma}_i, \quad |i - j| \geq 2, \quad (2.1)$$

$$\tilde{\sigma}_i \tilde{\sigma}_{i+1} \tilde{\sigma}_i = \tilde{\sigma}_{i+1} \tilde{\sigma}_i \tilde{\sigma}_{i+1}, \quad (2.2)$$

$$\tilde{\rho}_{i+1} = \tilde{\sigma}_i \tilde{\rho}_i \tilde{\sigma}_i \quad \text{and} \quad (2.3)$$

$$\tilde{\tau}_{i+1} = \tilde{\sigma}_i^{-1} \tilde{\tau}_i \tilde{\sigma}_i^{-1}, \quad (2.4)$$

where $i, j \in \{1, 2, \dots, N - 1\}$ and $i \neq N - 1$ for (2.2).

By deciding to restrict ourselves to abelian anyons, we can choose

$$\sigma_i = e^{i\theta} \mathbb{1}_M \quad (2.5)$$

to be the M -dimensional representation of $\tilde{\sigma}_i$, where $\mathbb{1}_M$ refers to the $M \times M$ identity matrix. Each of these M dimensions corresponds to a different component of the anyonic wave functions. The choice for σ_i implies for the representations ρ_j and τ_j of $\tilde{\rho}_j$ and $\tilde{\tau}_j$ that $\rho_j = \rho_1 e^{i2\theta(j-1)}$ and $\tau_j = \tau_1 e^{-i2\theta(j-1)}$ has to hold. Furthermore, it can be shown that

$$\tau_i \rho_j = \rho_j \tau_i e^{i2\theta(1-N\delta_{ij})}, \quad (2.6)$$

which implies when looking at the determinant for $i \neq j$ that

$$e^{i2\theta M} = 1. \quad (2.7)$$

I.e., for an irreducible, M -dimensional representation, θ , which is also known as the topological spin of the anyons [22], can be written as $\theta = \pi p/M$, with p and M being coprime integers. Another constraint is obtained by considering (2.3) and (2.4) together with (2.6):

$$e^{i2\theta N} = 1. \quad (2.8)$$

This restricts the total number N of anyons that can exist on the torus to $N = kM$ with $k \in \mathbb{N}$. Finally, one can choose ρ_1 and τ_1 to be

$$\rho_1 = e^{i2\pi\Phi_y/\phi_0} \begin{pmatrix} 1 & & & \\ & e^{i2\theta} & & \\ & & \ddots & \\ & & & e^{i2\theta(M-1)} \end{pmatrix} \quad \text{and} \quad \tau_1 = e^{i2\pi\Phi_x/\phi_0} \begin{pmatrix} 0 & 1 & & \\ \vdots & 0 & \ddots & \\ 0 & & \ddots & 1 \\ 1 & 0 & \dots & 0 \end{pmatrix}, \quad (2.9)$$

all other ρ_j and τ_j are fixed by (2.3) and (2.4). For completeness, in (2.9), we also introduced fluxes in x - and y -direction, Φ_x and Φ_y ; $\phi_0 = hc/e$ denotes the flux quantum. However, as we are not interested in any flux sectors, we will henceforth set $\Phi_x = \Phi_y = 0$.

2.1.2. Simulation Algorithm

With this background, let us review the algorithm from Ref. [17]. The goal is to simulate the anyonic tight-binding Hamiltonian

$$H = - \sum_{\langle i,j \rangle} e^{i\theta_{ij}} c_j^\dagger c_i + \text{H.c.}, \quad (2.10)$$

where the creation and annihilation operators for site i , c_i^\dagger and c_i , fulfil the same relations as the respective operators for HCBs, i.e.

$$\{c_i^\dagger, c_i^\dagger\} = 1 = \{c_i, c_i^\dagger\} \quad \text{and} \quad (2.11)$$

$$[c_i^\dagger, c_j^\dagger] = 0 = [c_i, c_j], \quad i \neq j. \quad (2.12)$$

The sum in (2.10) runs over all nearest neighboring pairs and θ_{ij} is associated to the connection from site i to site j . The order for the latter is important as $\theta_{ij} = -\theta_{ji}$. These phases are used in order to encode the anyons' statistics and are determined by the "string rules" that are introduced below.

Let us choose a basis of the Hilbert space in order to simplify this discussion. An intuitive choice is to take basis states for which each of the N anyons is localized at some site:

$$|\{\mathbf{r}_1, \mathbf{r}_2, \dots, \mathbf{r}_N\}, m\rangle, \quad (2.13)$$

where \mathbf{r}_i is the location of the i -th anyon. The order in which all the \mathbf{r}_i appear in (2.13) is of no importance. For each anyon configuration, there are in general multiple states with different wave function components labeled by m , with $m \in \{1, 2, \dots, M\}$. States with different wave

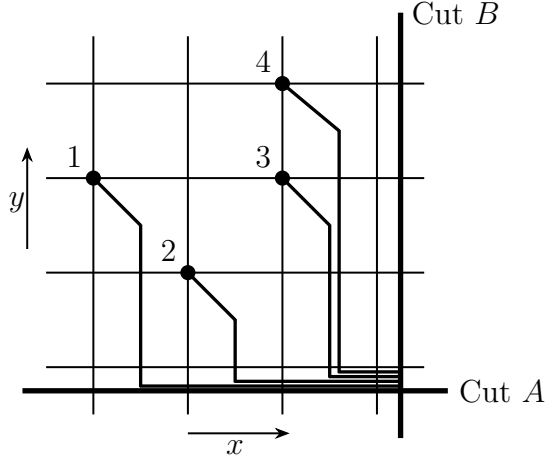


Figure 2.2.: Choice of cuts A and B on a lattice containing four anyons numbered from one to four. The phases associated to the anyons' strings are θ for the vertical and 2θ for the horizontal parts.

function components are orthogonal.

Using this basis, the string rules can be explained via the action of H on the basis states. Each anyon located on the lattice has a string that carries phases associated to it such that every time a string is crossed by an anyon, the wave function acquires a (non-trivial) phase given by this string. The strings are chosen to originate from the anyons, going into the plaquettes on the lower right of the anyons' sites and then follow the negative y -direction until they almost reach cut A that is given by the condition $y = 1/2$. Then, the strings follow the positive x -direction, ending when reaching cut B , which is given by $x = L_x + 1/2$. Examples for these strings are given in Fig. 2.2. The phases associated to the vertical parts of the strings are θ , the ones associated to the horizontal parts are 2θ . If multiple anyons are located in the same column, the x -coordinate corresponding to the vertical part of the string is larger for the string associated to the anyon located at the site with the larger y -coordinate, as can be seen for particles 3 and 4 in Fig. 2.2. This will be important later on. As for the horizontal strings, one can either choose to employ a similar rule, like in [18], or let them exist on top of each other, like in [17]. We chose the former convention, which is also illustrated in the above figure.

With this, θ_{ij} can be determined by considering all the different scenarios that can occur one after another. If an anyon is translated in y -direction without crossing cut A (e.g., if anyon 1 in Fig. 2.2 is translated in y -direction), the corresponding phase is trivial, $\theta_{ij} = 0$, as no string is crossed.

If an anyon crosses a vertical string when hopping in positive x -direction without crossing cut B (e.g., anyon 3 in Fig. 2.2 is translated), the wave function acquires a phase of $e^{i\theta}$. If this happens when an anyon is hopping in negative x -direction (e.g., for translating anyon 2 in Fig. 2.2), the corresponding phase is $e^{-i\theta}$. If a vertical string sweeps an anyon, the wave function gains the same phase as if the anyon would be moving across the string. This means that if an anyon moves in positive x -direction and its string sweeps another anyon on the way (e.g., for translating anyon 1 in Fig. 2.2), a phase of $e^{-i\theta}$ is acquired. The other direction corresponds to

a phase of $e^{i\theta}$ (e.g., anyon 4 in Fig. 2.2 is translated in negative x -direction).

If an anyon is translated across cut B in positive x -direction, τ_j has to be applied, i.e., the component m of the wave function is changed to $m - 1 \bmod M$, as can be seen from (2.9). While (2.4) is fulfilled due to the vertical strings, we have to add an additional phase of $e^{-i\theta(N-1)}$ in order to obtain the phase for τ_1 that we defined in (2.9). If cut B is crossed in the opposite direction, the wave function component is increased by one and $e^{i\theta(N-1)}$ is acquired as additional phase.

Finally, when hopping in positive y -direction over cut A , the wave function gains a phase of $e^{i2\theta}$ for each horizontal string that is crossed. In addition to that, ρ_j has to be applied, i.e., an additional phase of $e^{i2\theta(m-1)}$ is acquired, where m is again the component of the wave function. In this process, m remains unchanged. A further phase of $e^{i\theta N_c}$ is gained due to anyons located in the same column as the one crossing cut A , where N_c corresponds to the total number of anyons in the same column (i.e., with the same x -coordinate) as the anyon moving across the cut, without counting the translated anyon itself. This can be interpreted as a phase that is acquired in the process of bringing the strings back to their conventional order, as can be seen when translating anyon 4 in Fig. 2.2 over cut A : Due to the x -coordinates of the strings' vertical components not changing upon crossing the cut, the strings after the translation are not in the conventional order. In the process of exchanging the vertical components to restore this order, a phase of $e^{i\theta}$ is gained for each time two strings are exchanged.

When passing cut A in negative y -direction, the above phases have to be complex conjugated. This concludes the algorithm for simulating abelian anyons described in [17].

2.1.3. Momentum States

It is possible to exploit the translation invariance of H to construct a momentum state basis, as done in [18] for semions, which will be partly adapted here. In order to do this, one simply has to superpose all possible translations of a state $|\{\mathbf{r}_1, \mathbf{r}_2, \dots, \mathbf{r}_N\}, m\rangle$ and apply the discussed rules to the translation processes. I.e., the momentum states are given by

$$|\psi_{k_x, k_y}\rangle \equiv \frac{1}{\sqrt{\mathcal{N}}} \sum_{j=0}^{L_x-1} \sum_{n=0}^{L_y-1} e^{i(jk_x + nk_y)} \tilde{T}_x^j \tilde{T}_y^n |\psi\rangle \quad (2.14)$$

$$\equiv \frac{1}{\sqrt{\mathcal{N}}} \sum_{j=0}^{L_x-1} \sum_{n=0}^{L_y-1} e^{i(jk_x + nk_y)} e^{i\theta(N_c(n) + 2N_l(n))} (e^{-i\theta(N-1)} \tau_1)^{N_x(j)} \rho_1^{N_y(n)} T_x^j T_y^n |\psi\rangle, \quad (2.15)$$

where \mathcal{N} assures normalization. $|\psi_{k_x, k_y}\rangle$ is the constructed momentum state and $|\psi\rangle$ a state like $|\{\mathbf{r}_1, \mathbf{r}_2, \dots, \mathbf{r}_N\}, m\rangle$. \tilde{T}_x and \tilde{T}_y translate all anyons in positive x - and y -direction, respectively, adding phases and changing the wave function components according to the discussed string rules. These two operators can be rewritten using T_x and T_y , which translate all anyons in the respective directions without adding any phases or changing the wave function component; the acquired phases are then written explicitly in terms of the matrices τ_1 , ρ_1 and additional parameters. $N_x(j)$ ($N_y(n)$) corresponds to the number of anyons that cross cut B (cut A) when applying T_x^j (T_y^n) onto $|\psi\rangle$. $N_c(n)$ counts the total number of anyons in the same column as the

anyons that cross cut A when applying T_y^n . $N_l(n)$ counts the total number of anyons on the left of these very anyons for the same process. For $N_l(n)$, it is important to note that in (2.15), T_y^n is applied before T_x^j such that $N_l(n)$ does not depend on j . All these newly introduced properties together apply the string rules discussed above.

It is straight forward to see that $[\tilde{T}_x, \tilde{T}_y] = 0$ by considering all cases that can occur. First of all, it is to be realized that the only non-trivial scenario is the one in which anyons are translated across both cuts when applying \tilde{T}_x and \tilde{T}_y . For the other cases, the commutator vanishes since one or both operators correspond to the identity operator (the real space part is ignored as the commutation is obvious).

Suppose that when acting with \tilde{T}_x and \tilde{T}_y on an state, a single anyon crosses cut A . The general case follows from this by employing the argument to each anyon that crosses cut A when applying \tilde{T}_y . Assuming that n anyons cross cut B when applying \tilde{T}_x , where the just mentioned anyon is not among those n anyons, the acquired phases can be determined to be $e^{i\theta(N_c+2N_l)}e^{i2\theta m}e^{-i\theta(N-1)n}$ when acting with $\tilde{T}_x\tilde{T}_y$ on the state. The wave function component is changed from m to $m - n \bmod M$ in this process. For the reversed order, $\tilde{T}_y\tilde{T}_x$, the respective phase is $e^{-i\theta(N-1)n}e^{i\theta(N_c+2(N_l+n))}e^{i2\theta(m-n)}$, where it was used that after applying \tilde{T}_x , there are $N_l + n$ anyons to the left of the anyon to cross cut A . Further, the change in the wave function component affects the phase acquired due to ρ_1 . It can be seen that the two phases agree with each other.

In the second scenario, n anyons cross cut B due to the application of \tilde{T}_x , among which the anyon to cross cut A can be found. When acting with $\tilde{T}_x\tilde{T}_y$ on the state, the phase gained is $e^{i\theta(n-1+2(N-n))}e^{i2\theta m}e^{-i\theta(N-1)n}$, where $N_c = n - 1$ and $N_l = N - n$ due to the n anyons being located in the right most column has been used. For the other case of applying $\tilde{T}_y\tilde{T}_x$, the acquired phase is $e^{-i\theta(N-1)n}e^{i\theta(n-1)}e^{i2\theta(m-n)}$, where the change in the wave function component, $N_c = n - 1$ and $N_l = 0$ was used for the state obtained after applying \tilde{T}_x . By reminding ourselves that (2.8) holds, it is clear that both phases agree. As a generalization to multiple anyons crossing cut A is obvious, it follows that $[\tilde{T}_x, \tilde{T}_y] = 0$. With this commutator, it is clear that $\tilde{T}_{x(y)}|\psi_{k_x, k_y}\rangle = e^{-ik_x(y)}|\psi_{k_x, k_y}\rangle$, as expected for a momentum state. This (or a similar) discussion was omitted in [18].

In order show that the momentum states $|\psi_{k_x, k_y}\rangle$ block diagonalize the Hamiltonian H , we take a look at the overlap $\langle\psi'_{k'_x, k'_y}|H|\psi_{k_x, k_y}\rangle$, similar to [18]. Assuming that there are two parameters l and p such that $\langle\psi'|H\tilde{T}_x^l\tilde{T}_y^p|\psi\rangle = \eta \neq 0$, it can be argued that $\langle\psi'|(\tilde{T}_y^\dagger)^j(\tilde{T}_x^\dagger)^i H \tilde{T}_x^{l+i}\tilde{T}_y^{p+j}|\psi\rangle = \eta$ for all i and j . The reason for this is that the hermitian conjugates of the translation operators, \tilde{T}_x^\dagger and \tilde{T}_y^\dagger , cancel all contributions from their counterparts and the additional contributions from the Hamiltonian that arise due to the previous translations. If e.g. applying \tilde{T}_x^i onto $\tilde{T}_x^l|\psi\rangle$ leads to anyons crossing cut B , all effects due to this process are canceled by its conjugated counterpart $(\tilde{T}_x^\dagger)^i$. The only exception occurs if one of the anyons that crossed the cut is also translated by the Hamiltonian in x -direction and if this anyon is located such that applying H onto $\tilde{T}_x^l|\psi\rangle$ also translates it across the cut. In this case however, the contribution that is not canceled by $(\tilde{T}_x^\dagger)^i$ corresponds to the contribution that arises due the application of H onto $\tilde{T}_x^l|\psi\rangle$, i.e., the two states $H\tilde{T}_x^l|\psi\rangle$ and $(\tilde{T}_x^\dagger)^i H \tilde{T}_x^{l+i}|\psi\rangle$ are identical. This applies no matter whether or not the Hamiltonian translates an anyon over the cut, as can be verified using the

string rules.

The same argument can be used for \tilde{T}_y : All the phases acquired due to anyons crossing cut A upon applying \tilde{T}_y^j onto $\tilde{T}_y^p|\psi\rangle$ are canceled by $(\tilde{T}_y^\dagger)^j$. The exception occurs if an anyon that crossed the cut is also translated by the Hamiltonian in y -direction and if this anyon is located such that the application of H onto $\tilde{T}_y^p|\psi\rangle$ already translates it over the cut. Only if this condition is met, $(\tilde{T}_y^\dagger)^j$ does not translate the anyon back across the cut. But as this corresponds exactly to what happens if the Hamiltonian is applied without the additional translations \tilde{T}_y^j , one can see that $H\tilde{T}_y^p|\psi\rangle$ and $(\tilde{T}_y^\dagger)^j H\tilde{T}_y^{p+j}|\psi\rangle$ are identical states.

It thus follows that $\langle\psi'_{k'_x, k'_y}|H|\psi_{k_x, k_y}\rangle \propto \eta \sum_{j=0}^{L_x-1} \sum_{n=0}^{L_y-1} e^{i(j(k_x-k'_x)+n(k_y-k'_y))} \propto \eta \delta_{k_x k'_x} \delta_{k_y k'_y}$ and therefore, the momentum states indeed block diagonalize the Hamiltonian.

In [18], the allowed momenta for the momentum states $|\psi_{k_x, k_y}\rangle$ were not discussed in great detail. We will elaborate on this topic a little bit further. Each state $|\psi\rangle$ possesses two periodicities p_x and p_y with $p_x \leq L_x$ and $p_y \leq L_y$, which are defined to be the smallest positive integers such that $T_x^{p_x}|\psi\rangle = |\psi\rangle$ and $T_y^{p_y}|\psi\rangle = |\psi\rangle$, respectively. For the former periodicity, it is important to impose the additional condition that upon acting with $T_x^{p_x}$ on $|\psi\rangle$, the total number of anyons crossing cut B is a whole multiple of M such that the initial and the final wave function component in the superposition (2.15) agree. In order to assure that $\tilde{T}_{x(y)}^{p_x(y)}|\psi_{k_x, k_y}\rangle = |\psi_{k_x, k_y}\rangle$, the momenta k_x and k_y have to compensate the acquired phases. I.e., $k_x = (2\pi n_x - \theta_x)/p_x$ and $k_y = (2\pi n_y - \theta_y)/p_y$ with $n_x \in \{0, 1, \dots, p_x - 1\}$, $n_y \in \{0, 1, \dots, p_y - 1\}$, $\theta_x = -\theta(N-1)N_x(p_x)$ and $\theta_y = \theta(N_c(p_y) + 2N_l(p_y)) + 2\theta(m-1)N_y(p_y)$ have to be chosen, where m is again the wave function component.

Unfortunately, the above algorithm has some limitations. The first, obvious thing to mention is that the algorithm is restricted to abelian anyon models and even for those, it only allows to simulate a single type of anyons. While this still allows for many interesting applications, a generalization to arbitrary anyon models and multiple anyon types is desirable as it allows for more complex simulations to be performed. In principle, one could try to resolve this issue of simulating multiple anyon types by associating different string types to each anyon type in such a way that the acquired phases depend on both the anyon type of the anyon that is moving and the anyon type associated to the relevant string. While this could in principle take care of all the mutual and exchange statistics among the anyons, it is not clear how this would affect the rules for moving across the cuts.

Further, the flux fixing of Φ_x and Φ_y in (2.9) seems to be arbitrary. While it is explained in [17] that this condition is the same as the one for anyons on an annulus [16], it is questionable whether this actually translates to the torus due to the annulus and the torus being topologically different. In addition to that, the phase $e^{-i\theta(N-1)}$ that is gained upon crossing cut B is completely arbitrary as it depends on the conventional arrangement of anyons in Fig. 2.1. Reflecting the y -coordinate of each anyon (i.e. $y \rightarrow -y$) in this convention would for example lead to this phase becoming $e^{i\theta(N-1)}$. This would then also influence the definition of Φ_x again.

While the latter part is purely conventional, it is of great importance to develop an algorithm that is not limited to abelian anyon models and/or single anyon types in order to broaden the range of possible applications. Ideally, such an algorithm is more intuitive both with respect to

the flux convention and the physical interpretation of the cuts' effects. A generalized algorithm that does all these things is presented in section 4.

2.2. Adding Interactions

Later on, in section 6.2, we will study systems of interacting particles whose interactions are described by a power law, i.e., the interaction has the form $\phi(r) = U/r^n$, where U and n determine the interaction strength and the decay. Since we imposed PBC for the algorithm discussed above, the shift in energy due to the interactions is given by

$$\Phi(x, y) = \sum_{m \in \mathbb{Z}, l \in \mathbb{Z}} \frac{U}{\sqrt{(x - mL_x)^2 + (y - lL_y)^2}^n}, \quad (2.16)$$

where we assumed that there are only two particles on the lattice. x and y are the differences in x - and y -coordinates of the two particles. The sum over m and l is necessary as due to the PBC, there are particles localized at positions $(x_i - mL_x, y_i - lL_y)^\top$ for $m \in \mathbb{Z}, l \in \mathbb{Z}$ and for all particles i , where x_i and y_i denote the coordinates of the i -th particle with $0 \leq x_i < L_x$ and $0 \leq y_i < L_y$. I.e., because of this periodicity, the two particles effectively interact with each other multiple times, where each time corresponds to a different choice of m and l . This is exactly what (2.16) captures.

For the rest of this section, we will restrict ourselves to this case of two particles. However, the generalization to more particles is straight forward: One simply has to compute $\Phi(x, y)$ for all two-particle combinations and sum them up.

In order to efficiently compute (2.16), we follow the discussion in [23]. The goal is to split $\Phi(x, y)$ into a local and a distant contribution $\Phi_{local}(x, y)$ and $\Phi_{distant}(x, y)$, i.e.

$$\Phi(x, y) = \Phi_{local}(x, y) + \Phi_{distant}(x, y). \quad (2.17)$$

$\Phi_{local}(x, y)$ is a sum similar to (2.16) over a short-range interaction $\phi_{short}(r)$ rather than $\phi(r)$. Here, $\phi_{short}(r)$ is supposed to decay rapidly in real space such that $\Phi_{local}(x, y)$ converges fast, i.e., only few terms in the sum have to be computed to numerically estimate $\Phi_{local}(x, y)$.

Similar to $\Phi_{local}(x, y)$, $\Phi_{distant}(x, y)$ sums over all contributions of a long-range interaction $\phi_{long}(r)$ that decays slowly in real space. By transforming $\phi_{long}(r)$ to Fourier space, we again obtain a rapidly decaying function such that $\Phi_{distant}(x, y)$ can be computed/estimated by summing over comparably few terms in Fourier space in the infinite sum. We remind that the reason for this is that sums like (2.16) can also be expressed as sums over the Fourier transform using the well-known Poisson summation formula [24] that is given by:

$$L \sum_{n \in \mathbb{Z}} f(x + nL) = \sum_{n \in \mathbb{Z}} \tilde{f}(n/L) e^{2\pi i n x / L}, \quad (2.18)$$

$$\text{with the Fourier transform } \tilde{f}(x) = \int_{-\infty}^{\infty} dy f(y) e^{-2\pi i x y}. \quad (2.19)$$

From the above introduction of $\phi_{short}(r)$ and $\phi_{long}(r)$, it is immediately clear that

$$\phi(r) = \phi_{short}(r) + \phi_{long}(r). \quad (2.20)$$

We chose to utilize the gamma function Γ and its two incomplete versions in order to define

$$\phi_{short}(x, y) = \frac{U}{\sqrt{x^2 + y^2}^n} \frac{1}{\Gamma\left(\frac{n}{2}\right)} \int_{x^2+y^2}^{\infty} du u^{\frac{n}{2}-1} e^{-u} \quad (2.21)$$

$$\phi_{long}(x, y) = \frac{U}{\sqrt{x^2 + y^2}^n} \frac{1}{\Gamma\left(\frac{n}{2}\right)} \int_0^{x^2+y^2} du u^{\frac{n}{2}-1} e^{-u} = \frac{2U}{\Gamma\left(\frac{n}{2}\right)} \int_0^1 dv v^{n-1} e^{-v^2(x^2+y^2)}, \quad (2.22)$$

where we replaced the dependencies on r by dependencies on x and y , corresponding to the 2D coordinates. For $n = 1$, this reproduces the forms proposed in [23]. It is clear that (2.21) decays very rapidly for large distances due to the incomplete gamma function. At the same time, it can be seen that the same is true for the Fourier transform $\tilde{\phi}_{long}(k_x, k_y)$ of (2.22), which is given by

$$\begin{aligned} \tilde{\phi}_{long}(k_x, k_y) &= \frac{2U}{\Gamma\left(\frac{n}{2}\right)} \int_0^1 du \int_{-\infty}^{\infty} dx \int_{-\infty}^{\infty} dy u^{n-1} e^{-u^2(x^2+y^2)} e^{-2\pi i k_x x} e^{-2\pi i k_y y} \\ &= \frac{\pi U}{\Gamma\left(\frac{n}{2}\right)} \left[\pi^2 (k_x^2 + k_y^2) \right]^{\frac{n}{2}-1} \int_{\pi^2(k_x^2+k_y^2)}^{\infty} dv v^{-\frac{n}{2}} e^{-v}. \end{aligned} \quad (2.23)$$

Note that the factor of 2π is not included in k_x and k_y like it is usually done for Fourier transforms in physics. This convention was chosen here since it is the usual mathematical convention as used in (2.19).

By using the latter equation and the result for $\tilde{\phi}_{long}(k_x, k_y)$, the two contributions to $\Phi(x, y)$ can be determined:

$$\Phi_{local}(x, y) = \sum_{m \in \mathbb{Z}, l \in \mathbb{Z}} \phi_{short}(x - mL_x, y - lL_y), \quad (2.24)$$

$$\Phi_{distant}(x, y) = \frac{1}{L_x L_y} \sum_{m \in \mathbb{Z}, l \in \mathbb{Z}} \tilde{\phi}_{long}(m/L_x, l/L_y) e^{2\pi i m x / L_x} e^{2\pi i l y / L_y}. \quad (2.25)$$

While this is the main result of this section that is to be used to compute the interactions between particles on a periodic lattice, one might ask whether the sum in (2.25) indeed converges faster than its real space counterpart. After all, there are additional factors of L_x and L_y involved in the arguments. Also, $\phi_{long}(x, y) \propto (x^2 + y^2)^{-n/2}$ compared to $\tilde{\phi}_{long}(k_x, k_y) \propto (k_x^2 + k_y^2)^{n/2-1}$ might play a role.

In order to show that (2.25) always converges faster for all the cases to be considered in this thesis, we plotted $\phi_{long}(x/L_x, 0)$ and $\tilde{\phi}_{long}(x/L_x, 0)$ as function of x in Fig. 2.3, where we chose the parameters to be $U = 1$, $L_x = 40$ and $n = 3$. The latter is the largest exponent to be considered in section 6.2 that also features the least favorable convergence behavior for $\tilde{\phi}_{long}$. $L_x = 40$ is the largest value of L_x that is studied in the context of interactions later on. From the plot, it can be seen that when its argument reaches approximately 1, $\tilde{\phi}_{long}(x/L_x, 0)$ decays

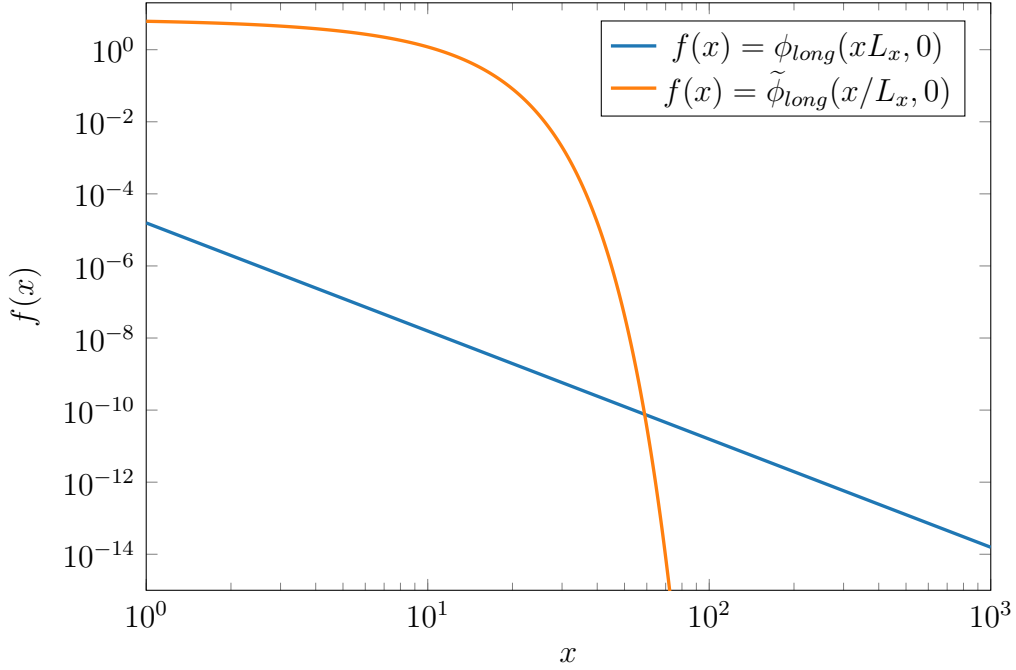


Figure 2.3.: $\phi_{long}(xL_x, 0)$ and $\tilde{\phi}_{long}(x/L_x, 0)$ as function of x with $U = 1$, $L_x = 40$ and $n = 3$.

very rapidly, i.e., for already slightly larger arguments, the contributions to the sum in (2.25) become smaller than the numerical precision. The same does not hold for $\phi_{long}(xL_x, 0)$, which gradually decays. We can thus infer that summing the Fourier transform in order to obtain the long-range interaction is indeed the superior method.

One might nevertheless argue that the summation in real space may suffice if the required precision is small enough. While this may be true for the above case, it is to be considered that for smaller exponents n , $\phi_{long}(xL_x, 0)$ converges more slowly, i.e., a real space summation may be appropriate only for large enough n . For smaller n , however, the summation in Fourier space becomes more efficient.

There is an additional remark to be made for the case $n = 1$, i.e., for Coulomb-like interactions. When trying to sum over ϕ_{long} , it is found that the result is always infinite, like for $\sum_n 1/n$. However, if we sum over the Fourier transform $\tilde{\phi}_{long}$, this divergence is contained in the single contribution for which both arguments are zero. Since only energy *differences* carry physical relevance, we can just exclude this point from the sum in (2.25) without changing the interaction/Hamiltonian. The key point why this works is that this contribution to $\Phi_{distant}(x, y)$ is identical for all x and y .

2.3. Continuous Simulations from Differential Equations

In order to complement the discrete lattice simulations discussed above, we will later on also study results from continuous simulations that are obtained by numerically integrating the corresponding Schrödinger equations. The most important consideration for this purpose is that

abelian anyons can be interpreted/modelled as (electrically) charged particles that have infinitely small flux tubes attached to them [25]. These flux tubes carry magnetic fluxes such that upon exchanging two anyons, the acquired phase due to the Aharonov-Bohm effect corresponds to the phase that is to be acquired according to the exchange statistics. One should however keep in mind that these charges and fluxes merely belong to a fictitious statistical gauge field.

We choose to work in bosonic gauge and with bosonic wave functions, i.e., non-bosonic statistics are obtained by using minimal coupling to an appropriate statistical gauge field in the Hamiltonian. For two identical anyons that carry charge q , this appropriate gauge field is given by $\mathbf{A} = \frac{\hbar c \alpha}{q} \nabla \theta$, where α denotes the statistical parameter that corresponds to the exchange statistics ($\alpha = 0$ for bosons and $\alpha = 1$ for fermions) and θ the angle between the two anyons [20, 26]. Due to reasons that become apparent later on, we will indeed restrict ourselves to this case of two anyons. If we now further assume a quadratic dispersion for the anyons, the Hamiltonian H can be separated into the following center of mass (H_{CM}) and relative parts (H_r) [20]:

$$H_{CM} = \frac{\mathbf{P}_{\mathbf{R}}^2}{4m}, \quad (2.26)$$

$$H_r = \frac{p_r^2}{m} + \frac{(p_\theta - \hbar \alpha)^2}{mr^2} + V(r). \quad (2.27)$$

Here, \mathbf{R} and r are the center of mass and relative coordinates of the two anyons; θ is again the angle between them. $\mathbf{P}_{\mathbf{R}}$, p_r and p_θ are the respective momentum operators, m the mass and $V(r)$ an additional interaction. The non-interacting case $V(r) = 0$ corresponds to the continuous version of the simulation discussed above in section 2.1 for two particles. For this case, the solutions to $H = H_{CM} + H_r$ are given by [20, 26]

$$\Psi(\mathbf{R}, r, \theta) \sim \sqrt{\frac{k}{L^3}} e^{i\mathbf{K} \cdot \mathbf{R}} e^{il\theta} J_{|l-\alpha|}(kr), \quad (2.28)$$

with the center of mass momentum \mathbf{K} , relative momentum k and $l = 2n, n \in \mathbb{Z}$ as we chose to work with bosonic wave functions. The corresponding total energy is $E = \hbar^2 \mathbf{K}^2 / 4m + \hbar^2 k^2 / m$. The normalization $\sqrt{k/L^3}$ is only correct in the limit of large L and for positive k . We chose to include it in (2.28) as this is the case of interest later on.

While this case is analytically soluble, we have to fall back on numerical integration when adding interactions. When doing this, one can simply choose a certain value for l and compute the relevant part $\psi(r, k)$ of $\Psi(\mathbf{R}, r, \theta)$, which is the part depending on r and k . For this, we remind that p_r^2 can be written as

$$p_r^2 = -\hbar^2 \left(\frac{d^2}{dr^2} + \frac{1}{r} \frac{d}{dr} \right). \quad (2.29)$$

I.e., the equation to be numerically integrated is given by

$$\left(-\frac{d^2}{dr^2} - \frac{1}{r} \frac{d}{dr} + \frac{(l - \alpha)^2}{r^2} + \frac{m}{\hbar^2} V(r) - k^2 \right) \psi(r, k) = 0, \quad (2.30)$$

which is only a differential equation in r since we chose a value for l such that the dependence on θ vanishes. For the eigenvalue, the same notation as in the non-interacting case was chosen. As for the numerical integration itself, two boundary conditions have to be chosen. The first, obvious choice is $\psi(0, k) = 0$ as two anyons are not allowed to be located on top of each other due to their statistics (given one does not choose $\alpha = 0$, i.e. bosons). For the second boundary condition, $\psi'(0, k) = a$ with an arbitrary $a \neq 0$ can be chosen. The reason for this is that after the normalization of ψ , the wave function does no longer depend on a . The normalization itself is done such that $\int_0^R dr r |\psi(r, k)|^2 = 1$, where R is the maximum simulation radius.

In the process of numerically integrating, one might need to take care for $r \rightarrow 0$ due to divergences in the differential equation. The solution is to simply substitute $r \rightarrow r + \epsilon$ with some small number $\epsilon > 0$ that has to be chosen such that the integration routine behaves well around $r = 0$.

3. Basic Formalism for Anyon Models

Here, we will introduce the most important basic aspects of anyon models that are essential in order to understand the construction of the generalized algorithm in section 4. We also briefly introduce the two anyon models to be studied later on, namely the semion and Fibonacci anyon model.

3.1. Basic Properties

For the purpose of reviewing the basic aspects of the description of anyon models that are essential for all the discussions to follow, the relevant parts of Refs. [27] and [28] are followed. Each anyon model contains a set \mathcal{C} of anyonic/topological charges, which are conserved quantum numbers obeying the commutative and associative fusion algebra

$$a \times b = \sum_c N_{ab}^c c, \quad (3.1)$$

where N_{ab}^c are the so-called fusion multiplicities, which are non-negative integers describing the number of distinct ways in which two anyonic charges a and b can fuse to charge c . There is a unique vacuum charge $1 \in \mathcal{C}$ which obeys the fusion rules $N_{a1}^c = \delta_{ac}$ and $N_{a\bar{a}}^1 = \delta_{a\bar{a}}$, where \bar{a} refers to the conjugate charge ("antiparticle") of charge a , which is also contained in \mathcal{C} : $\bar{\bar{a}} = a$, with $\bar{1} = 1$. This means that fusion (and also the later introduced braiding) with the vacuum charge is trivial.

Non-abelian anyon models possess the property that there is at least one pair of charges a and b for which $\sum_c N_{ab}^c > 1$, i.e., there are multiple fusion channels for these two charges. Abelian anyon models on the other hand possess the property that there is a unique fusion product for each pair of charges, i.e., $\sum_c N_{ab}^c = 1$ for all $a, b \in \mathcal{C}$.

It is highly beneficial to introduce a diagrammatic notation for anyons, in which the anyonic charges are represented by oriented lines with the corresponding charge labels attached to them. The following diagram is an example, in which charge c splits into charges a and b :



$$\begin{array}{c} a \quad b \\ \swarrow \searrow \\ c \end{array} . \quad (3.2)$$

This process is only allowed if $N_{ab}^c \neq 0$. In principle, one would need to introduce an additional label which can take the values $1, \dots, N_{ab}^c$ in order to distinguish the different ways in which the charges a and b can combine to form charge c . Such labels will be ignored here in order

to simplify the notation and provide diagrams of higher clarity, i.e., we restrict ourselves to $N_{ab}^c \in \{0, 1\}$. Putting these labels back for the general case is straight forward.

For such diagrams, reversing the orientation of a line is equivalent to replacing the charge by its conjugate charge. The interpretation of one anyon splitting into multiple other anyons in these diagrams is equivalent to the interpretation of multiple anyons fusing to a single anyon.

If charge d splits into three charges a , b and c , there are different basis choices that can be used. These basis choices are related via F -moves

$$\begin{array}{c} a \quad b \quad c \\ \diagdown \quad \diagup \quad \diagup \\ e \quad \diagdown \quad \diagup \\ \quad \quad \quad d \end{array} = \sum_f [F_d^{abc}]_{ef} \begin{array}{c} a \quad b \quad c \\ \diagdown \quad \diagup \quad \diagup \\ \quad \quad \quad f \quad \diagdown \quad \diagup \\ \quad \quad \quad \quad \quad d \end{array}, \quad (3.3)$$

which are unitary and therefore satisfy the relation

$$[F_d^{abc}]_{ef}^{-1} = [F_d^{abc}]_{ef}^\dagger = [F_d^{abc}]_{fe}^*. \quad (3.4)$$

If any of the charges a , b or c is the trivial charge 1, then the corresponding F -move is $F_d^{abc} = \mathbb{1}$, assuming the fusion is allowed by the fusion rules. When dealing with more than three anyons, the different bases can still be related to each other via strings of F -moves.

Counter-clockwise exchanges of two anyons a and b can be written in terms these anyons without any braiding using R -moves, that is,

$$\begin{array}{c} b \quad a \\ \diagdown \quad \diagup \\ \quad \quad \quad c \end{array} = R_c^{ab} \begin{array}{c} b \quad a \\ \diagdown \quad \diagup \\ \quad \quad \quad c \end{array}. \quad (3.5)$$

The R -moves are unitary and thus obey $(R_c^{ab})^{-1} = (R_c^{ab})^\dagger = (R_c^{ba})^*$. Furthermore, braiding with the vacuum charge is trivial, i.e. $R_c^{1b} = R_c^{a1} = 1$.

\mathcal{C} together with N_{ab}^c , $[F_d^{abc}]_{ef}$ and R_c^{ab} are the basic data that fully define an anyon model and thus, only these properties are needed in order to implement the algorithm to be discussed. It is however useful to first use the basic data to introduce a few additional quantities that will be needed for the algorithm later on.

For systems with more than two anyons, it is beneficial to introduce additional braid operators:

$$\begin{array}{c} a \quad b \quad c \\ \diagdown \quad \diagup \quad \diagup \\ e \quad \diagdown \quad \diagup \\ \quad \quad \quad d \end{array} = \sum_f [B_d^{abc}]_{ef} \begin{array}{c} a \quad b \quad c \\ \diagdown \quad \diagup \quad \diagup \\ \quad \quad \quad f \quad \diagdown \quad \diagup \\ \quad \quad \quad \quad \quad d \end{array} \quad (3.6)$$

and

$$\begin{array}{c} a \\ \nearrow \\ e \\ \nwarrow \\ d \end{array} \begin{array}{c} b \\ \nearrow \\ c \end{array} = \sum_f [B_d'^{abc}]_{ef} \begin{array}{c} a \\ \nearrow \\ f \\ \nwarrow \\ d \end{array} \begin{array}{c} b \\ \nearrow \\ c \end{array}, \quad (3.7)$$

where

$$[B_d^{abc}]_{ef} = \sum_g [F_d^{acb}]_{eg} R_g^{cb} [F_d^{abc}]_{gf}^{-1} \quad \text{and} \quad [B_d'^{abc}]_{ef} = \sum_g [F_d^{acb}]_{eg} (R_g^{cb})^* [F_d^{abc}]_{gf}^{-1}. \quad (3.8)$$

Using the unitarity of the F - and R -moves, it can be seen that these two operators are related by (note the reversed order of charges b and c)

$$[B_d^{abc}]_{ef}^{-1} = [B_d'^{acb}]_{ef}. \quad (3.9)$$

This means that one of those operators would be sufficient in order to describe what is to be discussed later. Nevertheless, both operators will be used as doing so provides more clarity. By comparison with the braid group operators discussed in section 2.1.1, it can be seen that the B - and B' -operators correspond to the σ - and σ^{-1} -operators of the braid group.

The quantum dimension d_a associated to charge a is given by

$$d_a = \begin{array}{c} \text{a circle with charge } a \text{ on the left} \end{array} = \left| [F_a^{a\bar{a}a}]_{11} \right|^{-1} \quad (3.10)$$

and equals the largest eigenvalue of the matrix N_a with entries $[N_a]_{bc} = N_{ab}^c$. With this, the total quantum dimension \mathcal{D} is given as

$$\mathcal{D} = \sqrt{\sum_a d_a^2}. \quad (3.11)$$

The topological spin θ_a of charge a is defined as

$$\theta_a = \frac{1}{d_a} \begin{array}{c} \text{a figure-eight with charge } a \text{ on the central strand} \end{array} = \sum_c \frac{d_c}{d_a} R_c^{aa} \quad (3.12)$$

and is a root of unity. Using the ribbon property [22], the topological spins can be related to the R -moves:

$$R_c^{ab} R_c^{ba} = \frac{\theta_c}{\theta_a \theta_b} \mathbb{1}. \quad (3.13)$$

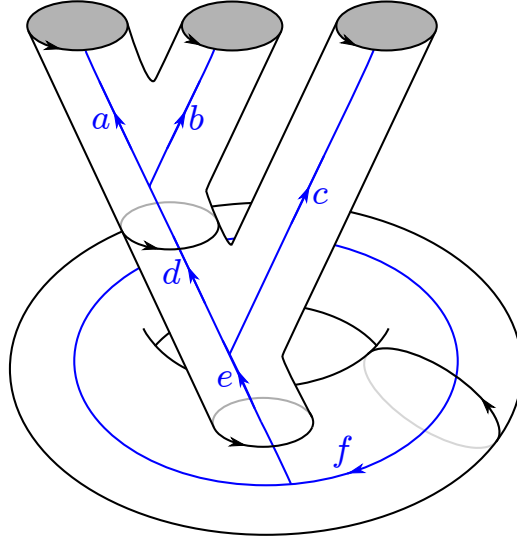


Figure 3.1.: Torus with the three charges associated to the punctures fusing to charge e which then fuses with the anyonic charge f moving along a non-contractible loop, which is hereby defined to follow the negative x -direction; the black loop being threaded by f hence follows the (positive) y -direction. The fusion order of the charges indicated here is used as the conventional fusion order for braiding.

3.2. Fusion Diagrams: Basis States

The final quantity to be introduced is the punctured torus S -matrix:

$$S_{ab}^{(z)} = \frac{1}{\mathcal{D}\sqrt{d_z}} a \left(\text{diagram of two loops} \right) z = \frac{1}{\mathcal{D}} \sum_c d_a d_b \frac{\theta_c}{\theta_a \theta_b} [F_a^{b\bar{b}a}]_{1c} [F_a^{b\bar{b}a}]_{c\bar{z}}^{-1} [F_{\bar{z}}^{z\bar{a}\bar{a}}]_{a1}, \quad (3.14)$$

with $N_{a\bar{a}}^z \neq 0$ and $N_{b\bar{b}}^z \neq 0$. In many other contexts, $S_{ab}^{(1)}$ is simply referred to as "the S -matrix". $S_{ab}^{(z)}$ can be used for a basis change on a torus from a basis in which anyons move along one non-contractible loop to a basis in which anyons move along another, complementary non-contractible loop. An example for this is given by Fig. 3.1: The charges associated to the three punctures fuse to charge e , where the charges are measured with respect to the black, oriented loops that are threaded by them. When changing the basis with $S^{(e)}$, anyon f is replaced with another anyon moving along a complementary non-contractible loop, similar to the black one measuring the anyonic charge f in the initial state. This very black loop is then also transformed to a non-contractible loop complementary to its initial one after the basis transformation, similar to the initial loop of charge f . For this to be the correct transformation, all the charges associated to the punctures on the torus need to fuse to charge z . These two different basis choices are also referred to as "inside basis" and "outside basis" [29].

Fig. 3.1 also indicates the convention for the fusion order: First, the two "left" anyons a and b fuse, then their fusion product fuses with the anyon associated to the third puncture. This

fusion product then fuses with the anyon threading the torus.

For this to be consistent, $N_{ef}^f > 0$ has to be fulfilled. This constraint already implies that for abelian anyon models, the final fusion product of all the charges associated to punctures has to be the vacuum charge since $N_{1f}^f = 1$ is (as mentioned above) a basic property of the fusion algebra and $\sum_a N_{1a}^a = 1$, i.e., $N_{ba}^a = 0$ if $b \neq 1$ for abelian anyons.

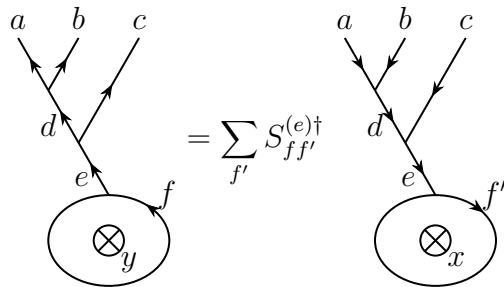
This seems to be the generalization of the condition $e^{i2\theta N} = 1$ that has to be fulfilled when simulating abelian anyons according to the already known implementations (see (2.8) or [17, 18, 21]). With these implementations, the dynamics of only one anyon type can be simulated. When exchanging two of these anyons, a phase of θ is obtained; N refers to the total anyon number. In order to see that the condition $e^{i2\theta N} = 1$ is equivalent to the condition that the N anyons fuse to the vacuum charge, one can consider the following: If an anyon is dragged around N other anyons along a closed loop, the obtained phase is $(e^{i2\theta})^N = 1$ since the anyon being dragged is effectively exchanged twice with all anyons inside the closed loop. Since this is a trivial phase corresponding to the anyon being dragged around a vacuum charge, the N anyons are indeed equivalent to a trivial charge.

It is useful to introduce the following diagrammatic notation for the state in Fig. 3.1:



The diagram shows three incoming lines labeled a , b , and c from the top. They merge into a line labeled d . This line d then merges into a line labeled e . This line e enters a circle containing a cross symbol \otimes and the index y . A line labeled f exits the circle from the right. The entire diagram is labeled (3.15) on the right.

where \otimes represents a non-contractible loop and the attached index y is used to represent the loop's direction. Thus, anyon f moves along a loop in x -direction, complementary to the one in y -direction. The index is of importance, as both directions are to be considered in the later sections. In this notation, the basis change using the punctured torus S -matrix reads



The equation shows a diagrammatic transformation. On the left is the diagram from (3.15) with lines a, b, c, d, e and a loop \otimes_y with anyon f . This is followed by an equals sign and a summation over f' of $S_{ff'}^{(e)\dagger}$. On the right is a similar diagram but with a loop \otimes_x and anyon f' . The entire equation is labeled (3.16) on the right.

where \otimes_x represents a non-contractible loop complementary to the loop in y -direction along which f' moves. The sum runs over all such anyon charges f' . Note that in this convention, the orientation of the line corresponding to the anyon moving along the non-contractible loop is reversed upon changing the basis.

Another important aspect is that also the orientation of all the lines associated to the other anyons are reversed upon transforming with the punctured torus S -matrix. The reason for this can be seen in diagram (3.14): The punctured torus S -matrix transforms the basis in which anyons move around a non-contractible loop to a basis in which anyons move around another non-contractible loop complementary to the initial one. As charge z moves from one loop to the other, its orientation is different with respect to the two loops, which is reflected in the diagrams before and after the basis change. This is depicted in (3.16), where f corresponds to a in (3.14), f' to b and e to z . The fact that e itself is a fusion product of other anyons does only matter in the sense that these anyons then also appear after the transformation with the reversed orientation.

It is to be noted that the transformation in (3.16) is done using $S^{(e)\dagger}$ rather than $S^{(e)}$. This is a detail arising from the way the crossings of the non-contractible loops in the new and in the old basis are oriented with respect to each other [30].

Generalizing the state given by (3.15) to N anyons leads to

(3.17)

where α_i are the anyonic charges associated to the punctures of the torus, f_i their fusion products according to the defined fusion order and a the anyon moving along the non-contractible loop. This forms the basis state in terms of fusion diagrams for all braid operations to be performed in the algorithm discussed in the next chapter. Apart from the fusion consistency conditions in all other vertices that also have to be satisfied, the generalized consistency condition involving the final fusion product of all the anyons and the anyon moving along the non-contractible loop reads

$$N_{f_{N-1}a}^a > 0. \quad (3.18)$$

It is noted again that for abelian anyon models, (3.18) can only be fulfilled if $f_{N-1} = 1$ due to the properties of the fusion algebra, i.e., abelian anyons must fuse to the vacuum charge in order to be able to exist on a torus.

3.3. The Semion and Fibonacci Anyon Model

Two different anyon models will be considered: The first one is the semion model [22], for which the known algorithms [17, 18] are also applicable. It consists only of the vacuum charge 1 and the semionic charge s with $\bar{s} = s$ and is an abelian anyon model with the only non-trivial fusion rule being

$$s \times s = 1. \quad (3.19)$$

All the F -moves except for one are either 1 or 0 depending on whether or not the charges are fusion consistent. The exception is

$$[F_s^{sss}]_{11} = -1. \quad (3.20)$$

Similar to the F -moves, there is only one non-trivial R -move:

$$R_1^{ss} = i. \quad (3.21)$$

With that, the semion model's basic data is already complete.

The second model to be considered is the Fibonacci anyon model [7]. Similar to the semion model, the Fibonacci model consists of only two anyons: $\mathcal{C} = \{1, \tau\}$, with the Fibonacci anyon τ and $\bar{\tau} = \tau$. It is a non-abelian model with the non-trivial fusion rule

$$\tau \times \tau = 1 + \tau. \quad (3.22)$$

The non-trivial F - and R -moves are given by

$$F_\tau^{\tau\tau\tau} = \begin{pmatrix} \varphi^{-1} & \varphi^{-1/2} \\ \varphi^{-1/2} & -\varphi^{-1} \end{pmatrix}, \quad R_1^{\tau\tau} = e^{4\pi i/5} \quad \text{and} \quad R_\tau^{\tau\tau} = e^{-3\pi i/5}, \quad (3.23)$$

with the golden ratio $\varphi = (1 + \sqrt{5})/2$.

4. Lattice Simulations for Non-abelian Anyons

In the following sections, the newly developed algorithm that is able to simulate arbitrary abelian and non-abelian anyon models on lattices is presented. We start in section 4.1 by discussing some considerations that are of importance. Then, in section 4.2, the new algorithm itself is explained. For this algorithm, it is also possible to construct momentum states. However, as the construction is quite technical, it is discussed in appendix A.

Lastly, in appendix B, it is shown that when taking the appropriate abelian anyon model as input, our algorithm reproduces the algorithm for abelian anyons discussed above in section 2.1, proving that it is indeed a generalization to both abelian and non-abelian anyon models.

4.1. Preparatory Considerations

The aim of this section is to make some important preparatory considerations regarding the Hamiltonian to be simulated and its Hilbert space. The final goal is to simulate anyons of a given anyon model hopping on a 2D square lattice according to the tight-binding Hamiltonian

$$\mathcal{H} = - \sum_{\alpha, \langle ij \rangle} T_{ij}(\{\mathbf{r}_k\}, \{\alpha_k\}) c_{\alpha, j}^\dagger c_{\alpha, i} + \text{H.c.} \quad (4.1)$$

with PBC in both directions, where the sum runs over all nearest-neighbor sites i and j and the anyonic charges α . $c_{\alpha, i}^\dagger$ ($c_{\alpha, i}$) creates (annihilates) an anyon of charge α at site i ; the associated commutation relations will be discussed in the next section. $T_{ij}(\{\mathbf{r}_k\}, \{\alpha_k\})$ are matrices whose entries depend on the positions $\{\mathbf{r}_k\}$ of all anyons and their charges $\{\alpha_k\}$, where the i -th anyon is located at the i -th position in $\{\mathbf{r}_k\}$ and is of the charge corresponding to the i -th element in $\{\alpha_k\}$. The dimensions of the matrices $T_{ij}(\{\mathbf{r}_k\}, \{\alpha_k\})$ correspond to the number of components of the anyon wave functions. Note that the $\{\mathbf{r}_k\}$ - and $\{\alpha_k\}$ -dependencies do only exist with respect to the anyon configurations and not their order, i.e., a given matrix remains unchanged if $\{\mathbf{r}_k\}$ and $\{\alpha_k\}$ are replaced by the *same* permutation of the respective set as the corresponding anyon configuration is the same. This also applies to all other quantities to be discussed that have this dependency. The construction of the matrices is discussed in detail in the next section. Similar to Refs. [17] and [18], two cuts, one in x - and one in y -direction named cuts A and B , can be introduced onto the lattice. Cut A , which is parallel to the x -axis, is chosen to have a y -coordinate equal to $y = 1/2$, such that translating an anyon with a y -coordinate of $y = L_y$ in positive y -direction translates it over the cut, where $y = L_y$ corresponds to $y = 0$ due to the PBC. Similarly, cut B (which is parallel to the y -axis) is chosen to have a x -coordinate

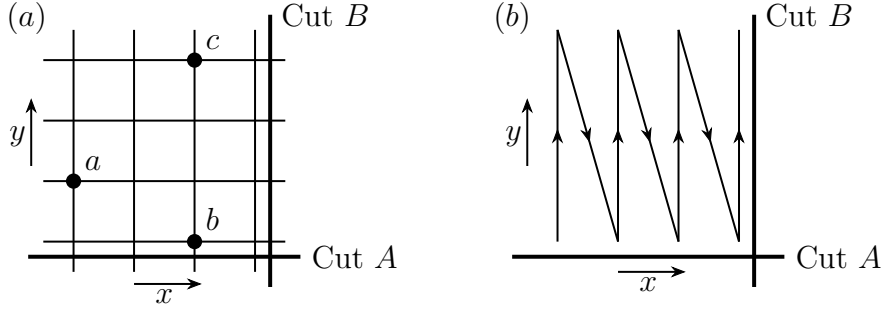


Figure 4.1.: (a): Choice of cuts A and B on a lattice containing three anyons corresponding to diagram (3.15) if the sheet is chosen accordingly. (b): Choice of fusion order. Anyons with small x -coordinates fuse first; among those with the same x -coordinate, anyons with smaller y -coordinates come first.

of $x = L_x + 1/2$ (or, equivalently, $x = 1/2$), with $x = L_x$ corresponding to $x = 0$ such that translating an anyon with a x -coordinate of $x = L_x$ in positive x -direction translates it over this cut. The two cuts are special in the sense that if an anyon is translated over one of them, $T_{ij}(\{\mathbf{r}_k\}, \{\alpha_k\})$ will be constructed according to a different rule than if this is not the case. The cuts can be seen in Fig. 4.1 (a), where also three anyons were added onto the lattice such that this scenario corresponds to diagram (3.15), where the fusion order depicted in Fig. 4.1 (b) has been chosen as convention. According to this fusion order, the first anyons to fuse in the corresponding diagrams are the ones with the smallest x -coordinates. Among those with the same x -coordinates, the anyons with smaller y -coordinates fuse before those with bigger y -coordinates. This fusion order is conceptually very similar to the order introduced by a Jordan-Wigner string when mapping spin- $\frac{1}{2}$ operators to fermionic ones using the Jordan-Wigner transformation [31].

The lattice and anyons in Fig. 4.1 (a) themselves do not contain any information about the fusion products and the anyon moving along the non-contractible loop. Such information is contained in the "sheets", which correspond to the components of the wave functions that were labeled by m in section 2.1. Each sheet thus represents an ordered string of fusion products together with an anyon moving along the non-contractible loop. Using the sheets, a basis of the Hilbert space is given by the states

$$|\{\mathbf{r}_k\}, \{\alpha_k\}; \mathcal{A}\rangle, \quad (4.2)$$

where $\{\mathbf{r}_k\}$ denotes the positions of the anyons and $\{\alpha_k\}$ their charge. \mathcal{A} are pairwise orthogonal, normalized vectors whose dimensions equal the total number of sheets. Here, we changed the notation compared to section 2.1 since \mathcal{A} are vectors, whereas m denoted integers. When discussing the construction of the momentum states later on in appendix A, it will become clear why we need vectors for the generalized algorithm instead of plain integers.

The entries of \mathcal{A} correspond to the probability amplitude of the anyon configuration $|\{\mathbf{r}_k\}, \{\alpha_k\}\rangle$ being on the respective sheet, i.e., having the respective fusion products and anyon moving along the non-contractible loop. The overlap between two states $|\{\mathbf{r}_k\}, \{\alpha_k\}; \mathcal{A}\rangle$ and $|\{\mathbf{r}'_k\}, \{\alpha'_k\}; \mathcal{A}'\rangle$

is given by

$$\langle \{\mathbf{r}'_k\}, \{\alpha'_k\}; \mathcal{A}' | \{\mathbf{r}_k\}, \{\alpha_k\}; \mathcal{A} \rangle \equiv \langle \{\mathbf{r}'_k\}, \{\alpha'_k\} | \{\mathbf{r}_k\}, \{\alpha_k\} \rangle \times \langle \mathcal{A}' | \mathcal{A} \rangle, \quad (4.3)$$

with the standard scalar product between vectors $\langle \cdot | \cdot \rangle$. $\langle \{\mathbf{r}'_k\}, \{\alpha'_k\} | \{\mathbf{r}_k\}, \{\alpha_k\} \rangle = 1$ if the anyons in both states are at the same positions and have the same charges, i.e., if the anyon configurations are identical. The vectors \mathcal{A} will be referred to as "sheet amplitude vectors".

It should be noted that the fusion order of the anyons in the states (4.2) may play an important role if different anyonic charges are involved: A changed fusion order might also change the possible (intermediate) fusion products of the state, which thus also changes the sheets on which the state may be. Similarly, it can also be seen that a given anyon configuration might not exist on every sheet if there are different anyonic charges involved, i.e., not all states of the form (4.2) are necessarily allowed to exist on every sheet. Thus, all possible sheet amplitude vectors \mathcal{A} of a given configuration might not span \mathbb{C}^{n_s} , but a subspace, where n_s refers to the total number of sheets that can be occupied by any anyon configuration.

On the other hand, if there is only one anyonic charge to be simulated, every anyon configuration is allowed on every sheet, i.e., all possible sheet amplitude vectors of a given anyon configuration span \mathbb{C}^{n_s} .

Let's take a look at the number of sheets for the two anyon models considered in this thesis: For semions, there are either two or zero sheets. If there is an even number of semions in the system, then these anyons will always fuse to the vacuum charge. Then, the consistency condition (3.18) is fulfilled for both $a = 1$ and $a = s$ and thus, there are two different sheets. If however the number of semions is odd, this consistency condition can never be fulfilled, i.e., such a system can not exist on a torus, corresponding to a total sheet number equal to zero. This argument thus agrees with the already discussed constraint $e^{i2\theta N} = 1$ for abelian anyons.

For Fibonacci anyons, the consistency condition (3.18) is fulfilled for an arbitrary (positive) number of τ -anyons if $a = \tau$ is chosen. The reason for this is the non-abelian fusion rule (3.22), which makes sure that both cases $f_{N-1} = 1$ and $f_{N-1} = \tau$ are consistent with $a = \tau$. Thus, any number of Fibonacci anyons may exist on a torus, which is a sharp contrast to the semion case or more generally the abelian case, for which $f_{N-1} = 1$ has to be fulfilled.

The total number of sheets n_s for $N > 0$ Fibonacci anyons is

$$n_s(N) = 2F_{N-1} + F_N, \quad (4.4)$$

with $F_{N+1} = F_N + F_{N-1}$, $F_0 = 0$ and $F_1 = 1$. This formula is based on the fact that if the N τ -anyons fuse to 1, both $a = 1$ and $a = \tau$ are consistent with (3.18), whereas if they fuse to τ , only $a = \tau$ is allowed. Using that the number of different ways of N τ s fusing to τ is given by F_N [7], one arrives at the above relation as due to the fusion rules, the only way for N τ s to fuse to 1 is for the first $N - 1$ τ s to fuse to τ . These relations can be inferred by taking a look at Fig. 4.2, which shows all allowed fusion diagrams for one (see (a)) and two (see (b)-(d)) Fibonacci anyons.

In general, the total number of sheets can be obtained by iterating over all combinations of

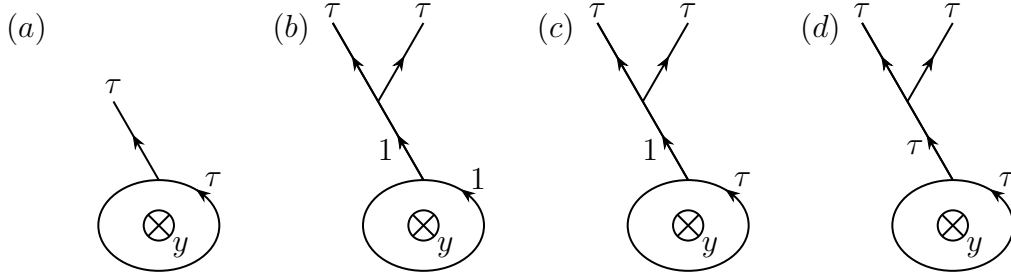


Figure 4.2.: Depiction of all allowed fusion diagrams for (a) one Fibonacci anyon and (b)-(d) two Fibonacci anyons.

fusion products $\{f_i\}$ and a in (3.17) and checking for fusion consistency in every vertex. The product of all the fusion multiplicities associated to the vertices corresponds to the number of sheets with the given configuration. Summing these products for all possible configurations of $\{f_i\}$ and a yields the total sheet number. Here, it is important to also consider fusion processes with different anyon orderings $\{\alpha_k\}$ if distinct anyonic charges are involved as this way, different (intermediate) fusion products may be allowed. There may also be multiple sheets with the same string of fusion products $\{f_i\}$ and the same a due to higher fusion multiplicities. These sheets are distinguished by additional labels associated to the vertices, which are suppressed here.

4.2. The Algorithm

In order to explain the construction of the tight-binding Hamiltonian (4.1) for an arbitrary anyon model, the states given by (4.2) will be used as basis. The choice of the sheet amplitude vectors does not matter as long as they are normalized, pairwise orthogonal and non-zero only where a given anyon configuration can exist on the corresponding sheet. The matrices $T_{ij}(\{\mathbf{r}_k\}, \{\alpha_k\})$ in (4.1) only act in the sheet space, i.e., on the sheet amplitude vectors \mathcal{A} of the basis states. Their dimensions thus agree with the total sheet number of the system. Even if there are "unphysical" sectors in the sheet space corresponding to sheets that are not allowed to be occupied by a given anyon configuration due to the fusion rules, $T_{ij}(\{\mathbf{r}_k\}, \{\alpha_k\})$ still acts on the full sheet space. The entries corresponding to the unphysical sectors are simply zero. From now on, we restrict ourselves to this physical subspace without explicitly mentioning it every time.

The entries of the Hamiltonian with respect to the basis states are given by

$$\begin{aligned}
 & \langle \{\mathbf{r}'_k\}, \{\alpha'_k\}; \mathcal{A}' | \mathcal{H} | \{\mathbf{r}_k\}, \{\alpha_k\}; \mathcal{A} \rangle \\
 &= - \sum_{\alpha, \langle ij \rangle} \langle \{\mathbf{r}'_k\}, \{\alpha'_k\} | c_{\alpha, j}^\dagger c_{\alpha, i} | \{\mathbf{r}_k\}, \{\alpha_k\} \rangle \times \langle \mathcal{A}' | T_{ij}(\{\mathbf{r}_k\}, \{\alpha_k\}) | \mathcal{A} \rangle \\
 & \quad + \langle \{\mathbf{r}'_k\}, \{\alpha'_k\} | c_{\alpha, i}^\dagger c_{\alpha, j} | \{\mathbf{r}_k\}, \{\alpha_k\} \rangle \times \langle \mathcal{A}' | T_{ij}^\dagger(\{\mathbf{r}_k\}, \{\alpha_k\}) | \mathcal{A} \rangle.
 \end{aligned} \tag{4.5}$$

It is sufficient to consider the translation of anyons only in positive x - and y -direction since the translations along the respective negative directions can be obtained by hermitian conjugation.

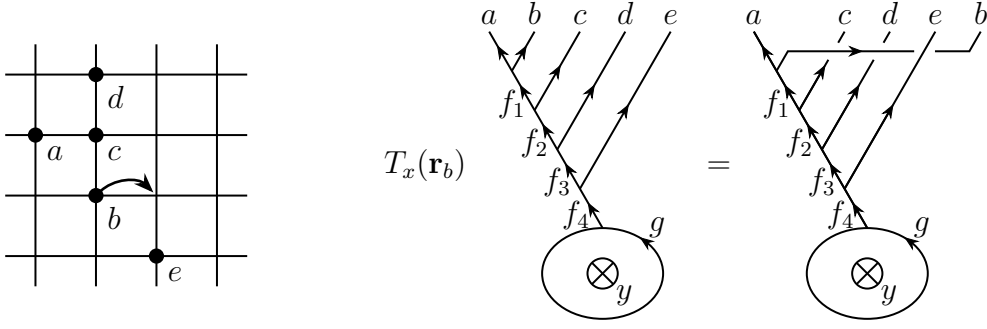


Figure 4.3.: Illustration of the braid rules for translating anyons in positive x -direction without crossing cut B . The lattice on the left shows an anyon configuration and indicates which anyon is to be translated. On the right, the effect of the translation on the fusion diagram is depicted.

The positive directions are chosen to be represented by the first term in the sum in (4.5). The second term is then obtained via conjugation of the first term for exchanged basis states. The effect of the translations encoded in the matrices $T_{ij}(\{\mathbf{r}_k\}, \{\alpha_k\})$ can be explained using the diagrammatic representation of the basis states (3.17). In general, when translating an anyon from one lattice site to another, the fusion order of the translated state (which is the same fusion order as the one of the initial state) might not be the same as the fusion order according to the convention in Fig. 4.1 (b). However, as this convention defines the fusion order for the basis states, the translated state has to be brought back to the conventional form using braid operators such that the entries in the Hamiltonian \mathcal{H} can be obtained with respect to this basis.

4.2.1. Translations in the Bulk

We start with the easiest case: When translating an anyon in positive y -direction without crossing cut A , the order of the anyons in the basis states corresponding to the initial and final state is the same. Thus, there are no braids due to such translations involved in these diagrams and the corresponding matrices $T_{ij}(\{\mathbf{r}_k\}, \{\alpha_k\})$ are identity matrices, $T_{ij}(\{\mathbf{r}_k\}, \{\alpha_k\}) = \mathbb{1}$.

A scenario in which braiding is involved can occur when translating an anyon in positive x -direction without it crossing cut B : If there is an anyon on the lattice with the same x -coordinate as the initial x -coordinate of the anyon being translated and with a greater y -coordinate than the latter anyon, the fusion order for these two anyons is different for the basis states corresponding to the state before and after the translation (see Fig. 4.1 (b)). An example for such an anyon configuration is given by the left-hand side of Fig. 4.3, where anyons b , c and d fulfil the above condition and anyon b is to be translated. The two cuts are not explicitly depicted due to the lack of relevance for this case. The anyons' fusion products in the diagrams on the right are labeled as f_1 to f_4 , the anyon moving along the non-contractible loop as g . The above translation process can be interpreted as braid in the fusion diagrams (3.17) in which the anyon to be translated moves to a spot such that the initial order of the anyons $\{\alpha_k\}$ before undergoing any fusion processes in the diagram corresponds to the conventional order of the basis

states. The fusion order itself remains unaffected, i.e., is the same as before the translation. In the given scenario, this can only happen if the line associated to the translated anyon moves across the line of the other anyon described above, i.e., they are braided. A convention in which the described process corresponds to the line of translated anyon moving "in front of" the other anyon will be used here. For the above example, this braid is depicted on the right-hand side of Fig. 4.3, where $T_x(\mathbf{r})$ denotes the operator translating the anyon located at position \mathbf{r} in positive x -direction and \mathbf{r}_b the position of anyon b .

A very similar situation occurs if an anyon is translated in positive x -direction and there is another anyon with a x -coordinate equal to the x -coordinate of the former anyon after the translation and a y -coordinate smaller than the one of the anyon to be translated. An example for this is again given by the anyon configuration on the left-hand side of Fig. 4.3, where anyons b and e meet the just mentioned condition.

Again, the fusion order of the basis states corresponding to the anyon configurations before and after the translation differ and therefore, this translation corresponds to a braiding process in the fusion diagrams. In contrast to the other scenario, the braiding is different: The line associated to the anyon being translated moves "behind" the line of the other anyon, as depicted by the diagram on the right-hand side of Fig. 4.3 for the anyons b and e .

The reason for this can be seen when looking at two anyons with the same x -coordinates. If the anyon with the smaller y -coordinate is translated and then the other anyon is also translated, there should not be overall braiding involved, as this scenario should be equivalent to translating the whole system of the two anyon in one step, which means that no braiding occurs. According to the rules above, the line associated to the first anyon with the smaller y -coordinate in the fusion diagram moves in front of the line of the other anyon. Then, the latter line moves behind the former one. Overall, the order of the anyons is back to its initial order and the lines are actually not braided, as they are always in front of/behind the other line, i.e., the rules are consistent with what is expected. Also, if one translates the two anyons in the reverse order, the order of the anyons in the intermediate state is not changed and thus, there is also no braiding involved, which is also consistent.

In principle, one can now apply the braid operators defined in (3.6) and (3.7) to express this diagram as superposition of diagrams of the form of the basis states. In this example, the final superposition of diagrams including these operators is given by

$$\sum_{f'_1, f'_2, f'_3} [B_{f_2}^{acb}]_{f_1 f'_1} [B_{f_3}^{f'_1 db}]_{f_2 f'_2} [B_{f_4}^{f'_2 f'_3 eb}]_{f_3 f'_3} \cdot \text{Diagram} \quad (4.6)$$

Using the rules and example in Fig. 4.3, the generalization of the operator string needed to bring an arbitrary fusion diagram after translation of an anyon back to its conventional form is straight forward: For each anyon fulfilling the first rule, a B -operator is to be applied. Each application changes one intermediate fusion product, over which is summed, yielding a superposition of diagrams. This also holds for all B' -operators which are to be applied for each anyon fulfilling the second rule. Subsequent operators depend on the latest intermediate fusion product introduced together with these operators. The order in which the operators have to be applied coincides with the order of the anyons fulfilling the rules according the fusion order convention, as this is used to order the anyons in the diagrams, i.e., the B -operators will always be applied before the B' -operators.

The string of B - and B' -operators corresponds to the entries in the matrices $T_{ij}(\{\mathbf{r}_k\}, \{\alpha_k\})$ if an anyon is translated in positive x -direction without crossing cut B . It can be seen from the amplitude contribution in (4.5) that the entry in the m -th row and n -th column corresponds to the single contribution in the sum over the different intermediate fusion products for which the sheet of the final state is the m -th sheet, given the sheet of the initial state is the n -th sheet. The enumeration of the sheets is of course arbitrary.

If one deals with an anyon configuration that can not exist on every sheet, the entries in the columns in $T_{ij}(\{\mathbf{r}_k\}, \{\alpha_k\})$ corresponding to the inaccessible sheets are zero.

Note that the special case in which an anyon is translated onto a site that is already occupied by another anyon is not considered here. Additional considerations which are discussed later on are needed in order to treat this case. For this reason, similar scenarios for the other translation types will also be ignored for now.

4.2.2. Translations over the Cuts

The final two cases to be considered occur when translating an anyon over one of the two cuts, which corresponds to dragging it once around the torus in the respective direction. This also explains the positions of the cuts: When translating an anyon with a $x(y)$ -coordinate of $L_x(L_y)$ in positive $x(y)$ -direction, its final $x(y)$ -coordinate is 1 due to PBC, i.e., it was dragged around the torus, which is indicated by crossing one of the two cuts.

To illustrate how this translation over a cut is dealt with diagrammatically, we consider an example of two anyons a and b fusing to anyon f ; the anyon moving along the non-contractible loop has charge c . Anyon b is translated in positive x -direction over cut B , which is indicated by the operator $T_{x,B}(\mathbf{r}_b)$ acting on the initial state. For now, any additional braid processes involving the anyons are ignored. In the diagram, the translation over cut B corresponds to dragging the respective anyon around the non-contractible loop. By using F -moves, the diagram

can then be expressed in terms of the basis states again:

$$\begin{aligned}
 T_{x,B}(\mathbf{r}_b) &= \text{Diagram 1} = \text{Diagram 2} = \sum_{c'} [F_{\bar{c}}^{abc}]_{f\bar{c}} \text{Diagram 3} \\
 &= \sum_{c'} [F_{\bar{c}}^{abc}]_{f\bar{c}} \text{Diagram 4} = \sum_{c',f'} [F_{\bar{c}}^{abc}]_{f\bar{c}} [F_{\bar{c}'}^{bac'}]_{\bar{c}f'} \text{Diagram 5}
 \end{aligned} \tag{4.7}$$

When dealing with a state that corresponds to a single diagram (i.e. a state with only one non-zero entry in the sheet amplitude vector) rather than a superposition of diagrams as initial state, the state after translating the anyon still features only one diagram for abelian anyons. For non-abelian anyons on the other hand, dragging an anyon of such a state around the torus in general yields a superposition of basis states/diagrams.

The above calculation can of course be generalized to an arbitrary state (3.17), where the last anyon in the fusion order is translated over cut B . The result can then be written in terms of a sum over all possible combinations of fusion products $\{f'_k\}$ and anyons moving along the non-contractible loop a' , i.e. all sheets, where each contribution is multiplied by the quantity $T_x^s(\{\alpha_k\}; \{f'_k\}, a'; \{f_k\}, a)$:

$$\begin{aligned}
 &\text{Diagram 1} = \sum_{\{f'_k\}, a'} T_x^s(\{\alpha_k\}; \{f'_k\}, a'; \{f_k\}, a) \text{Diagram 2}
 \end{aligned} \tag{4.8}$$

$T_x^s(\{\alpha_k\}; \{f'_k\}, a'; \{f_k\}, a)$ depends on the anyons $\{\alpha_k\}$ and their order, the sheet of the initial state and the sheet of the respective contribution to the final state. It is given by

$$T_x^s(\{\alpha_k\}; \{f'_k\}, a'; \{f_k\}, a) = \sum_{a', f'_1, \dots, f'_{N-1}} \left[F_{\bar{a}}^{f_{N-2} \alpha_N \bar{a}} \right]_{f_{N-1} \bar{a}'} \left[F_{\bar{a}'}^{\alpha_N f_{N-2} \bar{a}'} \right]_{\bar{a} f'_{N-1}}^{-1} \times \prod_{j=0}^{N-4} \left[F_{f'_{N-1-j}}^{\alpha_N f_{N-3-j} \alpha_{N-1-j}} \right]_{f_{N-2-j} f'_{N-2-j}}^{-1} \left[F_{f'_1}^{\alpha_N \alpha_1 \alpha_2} \right]_{f_1 f'_1}^{-1} \quad \text{for } N > 2 \quad (4.9)$$

and

$$T_x^s(\alpha_1, \alpha_2; f', a'; f, a) = \left[F_{\bar{a}}^{\alpha_1 \alpha_2 \bar{a}} \right]_{f \bar{a}'} \left[F_{\bar{a}'}^{\alpha_2 \alpha_1 \bar{a}'} \right]_{\bar{a} f'}^{-1} \quad \text{for } N = 2 \quad (4.10)$$

and is trivial for $N = 1$. It can be interpreted as entries of a "sheet hopping matrix" $T_x^s(\{\alpha_k\})_{s_f s_i} = T_x^s(\{\alpha_k\}; \{f'_k\}, a'; \{f_k\}, a)$ that is multiplied onto the sheet amplitude vector of the initial state upon translating the N -th anyon over cut B , where the index s_i stands for the initial and s_f for the final sheets.

Multiplying N sheet hopping matrices in the correct order and with the correct order of the anyon charges in their arguments yields the identity matrix:

$$T_x^s(\sigma^{N-1}(\{\alpha_k\})) T_x^s(\sigma^{N-2}(\{\alpha_k\})) \dots T_x^s(\{\alpha_k\}) = \mathbb{1}, \quad (4.11)$$

where $\sigma(1, 2, \dots, N) = (N, 1, 2, \dots, N-1)$. This relation holds due to the fact that if one successively drags all N anyons around the non-contractible loop in (4.8) such that the initial order is recovered and does not rewrite the diagram using the sheet hopping matrices, the anyons are not braided and the diagram is actually equivalent to the diagram of the initial state (3.17). Thus, by using the definition of the sheet hopping matrices, the correct order of a product of these matrices has to equal the identity matrix. To be more precise, (4.11) only holds in the physical subspace, i.e., for the entries corresponding to sheets which are accessible with a given anyon configuration. In the non-physical subspace, the diagonal entries equal zero.

With this knowledge, the effect of the translation of an anyon in positive x -direction across cut B in terms of the diagrams can be derived: In addition to the rules discussed above regarding the translation in x -direction without crossing cut B , upon crossing the cut, the translated anyon is dragged around the non-contractible loop. I.e., the anyon to be translated is first braided with all anyons having the same x -coordinate and a greater y -coordinate. As before, the line associated to this anyon moves in front of the lines of the other anyons fulfilling the mentioned condition. Then, the anyon is dragged around the torus in x -direction and finally braids with all the anyons having the same x -coordinate as and a smaller y -coordinate than the respective final coordinate of the translated anyon. The braiding works again in the same way as before, the translated anyon's line moves behind the lines of these other anyons to a spot such that the order of the anyons coincides with the conventional order associated to the final anyon configuration.

This process is illustrated using an example similar to the one given before for the translation in positive x -direction without crossing cut B . The anyon configuration is depicted on the

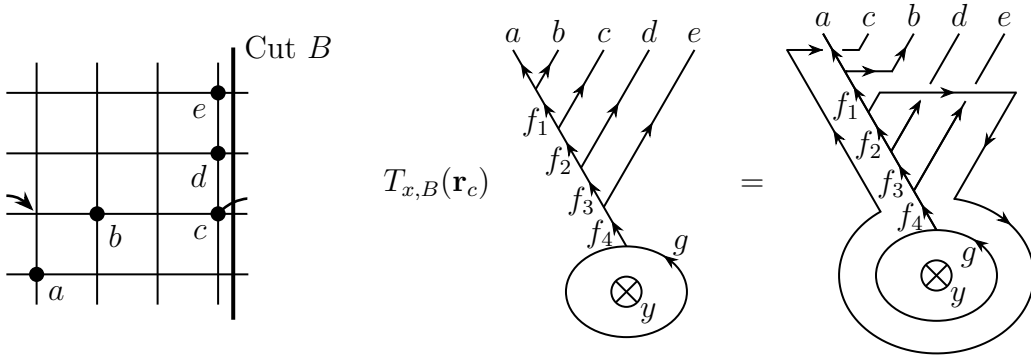


Figure 4.4.: Illustration of the braid rules for translating anyons in positive x -direction across cut B . The lattice on the left shows an anyon configuration and indicates which anyon is to be translated. On the right, the effect of the translation on the fusion diagram is depicted.

left-hand side of Fig. 4.4, the corresponding fusion diagrams on the right-hand side. Anyon c , which is to be translated in positive x -direction, possesses a x -coordinate such that by being translated, it crosses cut B . Anyons d and e possess the same x -coordinates as c on its initial site and greater y -coordinates than the latter. a on the other hand has the same x -coordinate as c in its final position and a smaller y -coordinate than c . The fusion products and the anyon moving along the non-contractible loops are again named f_1 to f_4 and g . $T_{x,B}(\mathbf{r})$ denotes the operator translating the anyon located at position \mathbf{r} over cut B .

These diagrams can be brought back to the form of the basis states' diagrams by first applying B -operators until there are no braids left for the translated anyon before being dragged around the torus. Then, after multiplying the sheet hopping matrix $T_x^s(\{\alpha_k\})$ onto the sheet amplitude vector received in the previous step, the final braids can be resolved by applying B' -operators. As before, the string of operators needed to bring the diagram back to the desired form corresponds to the entries of the matrices $T_{ij}(\{\mathbf{r}_k\}, \{\alpha_k\})$, given cut B is crossed in the translation process. The entry in the m -th row and n -th column is given by the contribution associated to the single diagram in the superposition of diagrams in the result that corresponds to the m -th sheet when the initial state's sheet is the n -th sheet.

The last case to be dealt with occurs when an anyon is translated in positive y -direction over cut A . Similar to the translation over cut B , this scenario corresponds to dragging the anyon around the torus in y -direction. Contrary to the translation in y -direction without crossing this cut, braiding is involved in this case, which can be depicted in the diagrams using the punctured torus S -matrix. This is illustrated again with an example in Fig. 4.5, where we once more consider five anyons (a to e) on a lattice. The fusion products and the anyon moving along the non-contractible loop are labeled f_1 to f_4 and g again. Anyon c is to be translated in positive y -direction over cut A , anyons d and e possess greater x -coordinates than it and anyon a a smaller one. Anyon b has the same x -coordinate as c . $T_{y,A}(\mathbf{r})$ denotes the operator translating the anyon located at position \mathbf{r} over cut A .

By considering the fusion order convention, it is easy to see that in order for the translated

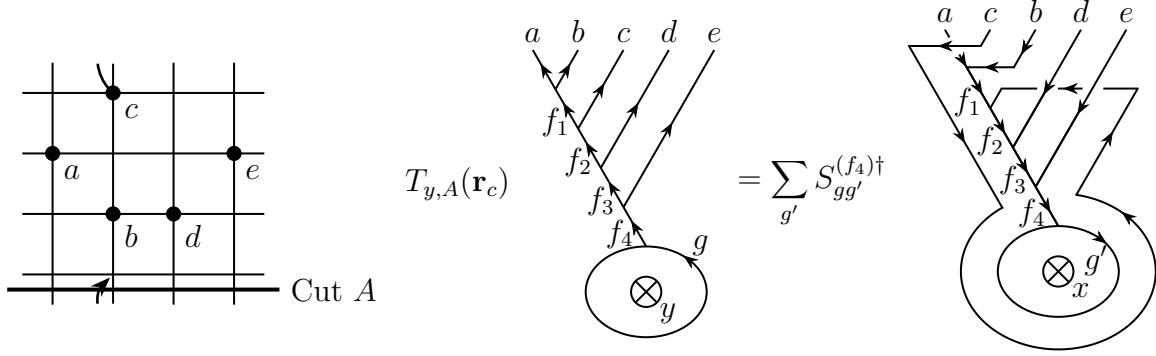


Figure 4.5.: Illustration of the braid rules for translating anyons in positive y -direction across cut A . The lattice on the left shows an anyon configuration and indicates which anyon is to be translated. On the right, the effect of the translation on the fusion diagram is depicted.

anyon to be dragged around the torus, it has to braid with all anyons possessing smaller or bigger x -coordinates: First, the translated anyon has to braid with all the anyons with bigger x -coordinates. Here, the line associated to it in the diagram moves behind the lines of the other anyons meeting the latter condition, as seen in the diagram in Fig. 4.5 for anyons c , d and e . Then, the anyon is dragged around the torus in y -direction and finally braids with the anyons having smaller x -coordinates. In this case, the translated anyon's line moves in front of the other anyons' lines to the spot dictated by the fusion order. This is also shown in Fig. 4.5, where one can also see that the translated anyon c does not braid with anyons that are located in the same column, like anyon b .

Note that due to the transformation with $S^{(f_4)^\dagger}$, the orientation of the lines in the final diagram in Fig. 4.5 is reversed. This does not affect the way the B - and B' -operators act on the diagrams, as the orientation of *every* line is reversed. In order to express such a diagram in terms of diagrams associated to the basis states, B' -operators have to be applied first until there is no braid left for the translated anyon before being dragged around the torus. Then, the same sheet hopping matrix as used before for the translation in x -direction over cut B is applied, followed by the application of B -operators until no braids remain. Finally, after transforming back using the punctured torus S -matrix, the diagram is of the desired form.

Until now, we ignored the fact that an anyon might hop onto an already occupied site. For this scenario, it is important to realize that in order for multiple anyons to be able to exist on the same site, they must not pick up a non-trivial phase when being exchanged. When dealing with identical anyons, this is usually not the case. This can however be relevant for anyons of different charge if one does not explicitly add hard-core interactions. Then, as we will see, one has to take special care when constructing the basis.

Suppose there are two anyons a and b fusing to anyon c located at positions \mathbf{r}_a and \mathbf{r}_b , respectively.

Then, the effect of counter-clockwise exchanging them is given by the R -moves:

$$\psi_{a,b \rightarrow c}(\mathbf{r}_a, \mathbf{r}_b) = R_c^{ab} \psi_{a,b \rightarrow c}(\mathbf{r}_b, \mathbf{r}_a), \quad (4.12)$$

where the first(second) argument in $\psi_{a,b \rightarrow c}$ represents the position of anyon $a(b)$. If both anyons are on the same site, i.e. $\mathbf{r}_a = \mathbf{r}_b$, the wave function can only be non-zero if $R_c^{ab} = 1$, i.e. if the two anyons are mutual bosons. Using this result, it is clear that the algorithm for the different translations described above can also be applied if an anyon is translated onto an already occupied site, given this is allowed by the just discussed constraint. In particular, it does not matter whether or not the anyons on the same site are braided with each other due to $R_c^{ab} = 1$.

It is however important to construct the basis states representing such a lattice configuration in the correct way. In order to do that, it is beneficial to start from a fusion diagram with all anyons located on the same site fusing together and their fusion product then fusing with the intermediate fusion products according to the fusion convention rather than each anyon on the same site fusing one after another with the intermediate fusion products. Such a diagram allows to straight forwardly read off the R -moves corresponding to the above constraint. If one then finds that the constraint is fulfilled for a certain anyon configuration and the fusion products, the diagram can be brought back to the conventional form (3.17) using F -moves. When doing this, it is important to fix an order in which anyons on the same site fuse. The reason is that if two anyons of different charge located on the same site are first exchanged and then brought to the conventional form, the sheet amplitude vector is in general different from the one obtained without exchanging them due to the fact that different intermediate fusion products may be produced. Thus, in order to assure the correctness of the entries in the Hamiltonian, all anyons located on the same site need an additional fusion order.

An example of such a diagram is given by

$$, \quad (4.13)$$

where anyons c and d are located at the same site and the newly introduced on-site fusion order dictates that charge c comes before charge d . The state can only exist if $R_{f_2}^{cd} = 1$ and may be brought to the conventional form by using $[F_{f_3}^{f_1 c d}]_{f_2 f_2'}^{-1}$.

In general, there may of course be more than two anyons on a single site and multiple sites may be occupied by more than one anyon. Then, there essentially are small fusion trees for each of those sites whose fusion products then fuse with the other fusion products of the anyons located at the other sites. The constraint above is then changed such that at each vertex of these fusion

trees for a single site, the corresponding R -move has to equal identity.

Using this consideration, it is clear how the commutation relations of the creation and annihilation operators $c_{\alpha,i}^\dagger$ and $c_{\alpha,i}$ in (4.1) have to look like. As we absorbed all statistical effects into the matrices $T_{ij}(\{\mathbf{r}_k\}, \{\alpha_k\})$, the commutation relations are either bosonic or hard-core bosonic, i.e. $[c_{\alpha,i}, c_{\alpha',j}^\dagger] = [c_{\alpha,i}, c_{\alpha',j}] = [c_{\alpha,i}^\dagger, c_{\alpha',j}^\dagger] = 0$ for all α, α', i, j with $i \neq j$. If two charges α and α' fulfil the above condition in order to exist on the same site, $[c_{\alpha,i}, c_{\alpha',i}^\dagger] = [c_{\alpha,i}, c_{\alpha',i}] = [c_{\alpha,i}^\dagger, c_{\alpha',i}^\dagger] = 0$ holds for the corresponding operators for all i (bosonic). If this is not the case, $\{c_{\alpha,i}, c_{\alpha',i}^\dagger\} = \{c_{\alpha,i}, c_{\alpha',i}\} = \{c_{\alpha,i}^\dagger, c_{\alpha',i}^\dagger\} = 0$ holds for all i (hard-core bosonic).

The algorithm above is constructed in a way that allows to see its equivalence to the already known algorithm for abelian anyons [17] that was discussed in section 2.1 without too much effort. This equivalence is shown in appendix B.

A further comparison among these two algorithms shows that the generalized one can go beyond the limitations of the algorithm for abelian anyons: It can not only simulate non-abelian anyon models, but also an arbitrary amount of distinct anyonic charges on the lattice. Moreover, the statistics' effects can be explained in a very intuitive way by using the fusion diagrams. Finally, there is no arbitrary flux fixing involved, as everything is fully determined by the diagrams.

Note that external fluxes were not explicitly considered in the construction of \mathcal{H} . However, if external fluxes are to be considered, they may for example be incorporated as additional phases $e^{2\pi i \Phi_x / \phi_0}$ or $e^{2\pi i \Phi_y / \phi_0}$ that are acquired when translating an anyon over cut B or A in positive x - or y -direction, respectively, where Φ_x and Φ_y denote the external fluxes and $\phi_0 = hc/e$ the flux quantum [17, 18]. This does however not correspond to a flux fixing condition like in (2.9).

It is possible to construct momentum states that block diagonalize the Hamiltonian (4.1). However, as it turns out that an appropriate discussion is quite technical, the construction is deferred to appendix A.

5. Thermalization of Anyons

Using the generalized algorithm introduced in section 4.2 and momentum states, the tight-binding Hamiltonian (4.1) was simulated for semions and Fibonacci anyons, where we restricted ourselves to periodic lattices corresponding to ladders, i.e. $L_y = 2$. Both the statistical distributions of the energy levels that show level repulsion within the momentum sectors and the behavior of the density distributions after a quench that converge to homogeneous density distributions suggest that these anyons, although only affected by their own statistics, behave like interacting particles.

5.1. Energy Level Spacing Statistics

First, the statistics of the ratios of consecutive energy level spacings r_n [32, 33] were examined, where

$$r_n = \frac{\min\{\delta_n, \delta_{n-1}\}}{\max\{\delta_n, \delta_{n-1}\}}, \quad \delta_n = E_{n+1} - E_n. \quad (5.1)$$

The energy levels E_n are ordered ascendingly, i.e. $\delta_n \geq 0$. It is expected that the level spacing statistics of an integrable Hamiltonian follows the Poisson distribution. For a non-integrable system on the other hand, the statistics is expected to behave like the Wigner-Dyson distribution of the Gaussian orthogonal ensemble (GOE) for time-reversal invariant systems [34].

The Poisson (Poi) and GOE predictions are given by [35]

$$P_{Poi}(r) = \frac{2}{(1+r)^2} \quad \text{and} \quad P_{GOE}(r) = \frac{27}{4} \frac{r+r^2}{(1+r+r^2)^{5/2}}. \quad (5.2)$$

When looking at the distribution of r , it is important to consider the symmetries of the system. Due to the Hamiltonian's translation invariance, momentum states with distinct momentum quantum numbers are decoupled and thus, the corresponding expectation values are conserved. In general, the presence of conserved quantities is expected to coincide with Poisson statistics. On the other hand, if conserved quantities are absent, the energy levels are expected to show level repulsion, which corresponds to Wigner-Dyson statistics. Therefore, if one analyzes the level spacing statistics without restriction to a certain momentum sector, a non-integrable, interacting system may seem to be integrable and non-interacting due to the lack of level repulsion between the energy levels in different momentum sectors [34]. It is thus important to only look at the statistics of the energy levels within a certain momentum sector. As this effect may also occur for spatial reflection symmetries, we will choose the momentum quantum

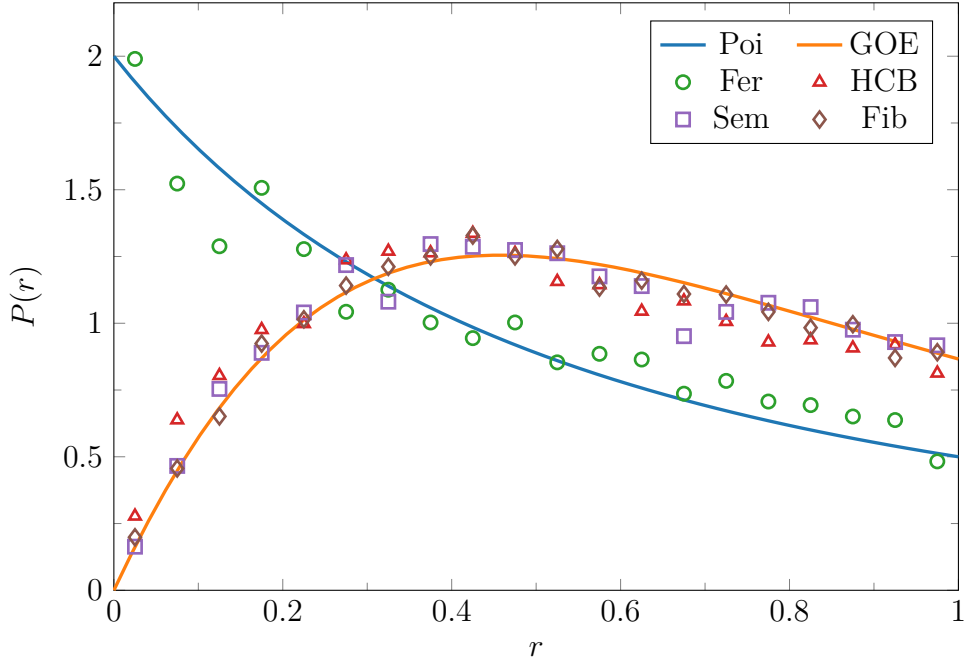


Figure 5.1.: $P(r)$ for fermions on a 40×2 lattice, HCBs with a rung coupling of $r_{\perp} = 0.5$ on a 40×2 lattice, semions on a 32×2 lattice and Fibonacci anyons on a 22×2 lattice in the $k_x = k_y = 1$ sector together with the Poisson and GOE distributions.

numbers for all further investigations to be $k_x = 1$ and $k_y = 1$.

In Fig. 5.1, the Poisson and GOE predictions of r are plotted together with the distributions obtained from exact diagonalization for semions and Fibonacci anyons in the $k_x = k_y = 1$ sector. The distributions for fermions and hard-core bosons (HCBs) are also shown for comparison. For all simulations, the particle number was set to $N = 4$. Due to the total sheet number's dependence on the particle type, different lattice size were used: For fermions and HCBs, a 40×2 lattice was chosen, for semions a 32×2 lattice and for Fibonacci anyons a 22×2 lattice. For HCBs, we slightly modified the Hamiltonian (4.1) in order to obtain better results for the chosen lattice configuration: Due to the trivial statistics, the PBC and $L_y = 2$, each site has a coupling in y -direction to the next site that is twice the coupling to the next site in x -direction. In order to make the system isotropic and avoid unintended effects, we introduced a rung coupling [36] and set it to $r_{\perp} = 0.5$ such that these two couplings agree with each other.

This issue was however ignored for all the other particle types. For fermions, no visible differences in the statistics for the chosen lattice were observed for different rung couplings, which is of course expected due to their non-interacting nature. For the two anyon types, the coupling when translating over cut A gains a phase that depends on the statistics and the anyon configuration of each state, i.e., the same effect as for HCBs is already avoided.

From the results, it can be seen that the distribution of r for fermions follows the Poisson distribution, i.e. shows no level repulsion, which agrees with the expectation. For HCBs, the level spacing statistics has the form of a Wigner-Dyson distribution, in agreement with the fact that HCBs are interacting particles. The distribution of r for both semions and Fibonacci

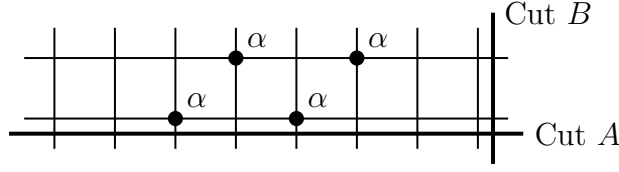


Figure 5.2.: Initial ladder configuration for the quench. $N = 4$ particles of type α are localized in the middle of the ladder in a zigzag pattern in order to avoid unnecessary blocking.

anyons also seem to follow the GOE prediction, suggesting interacting behavior among anyons of the same charge due to their statistics. This also suggests that there are no further symmetries to be exploited in order to further block diagonalize the Hamiltonian apart from the spatial reflection symmetries, which can only be exploited for certain momenta.

5.2. Quench Dynamics

In addition to the level spacing statistics, the Hamiltonian was also studied for a quench, where the density distribution over time was monitored. As before, the lattice was chosen to be a periodic ladder. In the initial state, $N = 4$ particles are localized in the middle of the ladder in a zigzag pattern such that there is one particle per rung and two particles are at most next-nearest neighbors. Such a configuration is depicted in Fig. 5.2 for a 8×2 lattice. The zigzag pattern was chosen since for both of the anyonic charges to be considered, two anyons are not allowed to be on the same site. The zigzag pattern should thus reduce the initial blocking of the inner particles by the outer ones. The n_s -dimensional initial sheet amplitude vector \mathcal{A}_i was set to $\mathcal{A}_i = n_s^{-1/2}(1, 1, \dots, 1)^\top$ for these simulations, where n_s denotes the total sheet number. Such a choice seems natural as we do not want to favor any special fusion realizations.

The particle density is measured for each rung rather than for each site since we are interested in the time dependence of the density along the x -direction. The operator measuring the density in the rung corresponding to the sites with an x -coordinate equal to i at time t is denoted by $n_i(t)$. In order to obtain results that allow for better comparison, the ladder was chosen to have the same size, 30×2 , for all particle types to be considered. In Fig. 5.3, the time dependent particle density $\langle n_i(t) \rangle$ is plotted for fermions, HCBs, semions and Fibonacci anyons. For HCBs, we set the rung coupling to $r_\perp = 0.5$ again.

For the fermionic case, the non-interacting behavior can be seen by the way the density spreads over time. When two wave packages collide, they simply pass through each other due to the lack of interactions. This leads to the density distribution at the final time step $t = 50$ still corresponding to wave packages rather than a homogeneous distribution. This also results in the prominent revivals in the density distribution that remain clearly visible even at larger times. Quite the opposite is observed for HCBs. Due to their interacting behavior, wave packages can not fully pass through each other, which leads to the density distribution becoming more and more homogeneous with increasing time. For semions and Fibonacci anyons, the observed behavior is very similar to the one obtained for HCBs, i.e., the density distribution becomes more homogeneous at larger times.

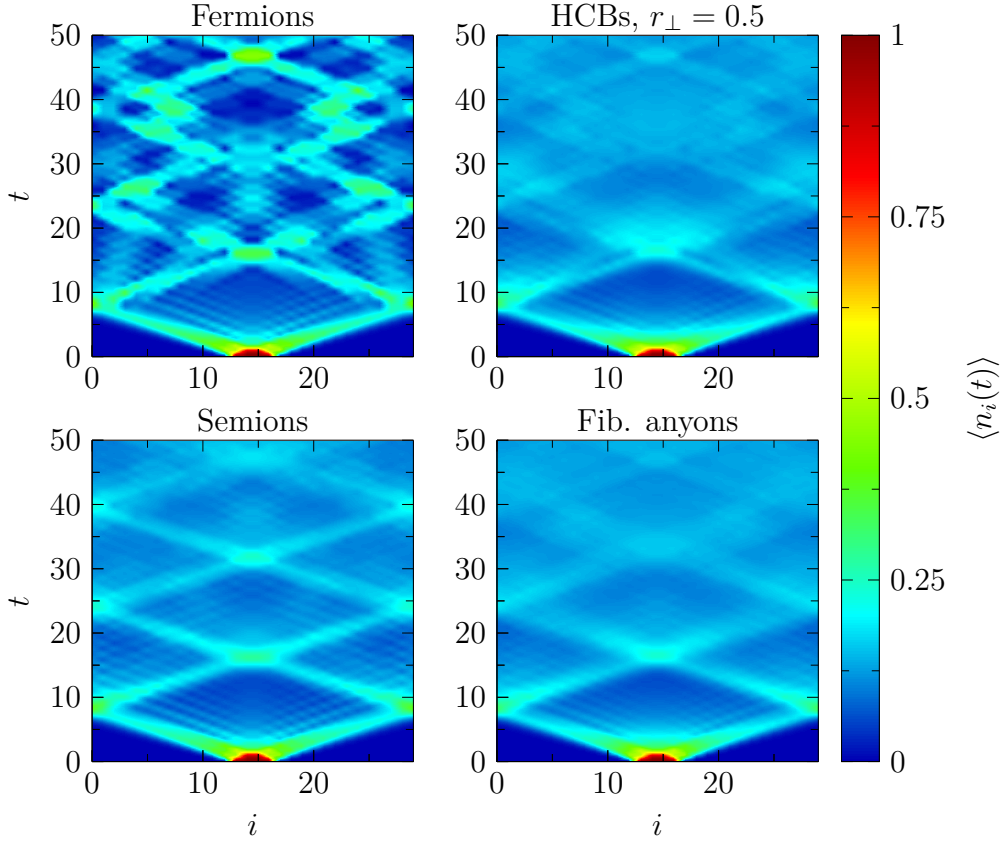


Figure 5.3.: Particle density per rung $\langle n_i(t) \rangle$ for fermions (upper left), HCBs (upper right), semions (lower left) and Fibonacci anyons (lower right) on a 30×2 ladder. Initially, the $N = 4$ particles are localized in the middle of the ladder in a zigzag pattern (see Fig. 5.2), the initial sheet amplitude vector is $\mathcal{A}_i = n_s^{-1/2}(1, 1, \dots, 1)^\top$. For HCBs, the rung coupling was set to $r_{\perp} = 0.5$.

In order to quantify this behavior, we study the density's time averaged squared deviation from its time average [34], i.e.

$$\Delta(T) = \frac{1}{L_x} \sum_i \frac{1}{\bar{n}_i^2 T} \int_0^T dt (\langle n_i(t) \rangle - \bar{n}_i)^2 \quad \text{with} \quad \bar{n}_i = \lim_{T \rightarrow \infty} \frac{1}{T} \int_0^T dt \langle n_i(t) \rangle, \quad (5.3)$$

where we average over all contributions for each rung and normalize each one by \bar{n}_i^2 to obtain a normalized quantity that does not depend on the rung. For ergodic systems, the expectation value of a certain operator is close to its time averaged expectation value (which agrees with the ensemble predictions) at almost all points in time in the long time limit [34, 37]. I.e., $\lim_{T \rightarrow \infty} \Delta(T)$ is expected to vanish in the limit of infinite system sizes for ergodic systems.

The behavior of $\Delta(T)$ is shown in Fig. 5.4 for fermions, HCBs, semions and Fibonacci anyons for the system sizes $L_x = 22, 26, 30$ and $L_y = 2$, where \bar{n}_i was approximated by $\bar{n}_i \approx \bar{n}_i(T_{max}) \equiv \frac{1}{T_{max}} \int_0^{T_{max}} dt \langle n_i(t) \rangle$ with the maximum simulation time $T_{max} = 10^4$. In this plot, the smaller system sizes correspond to brighter tones. It can be seen that for fermions,

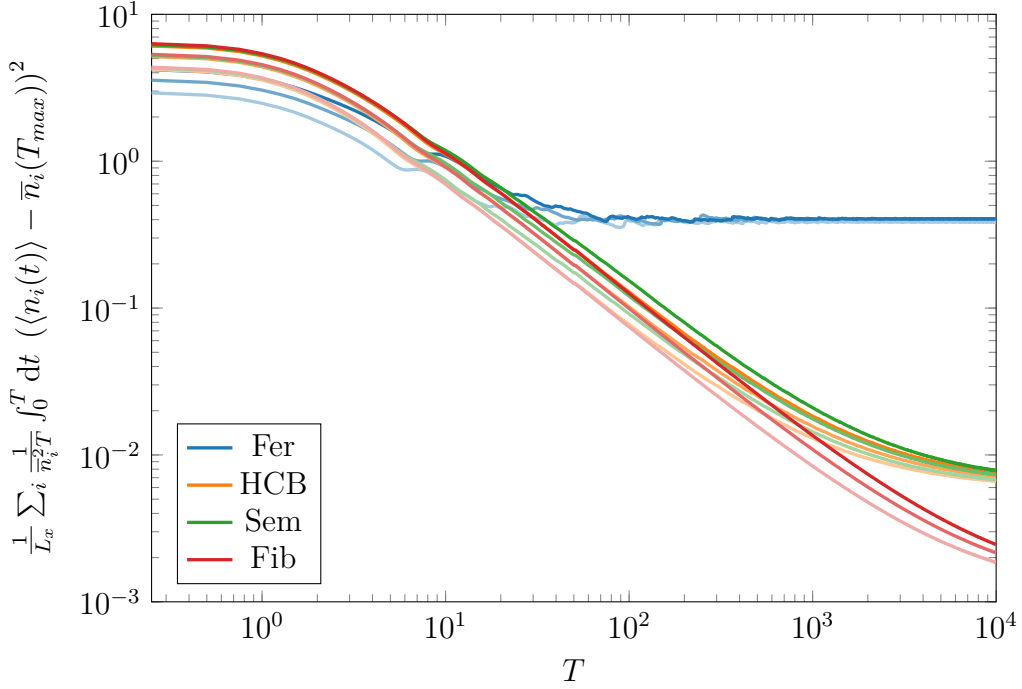


Figure 5.4.: $\frac{1}{L_x} \sum_i \frac{1}{n_i^2 T} \int_0^T dt (\langle n_i(t) \rangle - \bar{n}_i(T_{max}))^2 \approx \Delta(T)$ for fermions, HCBs, semions and Fibonacci anyons on a ladder with $L_x = 22, 26, 30$ and $L_y = 2$. Smaller system sizes correspond to brighter tones. In the initial state, $N = 4$ particles are localized in the middle of the ladder as depicted in Fig. 5.2. The initial sheet amplitude vector is $\mathcal{A}_i = n_s^{-1/2}(1, 1, \dots, 1)^\top$. For HCBs, the rung coupling was set to $r_\perp = 0.5$ again.

$\Delta(T)$ does not converge to smaller values for higher system sizes. In addition to that, the converged values for $\Delta(T)$ are only slightly smaller than 1, i.e., they are of the same magnitude, $\Delta(T) \lesssim 1$ for large T . However, if a given system thermalizes, i.e., the expectation value of an operator relaxes to its time averaged expectation value that also agrees with the statistical ensemble predictions, the relative deviations from this time averaged expectation value are expected to be small, i.e., $\Delta(T) \ll 1$ would be expected to hold for the converged value of $\Delta(T)$. This follows from the eigenstate thermalization hypothesis [34, 38] and the quantum ergodic theorem [39, 40].

It can be thus concluded that the fermions' density distribution does not converge to its time averaged value for large times, i.e., the fermionic system does not thermalize, which is expected due to their non-interacting nature. The observations for HCBs, semions and Fibonacci anyons stand in contrast to this: $\Delta(T) \ll 1$ is fulfilled at large enough T for all three of the particle types, i.e., despite $\Delta(T)$ not being fully converged in Fig. 5.4, it can be concluded that the density distribution converges to its time average at large times, hinting at thermalization.

Note that values of $\Delta(T)$ (for large T) for Fibonacci anyons are significantly smaller than those for HCBs and semions. One reason for this might be found in the size of the Hilbert spaces: For identical ladders, the size of the Hilbert space for Fibonacci anyons equals the size of the Hilbert space for HCBs (semions) times 7 (7/2). Thus, if $\Delta(T)$ converges to zero for infinite system

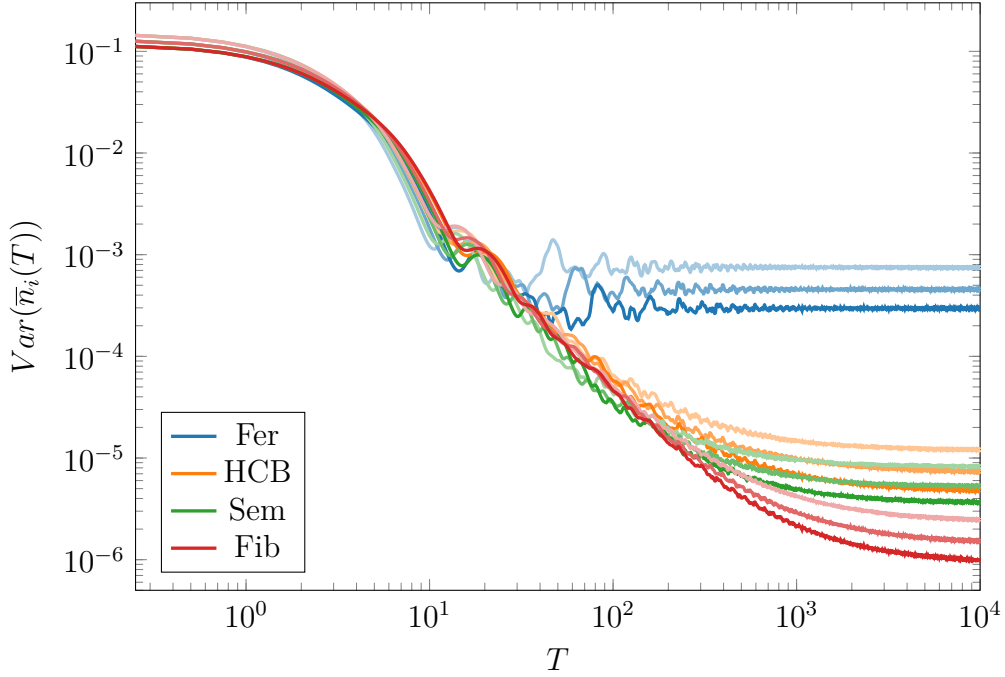


Figure 5.5.: Variance of $\bar{n}_i(T)$ for fermions, HCBs, semions and Fibonacci anyons on a ladder with $L_x = 22, 26, 30$ and $L_y = 2$. Smaller system sizes correspond to brighter tones. In the initial state, $N = 4$ particles are localized in the middle of the ladder as depicted in Fig. 5.2. The initial sheet amplitude vector is $\mathcal{A}_i = n_s^{-1/2}(1, 1, \dots, 1)^\top$. For HCBs, the rung coupling was set to $r_\perp = 0.5$ again.

/ Hilbert space sizes, it is intuitive that the converged values on identical (finite) ladders are smaller for Fibonacci anyons due to their larger Hilbert space. Another reason might be that for Fibonacci anyons, $\Delta(T)$ simply converges faster to its limit due to their statistics. In [41], it was found that for hard-core abelian anyons in 1D governed by a tight-binding Hamiltonian, all one-body observables converge faster to their limit if the anyonic statistics are closer to HCBs, i.e., if the phase acquired upon exchanging two anyons is smaller. Something similar seems to be happening in our case, as the Hilbert space for Fibonacci anyons on a 22×2 lattice is comparable to the Hilbert space for semions on a 30×2 lattice in size, i.e., the different Hilbert space sizes can not be responsible for the difference in convergence in this case.

In order to conclude that the time averaged density distributions that the systems for HCBs, semions and Fibonacci anyons converge to are indeed homogeneous, we take a closer look at their variances $Var(\bar{n}_i(T))$ as function of time T . These variances are depicted in Fig. 5.5 for these particle types and for fermions for the same system sizes as above. It is observed that for all particle types, the variance becomes smaller for larger system sizes, i.e., the time averaged density distribution becomes more homogeneous.

Similar to Fig. 5.4, it can be seen that the values for fermions are significantly larger than those corresponding to the other particle types. The reason for this is that for the fermionic systems, the density distribution does not converge to a stationary one, as discussed above. This leads to larger variances due to oscillations in the density distribution despite its time average

converging to a homogeneous distribution. It is again observed that there are differences in the converged values for the other particle types, which might be explained by the already discussed arguments.

Finally, we note that results very similar to those discussed in Fig. 5.3, 5.4 and 5.5 are obtained for other choices of initial sheet amplitude vectors \mathcal{A}_i , i.e., the above observations seem to be general for a quench with localized particles. It is thus concluded that semions and Fibonacci anyons on a 2D ladder seem to behave similar to interacting particles / HCBs if their dynamics are governed by a tight-binding Hamiltonian that merely accounts for their statistics. This is not only based on their energy level spacing statistics, but also on the fact that their density distribution after a quench converges to its time averaged value that becomes homogeneous in the limit of infinite time and system size.

A similarly interesting observation was made for 1D systems of hard-core abelian anyons of arbitrary statistics governed by the anyonic tight-binding Hamiltonian [41]. It was found that for quenches, one-body observables relax to the predictions of the generalized Gibbs ensemble for all abelian statistics (including HCBs) except for fermionic ones, suggesting that abelian anyons behave similarly to HCBs. This observation for 1D systems is consistent with what we found for semions on 2D ladders. Furthermore, based on our results for Fibonacci anyon model, the same seems to hold for non-abelian anyons.

In [19], abelian and non-abelian anyons on a 2D ladder governed by an anyonic tight-binding Hamiltonian were simulated. The key difference to our simulations is that in [19], only one anyon was allowed to move; all other anyons were pinned to the spaces in between the lattice sites. Looking at the transport properties, it was found that for non-abelian Ising anyons with both uniformly and randomly distributed background anyonic charges, the system features dispersive transport. For an abelian anyon model with uniformly distributed background anyons however, the system was found to exhibit ballistic transport. This result is a consequence of the chosen setup, as it was shown that for randomly distributed anyonic backgrounds, abelian anyons localize [42]. We thus see that although the thermalizing behavior discussed above seems to connect HCBs with abelian and non-abelian anyons, the different types may still behave very differently in other contexts.

6. The Spectral Function

Until now, we looked at anyonic systems solely from a theoretical point by constructing Hamiltonians from microscopic models and analyzing simulation results. Although we found that there is interacting behavior to be expected for anyonic systems that are governed by their own statistics, we still lack an experimentally observable property that can be used in order to distinguish between distinct anyonic systems. It turned out that the differential cross-section's behavior close to the threshold of creating two free anyons can be used as such a property, which is experimentally accessible in scattering experiments. This threshold behavior has already been studied both analytically and numerically for abelian anyons and was found to depend on the anyons' statistics [20]. I.e., it can in principle be used to distinguish distinct anyonic systems. Thus, we will also study this very property in the following and look at three different things: Firstly, the threshold behavior for non-interacting particles is studied in order to test our new numerical method / generalized algorithm by comparing the results to the expected threshold behavior discussed in [20]. Secondly, we study the effect of interactions on the threshold behavior more in-depth. Especially the consideration of long-range interactions is of interest due to Wigner finding that such interactions affect the cross section's threshold behavior in 3D [43]. For these two parts, we restrict ourselves to abelian anyons and compare the lattice simulations to continuous ones. Thirdly, the threshold behavior for non-interacting Fibonacci anyons is studied using only lattice simulations as there is currently no appropriate method for simulating non-abelian anyons using differential equations. The underlying idea for all these discussions is that the anyonic tight-binding Hamiltonian generated by the algorithm in section 4.2 serves as minimal model for anyon dynamics in real physical systems.

For e.g. inelastic neutron scattering experiments performed on gapped spin liquids, the differential cross-section $d^2\sigma/d\Omega d\omega$ is proportional to the dynamic structure factor $S^{\alpha\beta}(\mathbf{q}, \omega)$, with $\alpha, \beta \in \{x, y, z\}$ [44]. Due to the excitations being gapped, we can restrict ourselves to subspaces of fixed particle numbers and compute $S(\mathbf{q}, \omega)$ therein [20]. The underlying assumption for this is that the considered energies are not large enough in order to create additional particles, which is of course fulfilled when looking at the threshold behavior.

6.1. Definition and Basic Properties

Here, we will focus on the case of inelastic scattering that creates two anyons in the system, which corresponds to the non-trivial scenario with the lowest energy. To see that the creation of a single anyon is indeed trivial, we note that this process is not always allowed in the first place. But even if it is allowed, the spectral function for a single anyon does not depend on its statistics since there is only one anyon in the system and the sheet can not be changed (see the

corresponding rules in section 4.2).

The zero temperature spectral function to be examined can thus be written as ($\hbar \equiv 1$ from now on) [20]

$$S(\mathbf{q}, \omega) = \sum_{|\psi_f\rangle} \left| \langle \psi_f | O_{\mathbf{q}} | \psi_i \rangle \right|^2 \delta(\omega + \omega_i - \omega_f) \quad (6.1)$$

$$= -\frac{1}{\pi} \text{Im} \langle \psi_i | O_{\mathbf{q}}^\dagger \frac{1}{i\epsilon + \omega + \omega_i - \mathcal{H}} O_{\mathbf{q}} | \psi_i \rangle. \quad (6.2)$$

$|\psi_i\rangle$ is the initial state that does not feature any excitations and $|\psi_f\rangle$ are the two-anyon eigenstates of the Hamiltonian given by (4.1) on the lattice and (2.30) in continuous space. For the former, the interaction discussed in section 2.2 will also be added such that it indeed corresponds to the lattice version of (2.30). $O_{\mathbf{q}}$ denotes the Fourier transform of the operator $O(\mathbf{R})$ that creates two excitations which have a distance of a in between them; their center of mass is given by \mathbf{R} . While the natural choice of a is one lattice spacing for the lattice simulations, it may be arbitrarily set to unity for the continuous simulations since it does not influence the threshold behavior. We further used the well known relation $(x \pm i\epsilon)^{-1} = x^{-1} \mp i\pi\delta(x)$ with the implicit limit $\epsilon \rightarrow 0^+$. Equation (6.2) can be used to numerically compute $S(\mathbf{q}, \omega)$ for the lattice simulations using the continued fraction method [45]. For the continuous simulations, $S(\mathbf{q}, \omega)$ can be evaluated using [20]

$$S(\mathbf{q}, \omega) \propto \sum_{|\psi_f\rangle} \left| \int d\mathbf{R} d\varphi e^{i\mathbf{q}\cdot\mathbf{R}} \langle \psi_f | \mathbf{R}, a, \varphi \rangle \right|^2 \delta\left(\omega - \frac{k^2}{m} - \frac{\mathbf{K}^2}{4m} - \Delta\right) \quad (6.3)$$

$$\propto \frac{m}{2\sqrt{\Omega}} \left| \psi(a, \sqrt{\Omega}) \right|^2 \Theta(\Omega), \quad (6.4)$$

with $O(\mathbf{R})|\psi_i\rangle = \int d\varphi |\mathbf{R}, a, \varphi\rangle$. k and \mathbf{K} are again the momenta corresponding to the relative and center of mass coordinates, Δ is the energy needed to create the two anyonic excitations. We used a similar ansatz as in (2.28) for the wave function

$$\langle \psi_f | \mathbf{R}, a, \varphi \rangle = e^{i\mathbf{K}\cdot\mathbf{R}} e^{il\varphi} \psi(r, k), \quad (6.5)$$

where all normalization factors are absorbed into $\psi(r, k)$. From the \mathbf{R} and φ integrations, it follows that $\mathbf{K} = -\mathbf{q}$ and $l = 0$. The latter is simply a consequence of the definition of $O(\mathbf{R})$, where we focus on s -wave states that dominate at low energies, i.e. at the threshold. Substituting the sum $\sum_{|\psi_f\rangle}$ by the corresponding integral yields an additional factor of $m/2\sqrt{\Omega}$ from the δ -function with $\Omega = k^2 = m(\omega - \Delta) - \mathbf{q}^2/4$. $\Theta(\Omega)$ assures that there is a large enough energy transfer into the system in order to excite the state characterized by the above quantities. $\psi(r, k)$ can be obtained numerically by following the procedure discussed in section 2.3. The eigenvalue of the Hamiltonian is of course simply given by Ω .

For the non-interacting case, i.e. the wave function in (6.5) is given by (2.28), (6.4) simplifies to

[20]

$$S(\mathbf{q}, \omega) \propto m J_\alpha^2(a\sqrt{\Omega}) \Theta(\Omega) \quad (6.6)$$

$$\approx m(a^2\Omega)^\alpha \Theta(\Omega), \quad (6.7)$$

where an approximation for small arguments was made in the final step. α corresponds to the statistical parameter again. This result will be used as reference for the threshold behavior of non-interacting abelian anyons and fermions. For bosons however, $S(\mathbf{q}, \omega)$ takes a different form due to the absence of statistical repulsion making them susceptible to e.g. short-ranged hard-core interactions [20]. Thus, bosons will not be considered in the following parts.

There is an important remark to be made about $|\psi_i\rangle$ in (6.1). As mentioned, $|\psi_i\rangle$ does not feature any excitations. However, this does not mean that this state is unique (as can be seen by the considerations regarding sheets in 4.1). It was however numerically verified for the lattice simulations that the considered abelian anyon models yield the same qualitative results for different choices of $|\psi_i\rangle$. For all the following (lattice simulation) results to be discussed, we thus chose a convention in which the different sheets in $|\psi_i\rangle$ have identical prefactors, i.e. no sheet is favored. For the same reason, we can restrict ourselves to the solution of a Schrödinger equation that does not feature any sheets for the continuous simulations.

Since we are mainly interested in the threshold behavior, we numerically computed the results of $S(\mathbf{q}, \omega)$ for $\mathbf{q} = \mathbf{0}$, which corresponds to the case in which the two anyons' center of mass motion has zero energy / momentum. We further set the mass m in (2.30) to $m = 1$ and (as already mentioned) $a = 1$. For the lattice simulations, the hopping parameter in (4.1) is set to 1 by default. I.e., the typical energy scale for lattice systems that should be given by $(2ma^2)^{-1}$ is also set to unity. This means that when setting the lattice spacing to unity, all the energies for the lattice simulations are doubled compared to the continuous simulations. Thus, for all the following lattice simulations, the Hamiltonians obtained according to (4.1) were multiplied by 0.5 in order to compensate for the doubling such that the energy scales for the lattice and the continuous simulations agree.

In Fig. 6.1, $S(\mathbf{q} = \mathbf{0}, \omega)$ is plotted for non-interacting fermions and semions on a 40×40 lattice, where the dashed lines correspond to the expected non-interacting threshold behavior in (6.7). In order to get a better view of the threshold behavior, $S(\mathbf{q} = \mathbf{0}, \omega)$ was rescaled for both particle types such that the graphs intersect at uninteresting coordinates. This is also done for all further plots of $S(\mathbf{q} = \mathbf{0}, \omega)$ for both the lattice and the continuous simulations. Although the agreement with the predicted threshold behavior for $0.2 \lesssim \Omega \lesssim 2$ is remarkable for both particle types, there are clear deviations from it for smaller energies in the fermionic case. The reason for these deviations can be found in the utilized numerical method: $S(\mathbf{q} = \mathbf{0}, \omega)$ is computed according to (6.2) by using the continued fraction method, where the choice of ϵ plays a key role. Large values of ϵ smoothen the oscillations in the obtained spectral functions and strengthen the observed "tail" at low energies due to the Lorentzian decay in the imaginary part in (6.2). Small values on the other hand amplify the oscillations and dampen the tail. It turns out that also for semions, the behavior for small Ω is determined by such a tail; it just agrees by chance with the expectation, which can be verified by looking at Fig. 6.3 in the next section.

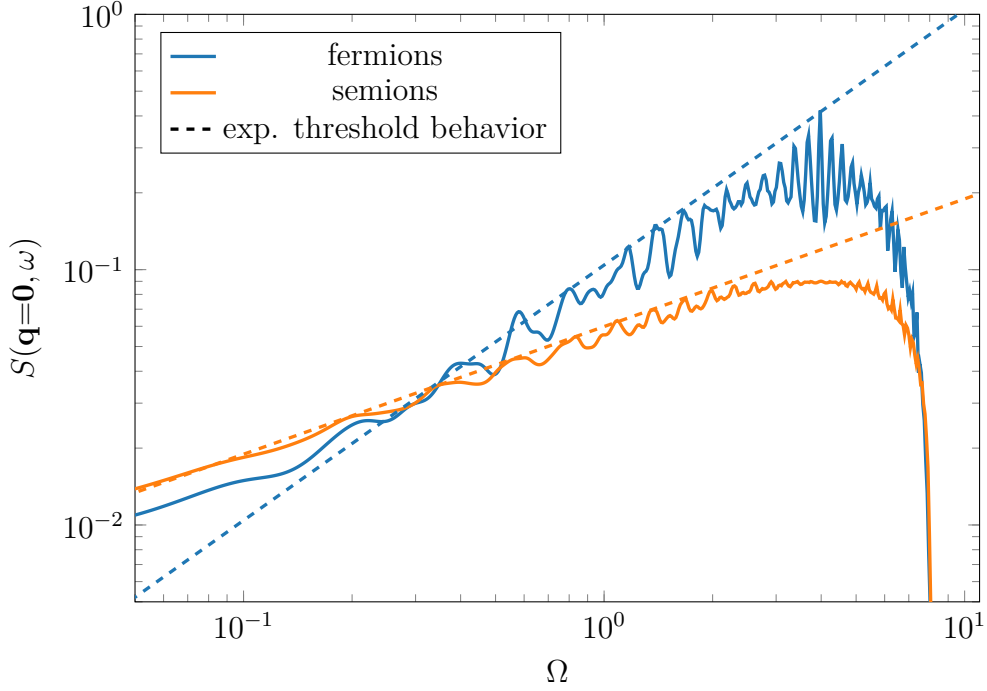


Figure 6.1.: Simulated threshold behavior of $S(\mathbf{q} = \mathbf{0}, \omega)$ for non-interacting fermions and semions on a 40×40 lattice and expected threshold behavior at low energies (dashed).

We chose $\epsilon = 0.05$ for all the plots obtained from lattice simulations such that the oscillations and the threshold behavior at larger energies can be observed. Choosing smaller values for ϵ does not add any benefits as with stronger oscillations, the threshold behavior is harder to verify at larger energies. At the same time, the density of states at low energies is too small for the accessible system sizes in order to reliably compare the numerics to the predictions, i.e., the dampened tails can not be used to verify the threshold behavior. Thus, tails similar to those in Fig. 6.1 will be present in all the following plots that were obtained from the lattice simulations and the threshold behavior will be studied for moderate energy ranges rather than low ones.

It can be further observed that the oscillations of the semionic spectral function are not as prominent as those of the fermionic one. This can be seen very clearly when looking at the spectral functions' maxima. The reason for this is not the different Hilbert space dimensions due to the sheet numbers being different. The distinct behavior was found to persist even when adjusting the lattice size for the semionic case such that the corresponding Hilbert space dimension approximately agrees with the fermionic case's. We thus infer that the different exchange statistics cause the distinct behaviors in the oscillations.

Moreover, it is interesting that the critical energy beyond which the spectral function starts to significantly deviate from the threshold behavior is slightly smaller for semions. This can be explained by using (6.6). Expanding the Bessel function $J_\alpha(x)$ for small arguments to the subleading term that is of order $\mathcal{O}(x^{\alpha+2})$ [46] reveals that the first correction to the threshold behavior is of order $\mathcal{O}(\Omega^{\alpha+1})$. I.e., the subleading contribution for semions ($\alpha = 0.5$) starts

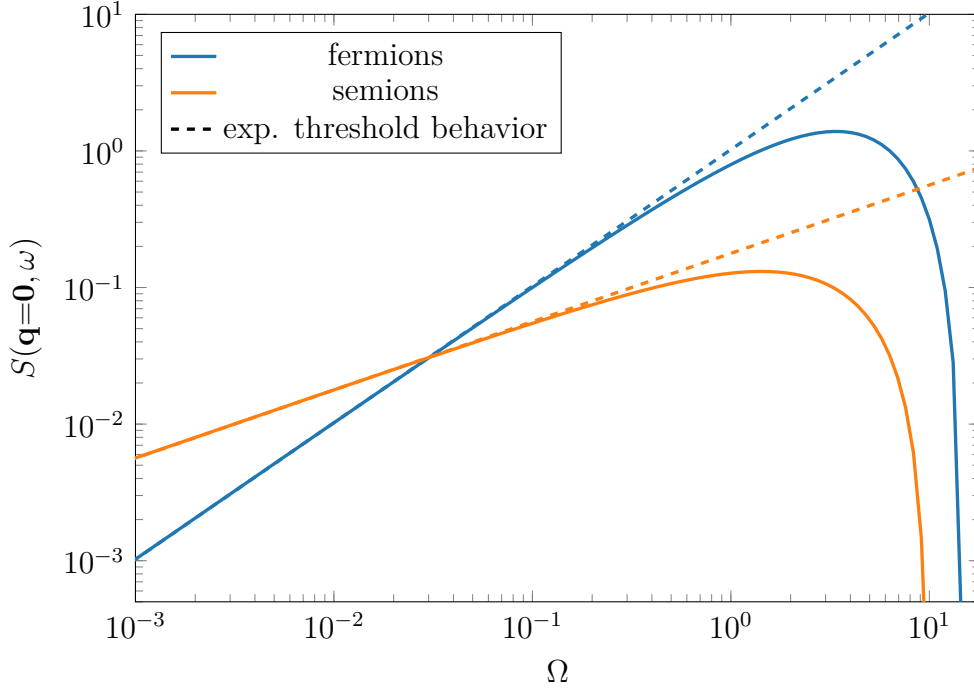


Figure 6.2.: Simulated threshold behavior of $S(\mathbf{q} = \mathbf{0}, \omega)$ for non-interacting fermions and semions from numerically solving the differential equation and the expected threshold behavior at low energies order (dashed).

to become relevant at smaller Ω compared to the fermionic case ($\alpha = 1$), which explains the observed behavior.

In Fig. 6.2, the same spectral functions as above are plotted for the continuous simulations, where the predictions for the threshold behaviors were added again as dashed lines. Due to the numerical method, the results show neither any oscillations nor any tails. Further, due to lack of relevance, the part of $S(\mathbf{q} = \mathbf{0}, \omega)$ beyond the first minimum is not depicted. This will be similar for all the following plots obtained from the continuous simulations. It can be seen that the threshold behaviors perfectly agree with the expectations for small Ω . As the method allows to reach arbitrarily small energies, the chosen energy range features a significantly smaller lower bound than the one in Fig. 6.1. Because of the rescaling of the energy scale for the lattice simulations mentioned above, the energies at which the spectral functions rapidly decay approximately agree among the two simulation types. That together with the agreement of the spectral functions' behaviors in both figures confirm that the simulations indeed correspond to the discrete and continuous versions of the same system.

With this confirmation and the reproduction of the known behaviors, it is time to use both methods in order to examine the effect of (long-range) interactions on the threshold behavior more in-depth.

6.2. The Effect of Interactions on the Spectral Function's Threshold Behavior

Interactions alter the wave function and by doing so, they may also affect the threshold behavior of the spectral function. Wigner showed that in 3D, the threshold behavior is changed for interactions $\propto r^{-2-\epsilon}$, $\epsilon \leq 0$, whereas for $\epsilon > 0$, it remains unaffected [43].

In the following, it will be shown that this also holds in 2D using the same argument as Wigner did in the 3D case and that even in the special case of interactions $\propto r^{-1}$, in which the threshold behavior is changed, the non-interacting expectation may still be observed within a certain energy range if the interaction amplitude is small enough.

The considered interactions that are added on top of the already introduced statistical interaction will be written as $Ur^{-(2+\epsilon)}$, such that the Schrödinger equation reads

$$\left(-\frac{d^2}{dr^2} - \frac{1}{r} \frac{d}{dr} + \frac{(l-\alpha)^2}{r^2} + \frac{U}{r^{2+\epsilon}} - \Omega\right) \psi(r, \sqrt{\Omega}) = 0, \quad (6.8)$$

which is obtained by plugging the interaction into equation (2.30) and choosing the eigenvalue of $\psi(r, \sqrt{\Omega})$ to the Hamiltonian to be Ω , in agreement with the notation used above. As in the previous section, we set $\hbar = m = 1$. For the lattice simulations, it is important to note that only the Hamiltonian (4.1) is rescaled by a factor of 0.5 in order to obtain the same energy scale as for the continuous simulations; the interaction strength U is not affected.

There are three qualitatively different cases that will be discussed here, namely $\epsilon = 0$, $\epsilon > 0$ and $\epsilon < 0$, where additional insights will be provided for the special case $\epsilon = -1$ as it is of particular interest due to its Coulomb-like interaction.

6.2.1. The Case $\epsilon = 0$

For $\epsilon = 0$, the additional interaction has the same form as the statistical interaction and thus, the solution to (6.8) can be obtained by substituting $(l-\alpha)^2 \rightarrow (l-\alpha)^2 + U$ in (2.28), i.e. $\psi(r, \sqrt{\Omega}) \propto J_{\sqrt{(l-\alpha)^2+U}}(\sqrt{\Omega}r)$. From the expansion of the Bessel function for small arguments discussed previously, it follows that the threshold behavior is expected to change from $\propto \Omega^\alpha$ to $\propto \Omega^{\sqrt{\alpha^2+U}}$.

This is confirmed by the lattice simulation results that are plotted in Fig. 6.3 for semions on a 40×40 lattice for $U = 0.25$, $U = 0.5$ and $U = 1$. The non-interacting case $U = 0$ is also plotted for comparison. It can be seen that $S(\mathbf{q}=\mathbf{0}, \omega)$ agrees with the expected threshold behavior over an extended energy range for all interaction strengths U . For low Ω , there are deviations from this expectation for all but the non-interacting case. This is, as discussed above, an effect of the numerical method that was used in order to compute $S(\mathbf{q}=\mathbf{0}, \omega)$ and thus confirms this argument.

Similar to the lattice simulations, the results obtained from the continuous simulations show very good agreement with the expected threshold behavior. Due the numerical method, this agreement is also visible at the lowest energies. This can be seen in Fig. 6.4 for the same

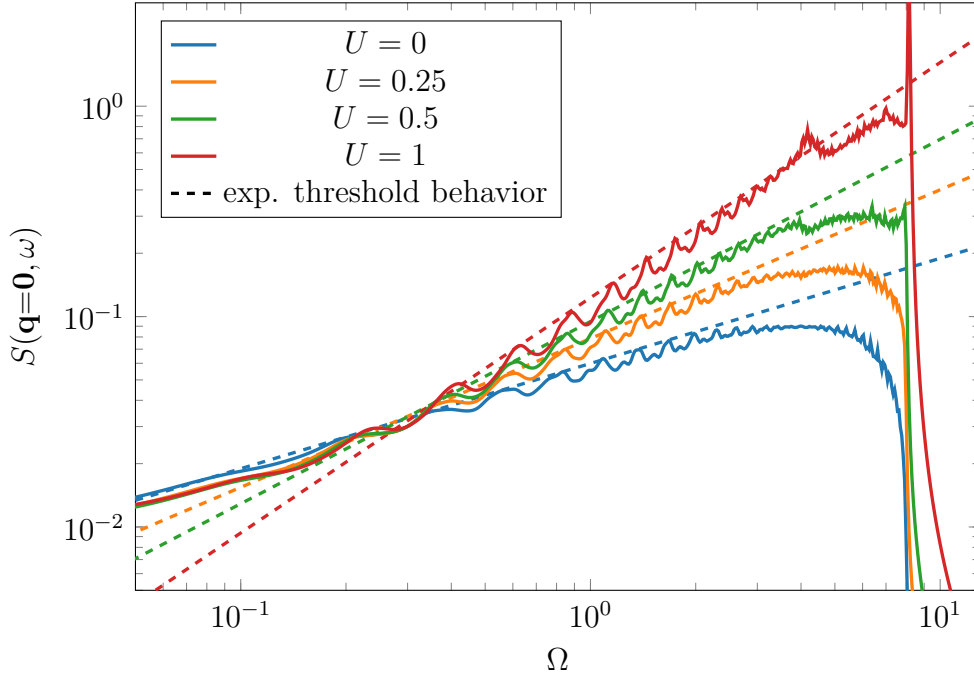


Figure 6.3.: Simulated behavior of $S(\mathbf{q}=\mathbf{0}, \omega)$ for semions with an additional interaction Ur^{-2} for $U = 0, 0.25, 0.5, 1$ on a 40×40 lattice and the corresponding expected threshold behaviors (dashed).

interaction strengths as above, i.e. for $U = 0, 0.25, 0.5, 1$.

6.2.2. The Case $\epsilon > 0$

Similar to Wigner's argument in 3D [43], one can also argue in 2D that the threshold behavior should not be affected by interactions $\propto r^{-(2+\epsilon)}$, $\epsilon > 0$. In appendix C, the following relation between the solution $\bar{\psi}(r)$ to (6.8) and the solution $\psi(r)$ to the same equation with the difference of setting $U = 0$ is derived (we suppress the Ω -dependency here for convenience):

$$\begin{aligned} \frac{\bar{\psi}(r)}{\psi(r)} = 1 + \int_r^\infty \frac{dr'}{(r'\psi(r'))^2} \int_{r'}^\infty dr'' (r''\psi(r''))^2 V(r'') \frac{\bar{\psi}(r'')}{\psi(r'')} \\ + \int_r^\infty \frac{dr'}{(r'\psi(r'))^2} \int_{r'}^\infty dr'' r''\psi(r'')^2 \frac{d}{dr''} \frac{\bar{\psi}(r'')}{\psi(r'')}, \end{aligned} \quad (6.9)$$

where $V(r) = Ur^{-2-\epsilon}$ and it was assumed that $\lim_{r \rightarrow \infty} \bar{\psi}(r)/\psi(r) = 1$. In appendix D, it is shown that (for $\epsilon > 0$) in the large r asymptotic expansion, the first deviation of $\bar{\psi}(r)$ from $\psi(r)$ is at order $\mathcal{O}(r^{-(1+\epsilon)})$ compared to the leading order term, which justifies this assumption as $\bar{\psi}(r)/\psi(r) = 1 + \mathcal{O}(r^{-(1+\epsilon)})$ follows. The reason for the leading order of this ratio being one and not another constant can be found when looking at the normalization of both wave functions. It is known from the asymptotic expansion that both $r|\psi(r)|^2$ and $r|\bar{\psi}(r)|^2$ become constant for large r . Thus, from the normalization constraints $\int_0^\infty dr r|\psi(r)|^2 = 1 = \int_0^\infty dr r|\bar{\psi}(r)|^2$ it is clear

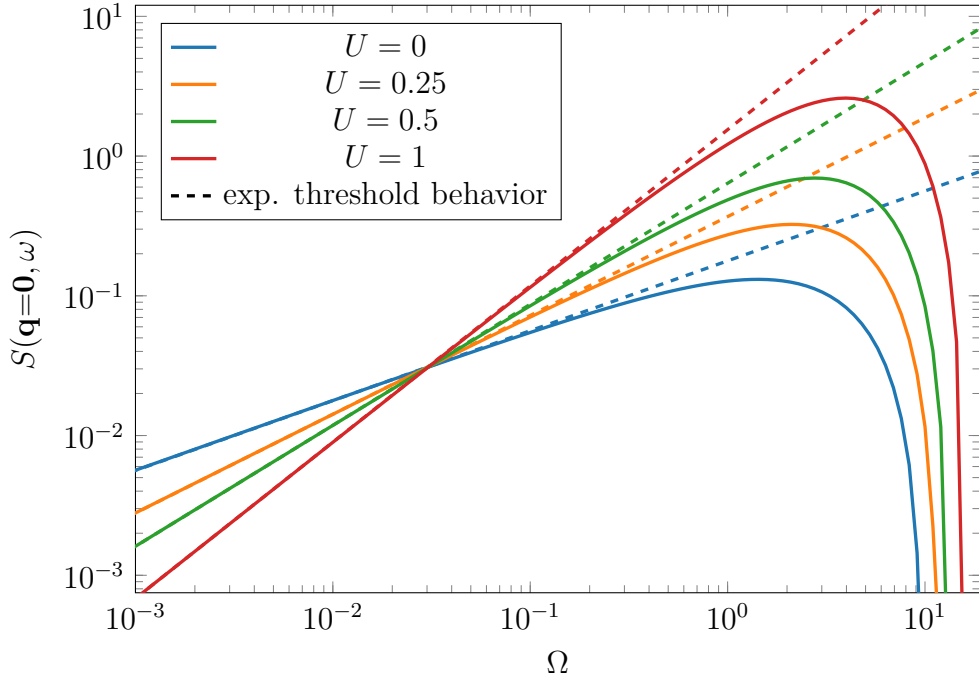


Figure 6.4.: Simulated behavior of $S(\mathbf{q}=\mathbf{0}, \omega)$ for semions with an additional interaction $U r^{-2}$ for $U = 0, 0.25, 0.5, 1$ obtained by numerically solving the Schrödinger equation and the corresponding expected threshold behaviors (dashed).

that the normalization constants are dominated by the leading orders of the large r expansions and therefore, these leading orders (including the prefactors from the normalization) have to be identical, i.e. their ratio is one up to higher order corrections.

As a change in the threshold behavior would also result in a change of the wave function itself, it seems that if both integrals on the right-hand side of (6.9) converge and go to zero in the limit of large r with $\bar{\psi}(r)/\psi(r) \rightarrow 1$, the threshold behavior remains unaffected by the additional interaction $V(r)$ [43].

This can be shown by bounding the absolute values of the integrals using $\psi(r) \approx c e^{i k r} / \sqrt{r}$, $\bar{\psi}(r) \approx c e^{i k r} / \sqrt{r}$, $\bar{\psi}(r)/\psi(r) \approx 1$ and $d/dr (\bar{\psi}(r)/\psi(r)) \approx -a(1+\epsilon)r^{-(2+\epsilon)}$, with some constants a and c . This is sufficient as none of the (subleading) corrections can change the leading order. The results of the calculations are

$$\left| \int_r^\infty \frac{dr'}{(r'\psi(r'))^2} \int_{r'}^\infty dr'' (r''\psi(r''))^2 V(r'') \frac{\bar{\psi}(r'')}{\psi(r'')} \right| \leq \int_r^\infty \frac{dr'}{r'} \int_{r'}^\infty dr'' r'' \frac{U}{(r'')^{2+\epsilon}} = \frac{U}{\epsilon^2 r^\epsilon} \quad \text{and} \quad (6.10)$$

$$\left| \int_r^\infty \frac{dr'}{(r'\psi(r'))^2} \int_{r'}^\infty dr'' r'' \psi(r'')^2 \frac{d}{dr''} \frac{\bar{\psi}(r'')}{\psi(r'')} \right| \leq \int_r^\infty \frac{dr'}{r'} \int_{r'}^\infty dr'' |a|(1+\epsilon) (r'')^{-(2+\epsilon)} = \frac{|a|}{(1+\epsilon)r^{1+\epsilon}}.$$

With these computations, it can be seen that for $\epsilon > 0$, the right-hand side of (6.9) does indeed go to one for large r , i.e. $\bar{\psi}(r)/\psi(r) \rightarrow 1$ for large r and thus, the threshold behavior is not expected to change.

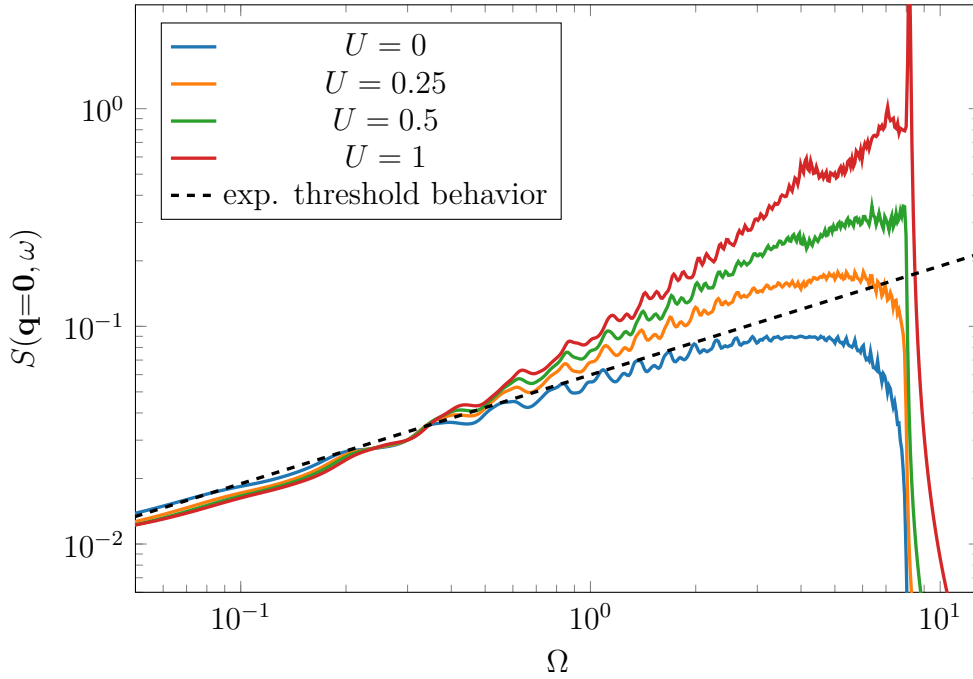


Figure 6.5.: Simulated behavior of $S(\mathbf{q}=\mathbf{0}, \omega)$ for semions with an additional interaction Ur^{-3} for $U = 0, 0.25, 0.5, 1$ on a 40×40 lattice, which is expected to agree with the non-interacting threshold behavior (dashed) in the low-energy limit.

It has to be emphasized that the above argument is by no means rigorous. Nevertheless, the change in the threshold behavior for $\epsilon = 0$ coincides with a diverging integral over $V(r)$ in (6.9) for zero energy. I.e. from this argument, a change in the threshold behavior is predicted, which agrees with what was found using the exact treatment of this case. Furthermore, it also predicts changes in the threshold behavior for $\epsilon < 0$, which also agrees with the expectations and findings to be discussed below.

It is however questionable to which extent this behavior can be observed both in experiments and simulations. If one uses (6.10) as a rough estimate on how $\bar{\psi}(r)/\psi(r)$ approaches one, it is obvious that for greater amplitudes U and smaller ϵ , $\bar{\psi}(r)/\psi(r)$ converges to one more slowly. This matches the intuitive expectation, as for stronger and slower decaying interactions, a stronger influence on the wave function at large distances is expected. Thus, for great amplitudes U and small ϵ , the region in which the threshold behavior is not affected might be too small in order to be observed.

In Fig. 6.5, the spectral function obtained from lattice simulations for semions on a 40×40 lattice is depicted for the interaction strengths $U \in \{0, 0.25, 0.5, 1\}$. By comparison with Fig. 6.3, we have to conclude that the agreement with the non-interacting threshold behavior at small energies may only be due to the utilized numerical method. Further, by trying to fit an energy dependency to the part that deviates from the expected threshold behavior in the intermediate energy range, it turns out that unlike the previous case, the behavior does not agree with some power law Ω^β for some Ω -independent parameter β . This means that using the

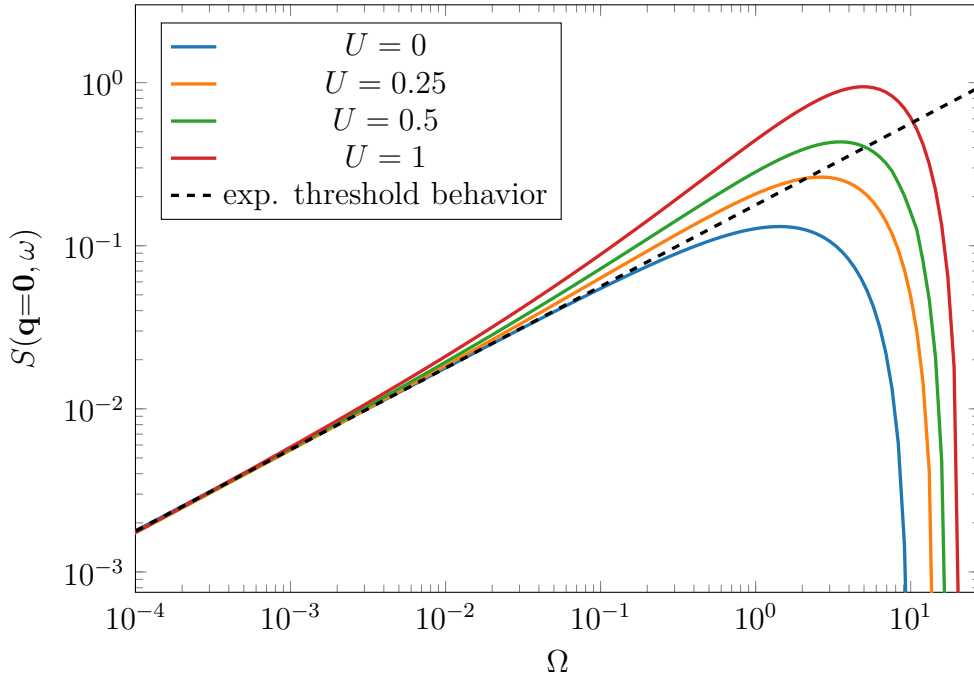


Figure 6.6.: Simulated behavior of $S(\mathbf{q}=\mathbf{0}, \omega)$ for semions with an additional interaction $U r^{-3}$ for $U = 0, 0.25, 0.5, 1$ obtained by numerically solving the Schrödinger equation, which is expected to agree with the non-interacting threshold behavior (dashed) in the low-energy limit.

lattice simulations, we are not able to determine the desired threshold behavior at low energies or infer it from the behavior at intermediate energies as above in Fig. 6.3.

The just observed behavior at these intermediate energies can be confirmed by looking at the results from the continuous simulations that are plotted in Fig. 6.6 for the same interaction strengths. More interestingly, since for the continuous simulations, the possible values of Ω are not bounded, it can be confirmed that the threshold behavior agrees with the non-interacting expectation at low energies, as predicted by the above argument. I.e., while the threshold behavior remains unaffected by interactions $\propto r^{-3}$, significant deviations are found at much smaller energies compared to interactions $\propto r^{-2}$.

In order to get a rough idea of the orders of magnitude a physical system may feature, we make a very simple estimate: Let us assume that we are dealing with particles whose properties agree with an electron's. These particles interact via magnetic dipole interactions, which have the form

$$-\frac{\mu_0}{4\pi r^3} (3(\mathbf{m}_1 \cdot \hat{\mathbf{r}})(\mathbf{m}_2 \cdot \hat{\mathbf{r}}) - \mathbf{m}_1 \cdot \mathbf{m}_2), \quad (6.11)$$

where \mathbf{m}_i denote the two dipole moments whose magnitudes equal the Bohr magneton μ_B , μ_0 the vacuum permeability and $\hat{\mathbf{r}}$ the unit vector of \mathbf{r} that connects the two particles. Putting back the respective values for m and \hbar and letting r become dimensionless by measuring it in terms of $a = 10^{-9}\text{m}$, the obtained dimensionless values in (6.8) are $U \approx \mu_0 \mu_B^2 m_e / 4\pi \hbar^2 a \approx 7 \cdot 10^{-7}$ and

$\Omega = 1\text{eV}m_e a^2/\hbar^2 \approx 13$, where we assumed that the incident beam in the scattering experiment has an energy corresponding to the creation of two particles plus 1eV.

This example shows that for magnetic dipole interactions and even for larger values of a and m , U is rather small. In the considered case, the value of Ω corresponding to an excess energy of 1eV is too large in order to measure the non-interacting behavior; 1meV would however suffice. This means that depending on the system and the properties of the excitations, it may or may not be impossible to measure the non-interacting threshold behavior. However, given the properties, one can estimate whether or not this possibility exists by computing the dimensionless values and looking at Fig. 6.6. The assumption is of course that there is no other interaction that is more dominant at large distances but the statistical interaction.

6.2.3. The Case $\epsilon < 0$

It is intuitive that for $\epsilon < 0$, changes in the threshold behavior are expected, as it was already shown above that for $\epsilon = 0$, changes occur. For interactions which decay even more slowly than this special case, a greater influence on the wave function at long distances is expected, which is supposed to affect the threshold behavior. This agrees with what is expected from Wigner's argument in 2D. For $\epsilon < 0$, the integral over $V(r)$ in (6.9) diverges at zero energy, which corresponds to the limiting case of the threshold behavior and thus, the condition for the threshold behavior to remain unaffected is not fulfilled.

The special case $\epsilon = -1$ is of particular interest as it corresponds to particles interacting via Coulomb force, which is of course highly relevant when dealing with charged particles.

Similar to the other interactions, the spectral function $S(\mathbf{q}=\mathbf{0}, \omega)$ was computed for semions on a 40×40 lattice for the interaction strengths $U = 0, 0.25, 0.5, 1$. The results are plotted in Fig. 6.7. These are, as usual, not meaningful for small Ω since their origin is the utilized numerical method rather than the system properties. The only thing that can be deduced from these graphs is that, similar to case with interactions $\propto r^{-3}$, the spectral function does not show a straight power law behavior in terms of Ω in the intermediate energy range.

This is confirmed by the results of $S(\mathbf{q}=\mathbf{0}, \omega)$ obtained from the continuous simulations, which are depicted in Fig. 6.8. Furthermore, it can be seen that the threshold behavior is drastically different from the other cases studied before. The slopes of the graphs (which correspond to the exponents of a power law in log-log-plots) are of higher magnitudes and do not seem to converge as fast. However, while the threshold behavior itself is changed, there may still be an energy range within which the spectral functions approximately behave the same as in the non-interacting case. I.e., despite the interactions, this could then in principle be used in experiments to determine the statistical nature of the particles, given such an energy range exists. Indeed, in Fig. 6.8, appropriate energy ranges can be found for all the chosen interaction strengths. The problem is however that these energy ranges are very narrow.

We thus take a closer look specifically at small values of U and directly evaluate the deviation from the expected non-interacting threshold behavior. This "local energy dependence", i.e. local power law behavior is given by $\text{dln}(S(\mathbf{q}=\mathbf{0}, \omega))/\text{dln}(\omega) - a_0$, where the non-interacting threshold behavior a_0 was already subtracted. This quantity is plotted in Fig. 6.9 for semions

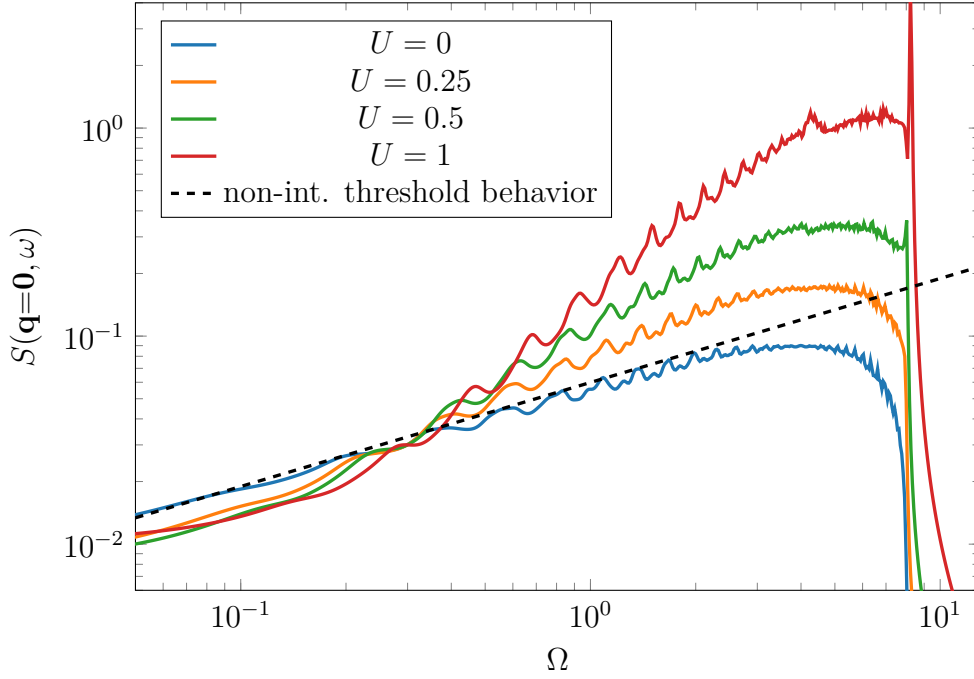


Figure 6.7.: Simulated threshold behavior of $S(\mathbf{q}=\mathbf{0}, \omega)$ for semions with an additional interaction Ur^{-1} for $U = 0, 0.25, 0.5, 1$ on a 40×40 lattice, which is expected to deviate from the non-interacting behavior (dashed) in the low-energy limit.

($a_0 = 0.5$) for $U = 0.001, 0.005, 0.01$ and was obtained from continuous simulations. It can be seen that for small enough interactions, there is indeed an extended energy range for which the non-interacting expectation is approximately recovered. Naturally, this energy range becomes larger with decreasing interaction strength but as long as $U \neq 0$, the (interacting) threshold behavior itself differs from the non-interacting one.

In order to estimate the behavior of this energy range, we note that within it, the ratio $\bar{\psi}(r)/\psi(r)$ should be approximately one. The reason for this is the same as in the 2D Wigner's argument: the behavior of the spectral function depends on the wave function, i.e. if $\bar{\psi}(r)/\psi(r) \approx 1$ over an extended range, there is a range within the non-interacting behavior may be approximately recovered. A connection between the radii r which fulfil $\bar{\psi}(r)/\psi(r) \approx 1$ and the energy range within which the desired behavior is observed can be established by looking at the solution of the Schrödinger equation (6.8) with an interaction U/r , which we try to solve using the following ansatz:

$$\psi(r, \sqrt{\Omega}) \propto e^{i\sqrt{\Omega}r} f(r, \sqrt{\Omega}). \quad (6.12)$$

The exponential was chosen in order to compensate the Ω in the Schrödinger equation. Plugging (6.12) into (6.8) yields the differential equation

$$\left(-\frac{d^2}{dr^2} - \frac{1}{r} \frac{d}{dr} + \frac{\alpha^2}{r^2} + \frac{U - i\sqrt{\Omega}}{r} \right) f(r, \sqrt{\Omega}) = 0, \quad (6.13)$$

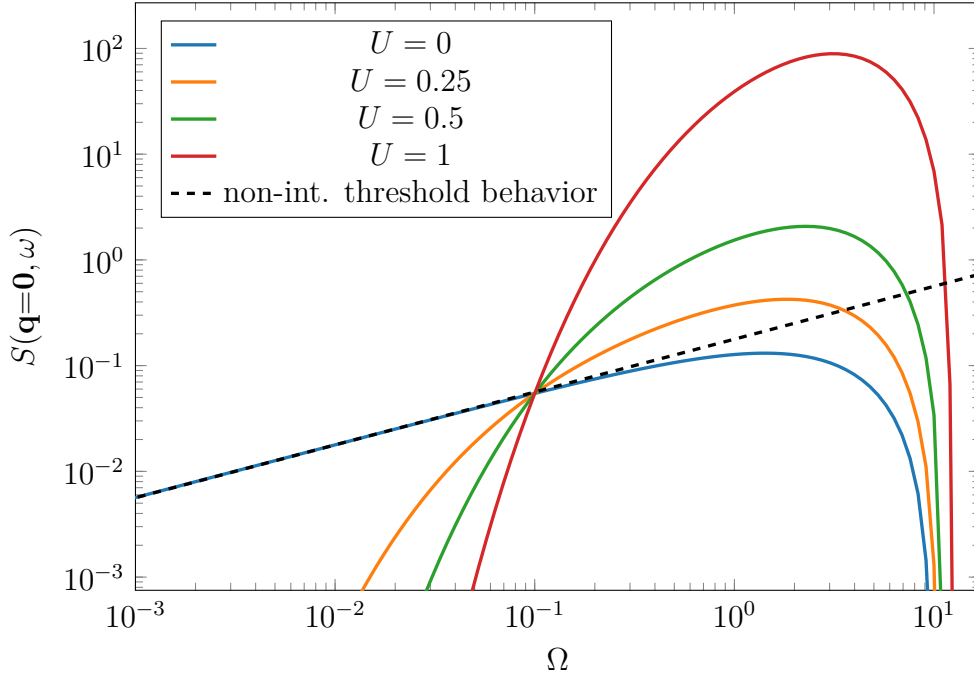


Figure 6.8.: Simulated threshold behavior of $S(\mathbf{q}=\mathbf{0}, \omega)$ for semions with an additional interaction Ur^{-1} for $U = 0, 0.25, 0.5, 1$ obtained by numerically solving the Schrödinger equation, which is expected to deviate from the non-interacting behavior (dashed) in the low-energy limit.

where we set $l = 0$. We can now simply expand $f(r, \sqrt{\Omega})$ for large r , similar to what we did in appendix D. The first two orders are given by

$$f(r, \sqrt{\Omega}) \propto \frac{1}{r^{0.5 + \frac{iU}{2\sqrt{\Omega}}}} \left(1 + i \frac{\alpha^2 - \frac{1}{4} + \frac{U^2}{4\Omega} - i \frac{U}{2\sqrt{\Omega}}}{2\sqrt{\Omega}} \frac{1}{r} + O\left(\frac{1}{r^2}\right) \right). \quad (6.14)$$

By comparing this to the non-interacting asymptotic behavior that arises from the same expansion for $U = 0$, it can be seen that the deviations are governed by the ratio $U/\sqrt{\Omega}$. I.e. the non-interacting behavior in the wave function and therefore also in the spectral function is approximately recovered for $U/\sqrt{\Omega} \ll 1$ or

$$U^2 \ll \Omega. \quad (6.15)$$

Another ansatz is to try the power series method to obtain a solution for the wave function and plug it into (6.4). Using

$$\psi(r, \sqrt{\Omega}) = \sum_{n=0}^{\infty} a_n r^{\beta+n} \quad (6.16)$$

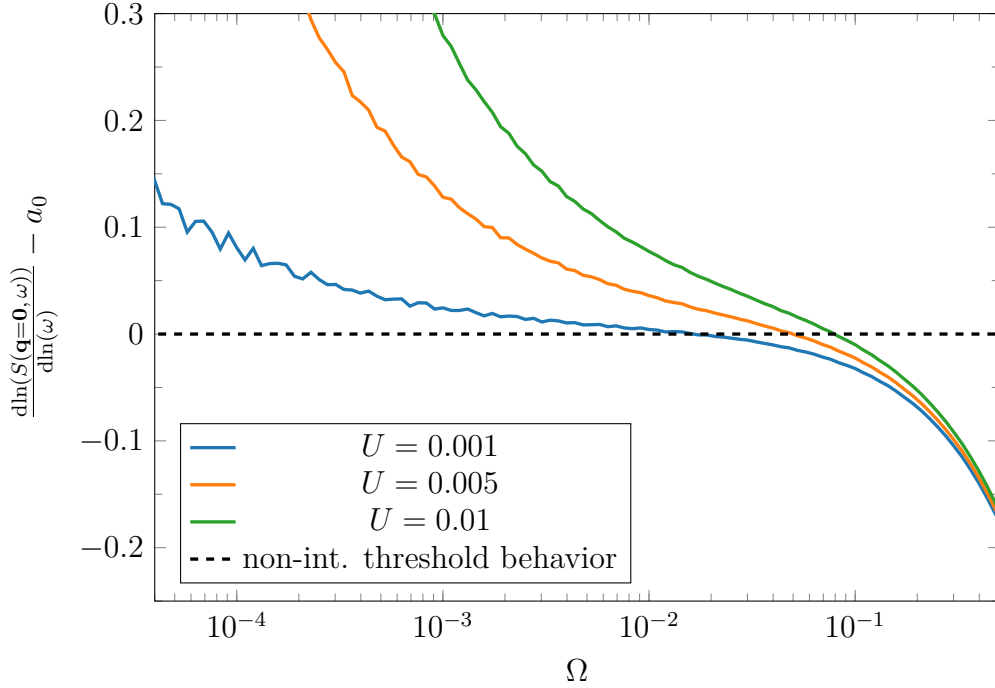


Figure 6.9.: Deviation of the local energy dependence from the non-interacting expectation a_0 (dashed), $\text{dln}(S(\mathbf{q}=\mathbf{0}, \omega))/\text{dln}(\omega) - a_0$, for semions ($a_0 = 0.5$) with interaction $U r^{-1}$, $U = 0.001, 0.005, 0.01$, obtained from numerically solving the Schrödinger equation and taking the mentioned derivative.

with some $\beta \in \mathbb{R}$ as solution to (6.8) for $l = 0$ yields

$$\sum_{n=0}^{\infty} r^{\beta+n} \left[a_n \left(-(\beta+n)^2 + \alpha^2 \right) + U a_{n-1} - \Omega a_{n-2} \right], \quad (6.17)$$

i.e.

$$\beta = \alpha, \quad a_1 = \frac{U}{1+2\alpha} a_0, \quad a_n = \frac{U}{n^2 + 2n\alpha} a_{n-1} - \frac{\Omega}{n^2 + 2n\alpha} a_{n-2}. \quad (6.18)$$

With that, we can approximate the squared absolute value of the wave function in (6.4):

$$|\psi(a, \sqrt{\Omega})|^2 \approx |a_0|^2 \left[a^{2\alpha} + \frac{2U}{1+2\alpha} a^{2\alpha+1} + \left(\frac{2U^2}{(1+2\alpha)^2} + \frac{2U^2}{(1+2\alpha)(4+4\alpha)} - \frac{2\Omega}{4+4\alpha} \right) a^{2\alpha+2} \right]. \quad (6.19)$$

In order to approximately recover the threshold behavior, the corrections in the equation above have to be small, i.e. $2U \ll 1 + 2\alpha$,

$$\Omega \ll 2 + 2\alpha \quad \text{and} \quad U \ll \Omega \quad (6.20)$$

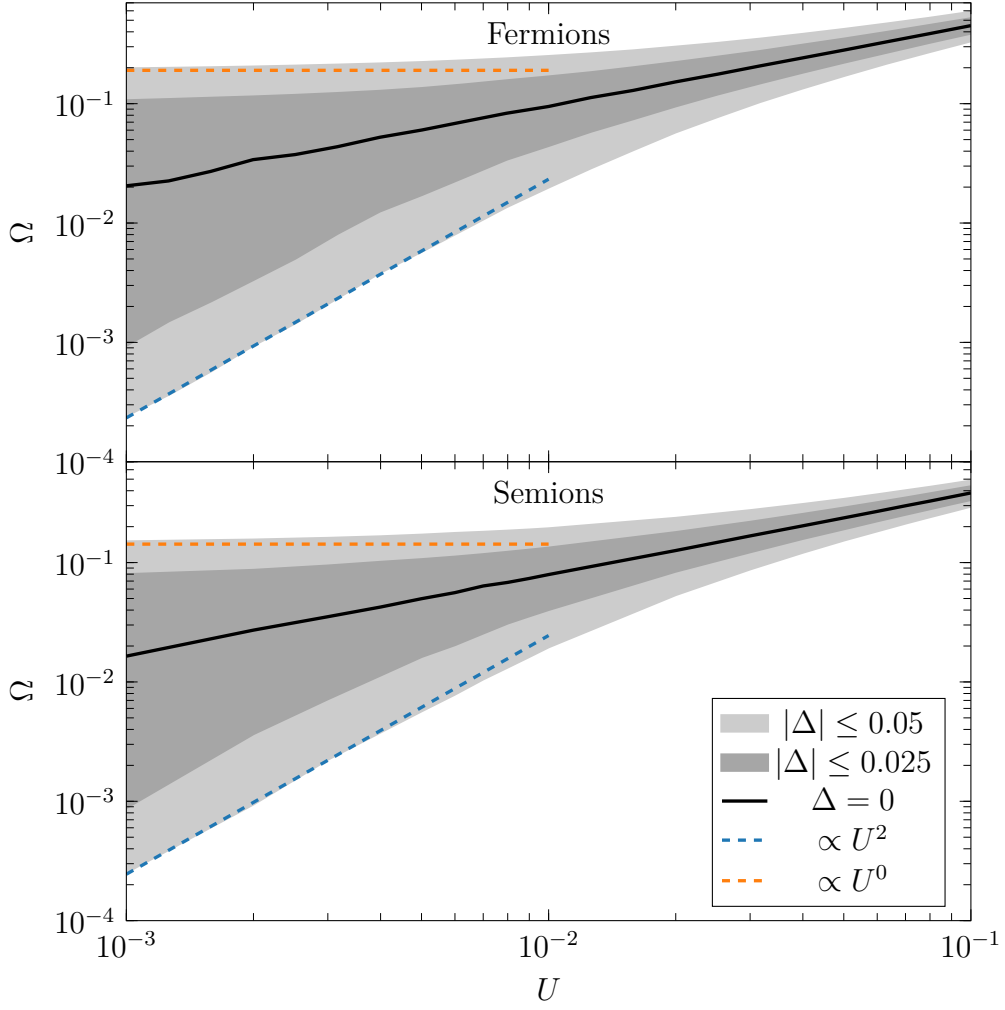


Figure 6.10.: $\frac{d\ln(S(\mathbf{q}=\mathbf{0}, \omega))}{d\ln(\omega)} - a_0 = \Delta$ for $\Delta = 0$ and $|\Delta| \leq 0.025, 0.05$ as function of U for fermions (upper plot) and semions (lower plot) interacting with Ur^{-1} , obtained from numerically solving the Schrödinger equation and analyzing the mentioned derivative.

have to hold, where the last inequality was imposed using the recursion relation in (6.18). The reason for this is that in (6.19), all higher orders should be suppressed and within each order, the dominant contribution should arise due to Ω , not U . Thus, one can simply impose that this is already taken care of in the recursion (6.18). As this is a stronger restriction on U in the relevant energy region, the above $2U \ll 1 + 2\alpha$ is not included in (6.20).

Overall, we derived two important conditions: (6.15) estimates a lower bound on the energy range in which the non-interacting threshold behavior might be recovered, whereas (6.20) does so for an upper bound. For the latter, there is an additional constraint, $U \ll \Omega$, to be fulfilled. These considerations can be verified by looking at the plots in Fig. 6.10, which show the areas in the Ω - U parameter space for which the fermionic and the semionic spectral functions behave similarly to their non-interacting threshold behavior. "Similar" behavior in this context means

that the deviation $\text{dln}(S(\mathbf{q}=\mathbf{0},\omega))/\text{dln}(\omega) - a_0$ is smaller than some threshold value Δ . In Fig. 6.10, the areas corresponding to similarities of $|\Delta| \leq 0.025, 0.05$ were plotted as well as the line $\Delta = 0$. Both for fermions and for semions, the lower bound of the $|\Delta| \leq 0.05$ region scales as $\Omega(U) \propto U^2$, as predicted by (6.15). The upper bound also follows the prediction of $\Omega \ll 2 + 2\alpha$ and becomes constant in the limit $U \rightarrow 0$, which was revealed by linear fitting. The extracted constant values Ω approaches in this limit show remarkable agreement with the derived inequality: For semions, this value is given by 0.1428(4), for fermions it is 0.1903(4). The ratio of the two values is 0.7503(21), which agrees very well with the predicted ratio of $(2 + 2 \cdot 0.5)/(2 + 2 \cdot 1) = 0.75$ within the uncertainty.

While this are already remarkable results, it is of particular interest to get an estimate for the simulation parameters corresponding to physical systems. Let us assume again that we are dealing with particles that feature the same properties as electrons. They interact with each other according to the Coulomb's law

$$\frac{q_1 q_2}{4\pi\epsilon_0 r}, \quad (6.21)$$

where q_i denote the electric charges and ϵ_0 the vacuum permittivity. As before with the magnetic dipole interactions, we put m and \hbar back into equation and measure r in terms of $a = 10^{-9}\text{m}$. With this, the obtained values are $U = e^2 m_e a / 4\pi\epsilon_0 \hbar^2 \approx 19$ and $\Omega = 1\text{eV} m_e a^2 / \hbar^2 \approx 13$. As before, we just assumed an incident beam energy corresponding to the two particles plus 1eV. From the estimated value for U , it can be seen that the desired non-interacting threshold behavior can not be measured for these particles; in order theoretically to do that, the corresponding excitations need to have fractional charges and smaller masses.

6.3. Fibonacci Anyons

Finally, we can take a look at the lattice simulation results for non-interacting Fibonacci anyons, which are plotted in Fig. 6.11 for a 40×40 lattice. Here, it is important to remember how $|\psi_i\rangle$ in (6.2) was chosen: Each sheet was given the same amplitude. Although it was verified that the results do not change qualitatively for different sheet distributions when simulating semions, they do change for Fibonacci anyons. To be more precise, the sheet distribution of $O(\mathbf{R})|\psi_i\rangle$ is (unlike for abelian anyons) not predetermined by the sheet distribution of $|\psi_i\rangle$ for non-abelian anyons, which can already be seen by the fact that the total sheet numbers do not agree for zero and two Fibonacci anyons. We thus modify the convention such that for the states $O(\mathbf{R})|\psi_i\rangle$, each sheet is given the same probability amplitude. The threshold behavior of $S(\mathbf{q}=\mathbf{0},\omega)$ turns out to be proportional $\Omega^{11/15}$ for this particular choice. This can be explained using the basic data of the Fibonacci anyon model and the knowledge regarding the wave function components (sheets), as discussed in sections 3.3 and 4.1.

For two Fibonacci anyons, there are three sheets. For two of the three sheets, the two Fibonacci anyons fuse trivially; for the other one, they fuse to another Fibonacci anyon. This means that (depending on the sheet) we can associate the phase $R_1^{\tau\tau} = e^{4\pi i/5}$ or $R_\tau^{\tau\tau} = e^{-3\pi i/5}$ to

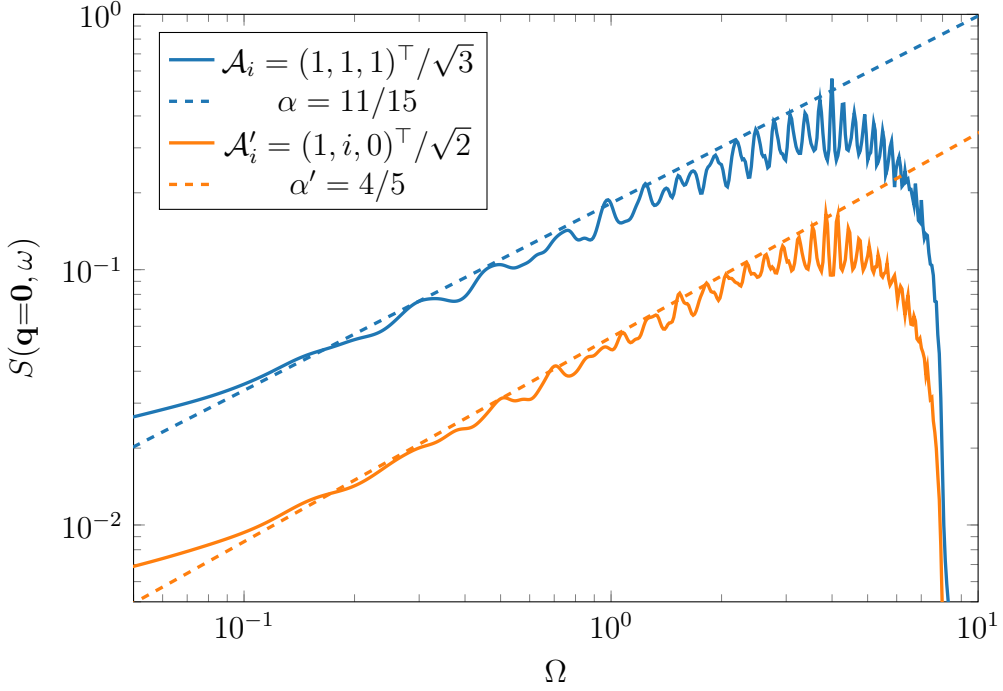


Figure 6.11.: Simulated threshold behavior of $S(\mathbf{q}=\mathbf{0}, \omega)$ for non-interacting Fibonacci anyons on a 40×40 lattice. The threshold behavior was found to agree with $\omega^{11/15}$ for the sheet distributions of $O(\mathbf{R})|\psi_i\rangle$ being $\mathcal{A}_i = (1, 1, 1)^\top / \sqrt{3}$. For $\mathcal{A}'_i = (1, i, 0)^\top / \sqrt{2}$, it agrees with $\alpha' = 4/5$.

exchanges, which corresponds to $\alpha_1 = 4/5$ or $\alpha_\tau = 3/5$ ¹, respectively. A key point here is that upon exchanging the two anyons, the sheet is not changed. We further argue that the sheet changing at the two cuts can be neglected, as in the Hamiltonian, the relative contributions due to the cuts compared to all contributions together are $\propto L_x^{-1}$ and $\propto L_y^{-1}$, i.e. they are negligible for large enough system sizes.

As the studied Hamiltonian does not favor any fusion channels, we can assume that every sheet contributes the same weight to the threshold behavior, i.e. there will be some averaging based on the sheet distribution of $O(\mathbf{R})|\psi_i\rangle$ involved. If we now completely neglect the effect of the cuts, there cannot be interference effects between different sheets, as there is no way of changing sheets left. This means that α for the system containing two Fibonacci anyons is given by averaging α_1 and α_τ according to the sheets, i.e. assuming that the sheet amplitude vector of every state $O(\mathbf{R})|\psi_i\rangle$ is given by \mathcal{A}_i with components $\mathcal{A}_{i,j}$ ($j = 1, 2, 3$), α is given by

$$\alpha = (|\mathcal{A}_{i,1}|^2 + |\mathcal{A}_{i,2}|^2) \alpha_1 + |\mathcal{A}_{i,3}|^2 \alpha_\tau \in \left[\frac{3}{5}, \frac{4}{5} \right]. \quad (6.22)$$

For the above convention, $\mathcal{A}_i = (1, 1, 1)^\top / \sqrt{3}$ and thus $\alpha = 11/15$, which agrees with the simulation results. This rule was verified for many more choices of \mathcal{A}_i . As an example, in Fig.

¹One can see that the sign disappears by looking at the differential equation corresponding to the R -move.

6.11, we also plotted the spectral function for $\mathcal{A}_i = (1, i, 0)^\top / \sqrt{2}$, which also agrees with the expectation of $\alpha' = 4/5$. We can thus see that this heuristic argument can indeed explain the threshold behavior of $S(\mathbf{q}=0, \omega)$.

In principle, one could now study the effect of interactions once more for this case. We will not do this, as the results agree with what is expected based on the previous discussions. In addition to that, we still lack a sophisticated method to continuously simulate Fibonacci anyons. Simply using the value of α according to the above heuristic argument and plugging it into (6.8) does not necessarily do justice to the anyons' non-abelian nature.

7. Conclusion

In this thesis, an important step forward in terms of simulating anyonic systems was taken. After starting with a summary of an already existing algorithm [17] that is restricted to abelian anyons and adding some new details to it (like showing that the translation operators that are essential for the construction of momentum states indeed commute), we developed a completely new, generalized algorithm that is able to simulate both abelian and non-abelian anyon models. The corresponding Hamiltonian solely accounts for the anyons' mutual and exchange statistics and is thus perfectly suitable for studying dynamics of free anyons. One of the biggest advantages of this algorithm apart from the fact that it can simulate any anyon model is that due to it being based on fusion diagrams, it is quite intuitive where all the operations / contributions come from. It further allows for a way to fix the external fluxes without having to impose an arbitrary convention; in the generalized algorithm, the flux convention naturally arises due to the diagrams. Finally, in order to make even better use of the algorithm in e.g. exact diagonalization methods, we showed that the Hamiltonian commutes with the two translation operators and constructed the appropriate momentum states.

Moreover, we briefly discussed how to efficiently compute long-range interactions on periodic lattices that are to be added later on to the generalized algorithm. In order to complement the lattice simulations, the continuous Hamiltonian of a two-anyon system was introduced, which corresponds to the continuous version of the generalized algorithm for two abelian anyons with interactions.

Using the generalized algorithm without interactions, we could already show a few interesting results: It was found that for semions and Fibonacci anyons, the energy level spacing statistics in the $k_x = k_y = 1$ sector agrees with a Wigner-Dyson distribution, implying that all symmetries were already exploited by using momentum states. Further, for a quench in which four anyons localized in the center of a ladder were studied, it turned out that the time-dependent density distributions become homogeneous and converge to their time average / ensemble predictions. This together with the level spacing statistics hints at thermalizing behavior of anyonic systems that are merely subject to their own statistics.

Finally, the threshold behavior of the spectral function was studied mainly for semions using both lattice simulations and continuous simulations, where our primary focus was on the effect of long-range interactions. Using the same approach in 2D as Wigner in 3D [43], it could be argued that for interactions of the form $Ur^{-(2+\epsilon)}$, $\epsilon > 0$, the threshold behavior is not affected. This was also verified by the continuous simulations. For the critical value of $\epsilon = 0$, the corresponding differential equations can be analytically solved, predicting a change in the threshold behavior that could be confirmed with both lattice and continuous simulations. For $\epsilon < 0$, the threshold behavior is also affected. Focussing on the case $\epsilon = -1$, we found energy

ranges beyond the threshold behavior within which the non-interacting threshold behavior is approximately recovered. Using expansions of the wave function, we could derive two inequalities that determine the upper and lower bounds of these energy ranges at low interaction strengths. In the last part, we studied the results for the spectral function's threshold behavior for Fibonacci anyons (without interactions), for which we had no predictions. It turned out that due to the non-abelian nature, the superposition of wave function components in the two-anyon system is key to understand the threshold behavior, as it can be determined by weighting the components according to their probability.

As this effectively corresponds to weighting different *abelian* anyon models, it would be very interesting to study the threshold behavior of the spectral functions for three Fibonacci anyons in the future. The reason for this is that the argument that was used for two anyons does not work for three anyons and thus, studying this case might provide more insights into non-abelian anyons and their nature.

In addition to that, there are many more questions to be answered and simulations to be performed using our more sophisticated and generalized algorithm. Straight forward applications would be to take our algorithm, add some interactions and study the properties of interest. As an example, interactions favoring different fusion channels like in the golden chain [7, 10] for Fibonacci anyons could be imposed. Adding such interactions to the statistical Hamiltonian is especially interesting for non-abelian anyons, as (intermediate) fusion products may already change upon exchanging two anyons (whereas for abelian anyons, one of the two cuts needs to be crossed). Depending on the interaction strength, this may have tremendous effects on the dynamics.

For quasi one-dimensional systems, it could also be beneficial to translate the algorithm to matrix product states in order to study larger anyonic systems, similar to [19, 47]. In the end however, it should be noted that due to the construction of the momentum states, the new algorithm may be very well used to perform exact diagonalization tasks. After all, we even showed that there is only the spacial symmetries left to take advantage of, i.e. the algorithm is (with the exception of a few momentum sectors) already optimized when it comes to block diagonalization.

A. Momentum States for the Generalized Algorithm

Due to the periodicity in x - and y -direction, it is possible to construct momentum states which block diagonalize the Hamiltonian \mathcal{H} that is given by (4.1). In order to do this, one has to look at the action of the two operators T_x and T_y that translate all anyons in positive x - and y -direction, respectively.

A.1. Momentum States in x -Direction

Applying T_x onto an arbitrary state $|\{\mathbf{r}_k\}, \{\alpha_k\}; \mathcal{A}\rangle$ does in general not only shift the anyons' positions in positive x -direction, but does also change the sheet amplitude vector \mathcal{A} . From the braid rules discussed in the previous section, it is clear that braiding can only occur if anyons are translated over cut B since T_x translates all anyons simultaneously. If only one anyon is translated across cut B upon applying T_x , we already know that the sheet amplitude vector is simply multiplied by the sheet hopping matrix $T_x^s(\{\alpha_k\})$ with entries given by (4.9) or (4.10). If multiple anyons are simultaneously translated over cut B , the resulting sheet amplitude vector can be expressed in terms of a product of multiple sheet hopping matrices being multiplied onto \mathcal{A} . The reason for this can be seen when dragging multiple anyons around the non-contractible loop in a fusion diagram and keeping in mind that the lines associated to the anyons are not allowed to further braid with each other. Then, successively applying $T_x^s(\{\alpha_k\})$ on \mathcal{A} with the proper order of anyon charges in the arguments takes care of the loops one after another, starting from the most inner one. In fact, such a fusion diagram is also obtained if T_x is applied multiple times onto a state, where for each application no more than a single anyon crosses cut B . With this, it is also clear that such diagrams with multiple anyons being dragged around the non-contractible loop can be brought back to the conventional form by only using sheet hopping matrices. Thus, the application of T_x onto an arbitrary state can be written as

$$T_x|\{\mathbf{r}_k\}, \{\alpha_k\}; \mathcal{A}\rangle = |\{\mathbf{r}_k + \mathbf{e}_x\}, \{\alpha_k\}; \prod_{i=0}^{j-1} T_x^s(\sigma^i(\{\alpha_k\}))\mathcal{A}\rangle. \quad (\text{A.1})$$

Here, \mathbf{e}_x denotes the vector pointing in positive x -direction whose length equals one lattice spacing and $\mathbf{r}_k + \mathbf{e}_x$ is understood modulo the lattice size due to the PBC. The product $\prod_{i=0}^{j-1} T_x^s(\sigma^i(\{\alpha_k\})) = T_x^s(\sigma^{j-1}(\{\alpha_k\})) T_x^s(\sigma^{j-2}(\{\alpha_k\})) \dots T_x^s(\{\alpha_k\})$ is ordered, $\sigma(1, 2, \dots, N) = (N, 1, 2, \dots, N-1)$ and j is the number of anyons being translated over cut B when applying T_x . We will from now on use the shorthand notation $\{\alpha_k\}^i \equiv \sigma^i(\{\alpha_k\})$. Note that it is not necessary

to apply σ on the arguments $\{\mathbf{r}_k + \mathbf{e}_x\}$ and $\{\alpha_k\}$ in (A.1) since applying any permutation operator on both $\{\mathbf{r}_k + \mathbf{e}_x\}$ and $\{\alpha_k\}$ does not change the anyon configuration.

From the above equation and (4.11), it can be seen that $T_x^{L_x} = \mathbb{1}$, i.e., both the final anyon configuration and the final sheet amplitude vector after applying $T_x^{L_x}$ agree with the ones of the initial state. This is fairly obvious for the anyon configuration due to the PBC. That this also holds for the sheet amplitude vectors can be seen when looking at an arbitrary fusion diagram: Applying $T_x^{L_x}$ is in terms of the diagrams equivalent to dragging all N anyons around the non-contractible loop without any further braiding between the lines. As this is done with all anyons, the diagram is in fact equivalent to the initial one. It should be kept in mind that $T_x^{L_x} = \mathbb{1}$ is only true in the physical sectors of the operator, i.e. for the entries corresponding to the sheets that are accessible with a given anyon configuration. If there are sheets on which this given anyon configuration is not allowed to exist, the corresponding diagonal entries (eigenvalues) in $T_x^{L_x}$ are zero.

This has important consequences: If an anyon configuration on the lattice possesses a periodicity p_x with $0 < p_x < L_x$ such that applying $T_x^{p_x}$ onto the state yields the same anyon configuration again (where one also has to consider the anyonic charges, not only the positions), the sheet hopping matrices associated to these configurations have an additional property. Suppose that by applying $T_x^{p_x}$, $n_x = Np_x/L_x$ anyons are in total translated over cut B . Then, it follows from (4.11) that

$$\left[\prod_{i=0}^{n_x-1} T_x^s(\{\alpha_k\}^i) \right]^{L_x/p_x} = \mathbb{1}, \quad (\text{A.2})$$

i.e., $\prod_{i=0}^{n_x-1} T_x^s(\{\alpha_k\}^i)$ is diagonalizable with eigenvalues $e^{2\pi i j p_x / L_x}$, $j \in \{0, 1, \dots, L_x/p_x - 1\}$. In particular, if there are N identical anyons on the lattice, the sheet hopping matrix (there exists only one sheet hopping matrix in this case as each possible charge configuration $\{\alpha_k\}$ is the same) is diagonalizable with eigenvalues $e^{2\pi i j / N}$, $j \in \{0, 1, \dots, N - 1\}$.

This property is of great importance when constructing momentum states that exploit the translational invariance in x -direction. These states are given by

$$\begin{aligned} |\{\mathbf{r}_k\}, \{\alpha_k\}; k_x; \mathcal{A}\rangle &\equiv \frac{1}{\sqrt{N_x}} \sum_{j=0}^{L_x-1} e^{ij k_x} T_x^j |\{\mathbf{r}_k\}, \{\alpha_k\}; \mathcal{A}\rangle \\ &= \frac{1}{\sqrt{N_x}} \sum_{j=0}^{L_x-1} e^{ij k_x} |\{\mathbf{r}_k + j\mathbf{e}_x\}, \{\alpha_k\}; \prod_{i=0}^{n_x(j)-1} T_x^s(\{\alpha_k\}^i) \mathcal{A}\rangle, \end{aligned} \quad (\text{A.3})$$

where $n_x(j)$ denotes the number of anyons being translated over cut B when applying T_x^j onto $|\{\mathbf{r}_k\}, \{\alpha_k\}; \mathcal{A}\rangle$, $N_x = L_x^2/p_x$ the normalization constant and k_x the momentum in x -direction with $k_x \in \{0, 2\pi/L_x, \dots, 2\pi(L_x-1)/L_x\}$ if $p_x = L_x$. $|\{\mathbf{r}_k\}, \{\alpha_k\}; \mathcal{A}\rangle$ will be referred to as "reference state" of $|\{\mathbf{r}_k\}, \{\alpha_k\}; k_x; \mathcal{A}\rangle$, as it is the state generating the momentum state by being translated. From the definition in (A.3), it can be seen that

$$T_x |\{\mathbf{r}_k\}, \{\alpha_k\}; k_x; \mathcal{A}\rangle = e^{-ik_x} |\{\mathbf{r}_k\}, \{\alpha_k\}; k_x; \mathcal{A}\rangle, \quad (\text{A.4})$$

as expected for a momentum state with momentum k_x .

If the anyon configuration of $|\{\mathbf{r}_k\}, \{\alpha_k\}; \mathcal{A}\rangle$ in (A.3) is periodic in x -direction with a periodicity $p_x < L_x$, there is a constraint for the allowed momenta k_x . By choosing \mathcal{A} to be an eigenvector of $\prod_{i=0}^{n_x(p_x)-1} T_x^s(\{\alpha_k\}^i)$,

$$e^{ip_x k_x} e^{2\pi i \beta p_x / L_x} = 1 \quad \text{for} \quad \prod_{i=0}^{n_x(p_x)-1} T_x^s(\{\alpha_k\}^i) \mathcal{A} = e^{2\pi i \beta p_x / L_x} \mathcal{A} \quad (\text{A.5})$$

has to be fulfilled, restricting the allowed momenta to $2\pi n/p_x - 2\pi\beta/L_x$, $n \in \{0, 1, \dots, p_x - 1\}$ for periodic configurations. This simply assures that applying $T_x^{p_x}$ onto the reference state yields the same state again, including the sheet amplitude vector, i.e. $T_x^{p_x} |\{\mathbf{r}_k\}, \{\alpha_k\}; \mathcal{A}\rangle = |\{\mathbf{r}_k\}, \{\alpha_k\}; \mathcal{A}\rangle$. Thus, when constructing the momentum states, one first has to find the periodicity p_x of each anyon configuration. Then, if $p_x < L_x$, eigenstates of $\prod_{i=0}^{n_x(p_x)-1} T_x^s(\{\alpha_k\}^i)$ have to be used as sheet amplitude vectors. The momentum sectors in which such a state may exist are obtained by checking condition (A.5). If there are multiple eigenstates \mathcal{A} to the same eigenvalue, it is to be assured that these are pairwise orthonormal.

It remains to show that the states $|\{\mathbf{r}_k\}, \{\alpha_k\}; k_x; \mathcal{A}\rangle$ indeed form a basis of the Hilbert space, i.e., that different momentum states are orthogonal and that the number of momentum states equals the number of states in the original basis (4.2). It is obvious that two momentum states with unrelated reference states, meaning that the anyon configuration of one reference state can not be brought to the form of the anyon configuration of the other one using T_x -operators, are orthogonal. We can thus restrict ourselves to momentum states with related reference states and for these, we assume that the reference states possess identical anyon configurations. This does not further restrict the number of momentum states to be considered, as a momentum state generated by a translated version of a reference state differs from the original one merely by a phase. The overlap between two momentum states whose reference states have identical anyon configurations is given by

$$\begin{aligned} & \langle \{\mathbf{r}_k\}, \{\alpha_k\}; k'_x; \mathcal{A}' | \{\mathbf{r}_k\}, \{\alpha_k\}; k_x; \mathcal{A} \rangle \\ &= \frac{1}{N_x} \sum_{j, j'=0}^{L_x-1} e^{i(jk_x - j'k'_x)} \langle \{\mathbf{r}_k\}, \{\alpha_k\}; \mathcal{A}' | T_x^{j-j'} | \{\mathbf{r}_k\}, \{\alpha_k\}; \mathcal{A} \rangle \\ &= \frac{1}{N_x} \sum_{j, j'=0}^{p_x-1} \sum_{l, l'=0}^{L_x/p_x-1} e^{i(jk_x - j'k'_x)} \langle \{\mathbf{r}_k\}, \{\alpha_k\}; \mathcal{A}' | T_x^{j-j'} | \{\mathbf{r}_k\}, \{\alpha_k\}; \mathcal{A} \rangle = \frac{L_x/p_x}{N_x} \delta_{k_x k'_x} \langle \mathcal{A}' | \mathcal{A} \rangle. \end{aligned} \quad (\text{A.6})$$

First, each sum ranging from 0 to $L_x - 1$ appearing in the momentum states can be divided into two sums, where the limits of the first one are 0 and $p_x - 1$ and the limits of the second one 0 and $L_x/p_x - 1$; both momentum states have the same periodicity due to the above restriction. This can be done since according to (A.5), acting with $T_x^{p_x}$ on one of the two reference states and multiplying with $e^{ip_x k_x} (e^{ip_x k'_x})$ does not affect the state. Then, by using that the overlap of the anyon configurations yields $\delta_{jj'}$, the sum over j gives $p_x \delta_{k_x k'_x}$. The latter holds because the allowed momenta for a momentum state with periodicity p_x are $2\pi n/p_x - 2\pi\beta/L_x$, $n \in \{0, 1, \dots, p_x - 1\}$. The relevant part in the sum is thus $\sum_{j=0}^{p_x-1} \exp\{2\pi i(n - n')j/p_x\} = p_x \delta_{n, n'} = p_x \delta_{k_x k'_x}$, where it

was already used that the eigenvalue of $\prod_{i=0}^{n_x-1} T_x^s(\{\alpha_k\}^i)$ for both of the two reference states is identical due to the overlap $\langle \mathcal{A}' | \mathcal{A} \rangle$. One finally arrives at the last expression in (A.6), which states that both the momentum and the sheet amplitude vector have to be identical for a non-zero overlap. As we already argued that the anyon configuration also has to match, it follows that the momentum states are pairwise orthogonal. This calculation also shows that $N_x = L_x^2/p_x$. There is a straight forward argument that the total number of momentum states $|\{\mathbf{r}_k\}, \{\alpha_k\}; k_x; \mathcal{A}\rangle$ is the same as the total number of states $|\{\mathbf{r}_k\}, \{\alpha_k\}; \mathcal{A}\rangle$ in the original basis (4.2): Every given anyon configuration possesses a periodicity $p_x \leq L_x$. By using a certain configuration as reference state, one can generate p_x different momentum states. At the same time, for the original basis, there are also exactly p_x states that have this very anyon configuration with the only difference being that each anyon is translated in x -direction. Taking the sheet amplitude vectors into account yields a similar result. Due to the fact that $\prod_{i=0}^{n_x(p_x)-1} T_x^s(\{\alpha_k\}^i)$ is diagonalizable, the number of eigenvectors coincides with the number of distinct sheet amplitude vectors of the original basis and thus it follows that the number of momentum states equals the number of states in the original basis.

In the last argument regarding the sheet amplitude vectors, one may need to be more precise: Only the eigenvectors of $\prod_{i=0}^{n_x(p_x)-1} T_x^s(\{\alpha_k\}^i)$ in the physical subspace, i.e., to the non-zeros eigenvalues are to be considered for the momentum states as the other eigenvectors correspond to unphysical combinations of anyon configurations and sheets. The number of relevant eigenvectors is identical for all possible choices of reference states, which can be seen from the fact that the sheet hopping matrices in (4.9) and (4.10) are unitary due to the unitarity of the F -moves. This implies that the number of accessible sheets does not change upon translating an anyon across one of the cuts. This also means that the number of accessible sheets in the original basis is the same for the given anyon configuration and its translations in x -direction, i.e. as above, the number of states in the original basis coincides with the number of momentum states and therefore, the states $|\{\mathbf{r}_k\}, \{\alpha_k\}; k_x; \mathcal{A}\rangle$ indeed form a basis of the Hilbert space.

Although we now know how to construct a momentum state basis, it is still to be shown that these states indeed block diagonalize the Hamiltonian \mathcal{H} , i.e., $[\mathcal{H}, T_x] = 0$ is to be proven. In order to argue that this is the case, we first note that the translation operator T_x can be thought of as applying the part of the Hamiltonian \mathcal{H} that translates anyons in positive x -direction at each site on which an anyon is located in arbitrary order. This point of view is straight forward to verify using the rules in Figs. 4.3 and 4.4. Due to the fact that *all* anyons are translated, there is no braiding between different anyons involved; they can at most be dragged around the non-contractible loop. This view on T_x is valid for every anyon configuration as even if the application of the relevant part of \mathcal{H} at a certain site may cause problems due to an already occupied site to its right, one can simply map the anyon configuration on a larger lattice such that blocking is avoided (as this can not happen when simultaneously translating all anyons, which is the definition of T_x) and the resulting diagram is unaffected. Such a mapped anyon configuration is for example obtained from the initial one by inserting columns of empty sites in between each pair of consecutive columns.

From this consideration, it is clear that T_x commutes with the part of \mathcal{H} that translates anyons in x -direction. Further, the translation of anyons in y -direction without crossing cut A is trivial

in the fusion diagrams and thus also commutes with T_x . In order to better understand the final case in which one anyon crosses cut A and possibly multiple others (the just mentioned anyon may or may not be included) cross cut B , we once more take a look at the illustration of a torus with punctures in Fig. 3.1. With the picture in mind that upon crossing cut B , the corresponding anyons (which come last in fusion order) are dragged around a cycle in x -direction and upon crossing cut A , the corresponding anyon is dragged around in y -direction, it becomes apparent why these two operations commute: The final state, no matter whether or not one starts with the x - or y -translations, looks always the same due to the fact that the x -translations do not introduce any braids among the punctures. This results in the y -translation always having the identical impact, independent of whether or not T_x is applied first or if the corresponding anyon is translated across both cuts or only cut A . It thus follows that $[\mathcal{H}, T_x] = 0$.

A.2. Momentum States in x - and y -Direction

It is possible to further block diagonalize the Hamiltonian by also exploiting the translation invariance in y -direction. Applying the translation operator in y -direction T_y onto $|\{\mathbf{r}_k\}, \{\alpha_k\}; \mathcal{A}\rangle$ shifts the positions of all anyons by one lattice spacing in positive y -direction and entails braiding in the fusion diagrams if an anyon is to cross cut A in the process. This braiding occurs as described in Fig. 4.5 in the previous section. If multiple anyons are simultaneously translated across cut A , this rule is applied for each of those anyons, where it is *not* important to apply the rule to the relevant anyons in a specific order, as can be seen from the following argument. Suppose that two anyons are simultaneously translated over cut A . If we begin by translating the "left" anyon (which comes first according to the fusion order), its line is dragged once around the diagram, moving behind the line of the second anyon (the braids with all other anyons are irrelevant for this argument). Then, rule in Fig. 4.5 is applied to the second anyon. Its line is also dragged around the diagram, braiding with the line of the left anyon by moving in front of it to its designated spot after going around the non-contractible loop. The lines of the two relevant anyons are actually not braided, as the line of one anyon is always in front of / behind the line of other one. These line crossings in the diagram can thus simply be resolved, which also leads to the inner line of the two lines being dragged around the non-contractible loop becoming the outer line and vice versa (see (A.7) below for a diagrammatic illustration).

If however the second anyon is translated first in the diagram, it is dragged around the non-contractible loop and moves in front of the left anyon to its final position. Then, when moving the line of the left anyon according to Fig. 4.5, it moves behind the line of the second anyon from the step before, then around the non-contractible loop to its designated spot. Overall, there is again no braiding between both of the anyons as again, the corresponding lines are always in front of / behind the other one. By resolving these line crossings, it can be seen that the final diagram is indeed equal to the one obtained when reversing the order in which the rule from Fig. 4.5 is applied, as in the first scenario.

These two scenarios look as follows in the fusion diagrams

(A.7)

where only the two anyons being translated over cut A are depicted because all other anyons merely contribute to more complex diagrams while it is clear that changing the order in which the two anyons are translated across cut A does not affect the braiding with these omitted anyons. The left-hand side in (A.7) corresponds to the first scenario described above, the right-hand side to the second one.

With this argument, it becomes clear that anyons crossing cut A do not braid with each other, which is intuitively expected when translating them simultaneously. On the other hand, these anyons do braid with all other anyons, which is neither avoidable nor unexpected, given rule (4.5).

Furthermore, the same result is obtained if two anyons are translated over cut A one after another, i.e., T_y is applied multiple times and each time no more than a single anyon crosses cut A . This also implies that applying $T_y^{L_y}$ drags all anyons once around the non-contractible loop, but does not braid them with each other, as the above argument can be employed for each anyon pair in this scenario. The resulting diagram is thus equal to the one before the application of $T_y^{L_y}$, meaning that $T_y^{L_y} = \mathbb{1}$ both in real space and in sheet space.

In principle, one could now write the action of T_y onto an arbitrary state similar to (A.1) in terms of B - and B' -operators, the punctured torus S -matrix and the sheet hopping matrices T_x^s . We will forgo this since it would not add any benefits as the operator string is already evident from (4.5); it would be necessary to introduce many new auxiliary quantities in order to obtain a general, bloated expression that would have to be absorbed into another quantity anyways in order to maintain readable expressions. We will thus simply write

$$T_y |\{\mathbf{r}_k\}, \{\alpha_k\}; \mathcal{A}\rangle = |\{\mathbf{r}_k + \mathbf{e}_y\}, \{\alpha_k\}; T_y^s \mathcal{A}\rangle, \quad (\text{A.8})$$

where \mathbf{e}_y is the vector pointing in positive y -direction possessing a length equal to one lattice spacing and $\mathbf{r}_k + \mathbf{e}_y$ is again understood modulo the lattice size. T_y^s applies rule (4.5) onto \mathcal{A} for each anyon that is translated across cut A when applying T_y , generalizing to $(T_y^s)^i$ when applying T_y^i .

From the description above, it is clear that similar to T_x , T_y can be thought of as applying the part of the Hamiltonian \mathcal{H} that translates anyons in positive y -direction at each occupied site in an arbitrary order. This time however, in the diagrams, braiding between anyons that

cross cut A and anyons that do not cross cut A is involved. Again, in order for the equivalence between T_y and the relevant parts of \mathcal{H} to hold for every state, one might need to map an anyon configuration to a larger lattice such that blocking by other anyons is avoided (the resulting diagram also needs to agree with the one expected from the initial configuration). Such a mapped anyon configuration is e.g. obtained from the initial one by inserting rows of empty sites in between each pair of consecutive rows. From this point of view, it is obvious that T_y commutes with the part in \mathcal{H} that translates anyons in y -direction. By looking at anyon configurations like the one in Fig. 4.5, their corresponding diagrams and the action of the respective operators on them, it can be verified that T_y also commutes with the part in \mathcal{H} that translates anyons in x -direction without crossing cut B . The reason for this is that the order of the braids can be exchanged in each diagram. The commutation can also be seen when looking at Fig. 3.1, where we should think of the punctures as having different y -coordinates in order to allow for braiding when translating an anyon in x -direction. Due to the fact that all the anyons crossing cut A upon acting with T_y on the state possess the largest (smallest) y -coordinates possible before (after) the translation, it can be seen that the final configuration of punctures after the application of both operators is the same for the two operator orderings. This is also true if the anyon to be translated in x -direction is located such that its initial or final position is in the same column as an anyon that is to cross cut A or if it itself is to be translated over cut A . With this very argument, it is also apparent that T_y has to commute with the part in the Hamiltonian that translates anyons in x -direction across cut B . Overall, it thus follows that $[\mathcal{H}, T_y] = 0$.

As we already argued that both T_x and T_y commute with the parts in \mathcal{H} that translate anyons along the different directions and can be viewed as these very parts acting on all the anyons, it is immediately clear that $[T_x, T_y]$ holds. Together with the other commutation relations, it follows that \mathcal{H} can be block diagonalized using simultaneous eigenstates of T_x and T_y , which will be constructed in the following.

Similar to the translation in x -direction, an anyon configuration might be periodic in y -direction with a periodicity p_y that is smaller than the lattice size, $0 < p_y < L_y$. In this case,

$$\left[(T_y^s)^{p_y} \right]^{L_y/p_y} = \mathbb{1} \quad (\text{A.9})$$

holds and $(T_y^s)^{p_y}$ is diagonalizable with eigenvalues $e^{2\pi i j p_y / L_y}$, $j \in \{0, 1, \dots, L_y/p_y - 1\}$.

Finally, one can introduce the "mixed" periodicity $\mathbf{p}_{xy} \equiv (p'_x, p'_y)$ involving translations both in x - and y -direction, given by

$$(p'_x, p'_y) \equiv \min_i \left(\min_j \left(\{ (i, j) : T_y^j T_x^i | \{\mathbf{r}_k\}, \{\alpha_k\} \rangle = | \{\mathbf{r}_k\}, \{\alpha_k\} \rangle; 0 < i \leq L_x, 0 < j \leq L_y \} \right) \right), \quad (\text{A.10})$$

where $p'_y \leq p_y$ holds. By using $[T_x, T_y] = 0$, it is evident that

$$\left[(T_y^s)^{p'_y} \prod_{i=0}^{n_x(p'_x)-1} T_x^s(\{\alpha_k\}^i) \right]^\gamma = \mathbb{1}, \quad (\text{A.11})$$

where γ is the least common multiple of L_y/p'_y and L_x/p'_x . As in the above case, it follows that $(T_y^s)^{p'_y} \prod_{i=0}^{n_x(p'_x)-1} T_x^s(\{\alpha_k\}^i)$ is diagonalizable with eigenvalues $e^{2\pi i j/\gamma}$, $j \in \{0, 1, \dots, \gamma - 1\}$.

With this knowledge, we can construct momentum states possessing the momentum k_x in x -direction and k_y in y -direction:

$$\begin{aligned} |\{\mathbf{r}_k\}, \{\alpha_k\}; \mathbf{k}; \mathcal{A}\rangle &\equiv \frac{1}{\sqrt{N_{xy}}} \sum_{j=0}^{L_x-1} \sum_{l=0}^{L_y-1} e^{ij k_x + il k_y} T_y^l T_x^j |\{\mathbf{r}_k\}, \{\alpha_k\}; \mathcal{A}\rangle \\ &= \frac{1}{\sqrt{N_{xy}}} \sum_{j=0}^{L_x-1} \sum_{l=0}^{L_y-1} e^{ij k_x + il k_y} |\{\mathbf{r}_k + j\mathbf{e}_x + l\mathbf{e}_y\}, \{\alpha_k\}; (T_y^s)^l \prod_{i=0}^{n_x(j)-1} T_x^s(\{\alpha_k\}^i) \mathcal{A}\rangle, \end{aligned} \quad (\text{A.12})$$

where $\mathbf{k} = (k_x, k_y)^\top$ denotes the momentum vector and $N_{xy} = L_x^2 L_y^2 / p_x p'_y$ the normalization constant. When there are no additional constraints due to the periodicities p_x , p_y , p'_x and p'_y , the allowed momenta are given by $k_{x(y)} \in \{0, 2\pi/L_{x(y)}, \dots, 2\pi(L_{x(y)} - 1)/L_{x(y)}\}$. Similar to the previous momentum states $|\{\mathbf{r}_k\}, \{\alpha_k\}; k_x; \mathcal{A}\rangle$, for $|\{\mathbf{r}_k\}, \{\alpha_k\}; \mathbf{k}; \mathcal{A}\rangle$

$$T_{x(y)} |\{\mathbf{r}_k\}, \{\alpha_k\}; \mathbf{k}; \mathcal{A}\rangle = e^{-ik_{x(y)}} |\{\mathbf{r}_k\}, \{\alpha_k\}; \mathbf{k}; \mathcal{A}\rangle \quad (\text{A.13})$$

holds. If one is to construct a momentum state for a reference state $|\{\mathbf{r}_k\}, \{\alpha_k\}; \mathcal{A}\rangle$ with non-trivial periodicities, there are multiple things to consider.

First of all, if $p_x < L_x$, the same constraint as for the previous momentum states has to be fulfilled: \mathcal{A} has to be chosen to be an eigenvector of $\prod_{i=0}^{n_x(p_x)-1} T_x^s(\{\alpha_k\}^i)$ and (A.5) has to be fulfilled, restricting the allowed momenta in x -direction to $2\pi n/p_x - 2\pi\beta/L_x$, $n \in \{0, 1, \dots, p_x - 1\}$. If $p_y < L_y$, \mathcal{A} has to be chosen to be an eigenvector of $(T_y^s)^{p_y}$ that fulfills

$$e^{ip_y k_y} e^{2\pi i \beta' p_y / L_y} = 1 \quad \text{for} \quad (T_y^s)^{p_y} \mathcal{A} = e^{2\pi i \beta' p_y / L_y} \mathcal{A}, \quad (\text{A.14})$$

which restricts the allowed momenta in y -direction to $2\pi n/p_y - 2\pi\beta'/L_y$, $n \in \{0, 1, \dots, p_y - 1\}$. Finally, if $p'_y < p_y$, one has to choose \mathcal{A} to be an eigenvector of $(T_y^s)^{p'_y} \prod_{i=0}^{n_x(p'_x)-1} T_x^s(\{\alpha_k\}^i)$ that fulfills

$$e^{ip'_x k_x + ip'_y k_y} e^{2\pi i \beta''} = 1 \quad \text{for} \quad (T_y^s)^{p'_y} \prod_{i=0}^{n_x(p'_x)-1} T_x^s(\{\alpha_k\}^i) \mathcal{A} = e^{2\pi i \beta''} \mathcal{A}. \quad (\text{A.15})$$

This restricts the allowed momenta to $k_x = 2\pi n/p'_x - 2\pi\beta_x$ and $k_y = 2\pi m/p'_y - 2\pi\beta_y$, $n \in \{0, 1, \dots, p'_x - 1\}$, $m \in \{0, 1, \dots, p'_y - 1\}$ for all choices of β_x and β_y such that $p'_x \beta_x + p'_y \beta_y = \beta''$, where β_x is an integer multiple of $1/L_x$ and β_y an integer multiple of $1/L_y$ fulfilling $0 \leq \beta_x < 1/p'_x$ and $0 \leq \beta_y < 1/p'_y$.

Note that if $p'_y = p_y$, this case is already covered by combining the other two cases and does therefore not correspond to an additional constraint.

If a reference state $|\{\mathbf{r}_k\}, \{\alpha_k\}; \mathcal{A}\rangle$ fulfills multiple of the conditions mentioned above ($p_x < L_x$, $p_y < L_y$, $p'_y < p_y$), the sheet amplitude vectors \mathcal{A} have to be chosen to be eigenvectors of all the corresponding operators; the allowed momenta for the momentum states $|\{\mathbf{r}_k\}, \{\alpha_k\}; \mathbf{k}; \mathcal{A}\rangle$ are then restricted by all the respective constraints given by (A.5), (A.14) and/or (A.15). Due to the commutation relation $[T_x, T_y] = 0$, we can indeed choose the sheet amplitude vectors to be simultaneous eigenstates of the relevant operators.

When constructing the momentum states $|\{\mathbf{r}_k\}, \{\alpha_k\}; \mathbf{k}; \mathcal{A}\rangle$, one should first identify the periodicities p_x , p_y , p'_x and p'_y of each anyon configuration and identify which of the three constraints discussed above are to be applied. Finally, one has to choose the sheet amplitude vectors to be (simultaneous) eigenstates of the relevant operators and choose the allowed momenta accordingly. Different sheet amplitude vectors to the same anyon configuration have to be orthogonal.

One can numerically find simultaneous eigenvectors of two operators by using the Zassenhaus algorithm [48, 49], which computes a basis for the sum and the intersection of two subspaces of a vectorspace. In particular, we are interested in the intersection of the subspace to a certain eigenvalue of one operator with the subspace to some other eigenvalue of another operator, where the vectorspace is the sheet space. All the vectors in the intersection are therefore simultaneous eigenvectors of the two operators to the associated eigenvalues. If for an anyon configuration e.g. $p_x < L_x$, $p_y < L_y$ and $p'_y = p_y$, we can find the eigenvectors and therefore the subspaces of $\prod_{i=0}^{n_x(p_x)-1} T_x^s(\{\alpha_k\}^i)$ and $(T_y^s)^{p_y}$ by diagonalization and then find the simultaneous eigenvectors in the intersections of all the combinations of subspaces of the two operators.

When identifying the different subspaces, it is very important to account for the numerical precision: In the diagonalization process, one might obtain two slightly different eigenvalues which in fact would agree with each other in an exact treatment. Such cases can be easily identified since we know the typical magnitude of numerical errors and already discussed the form of all possible eigenvalues to the relevant operators. We thus simply have to combine the corresponding eigenvectors in order to form to correct (higher dimensional) subspaces. Otherwise, one might not obtain the correct number of simultaneous eigenstates in the intersections.

The simultaneous eigenvectors of three operators can be found by applying the Zassenhaus algorithm a second time, where one subspace corresponds to an intersection of two subspaces of the first two operators, the other subspace corresponds to a subspace of the third operator, i.e., one subspace already corresponds to an eigenvalue pair of the first two operators, the second subspace to an eigenvalue of the third operator. With this knowledge, it is possible to construct all allowed momentum states $|\{\mathbf{r}_k\}, \{\alpha_k\}; \mathbf{k}; \mathcal{A}\rangle$ to every anyon configuration.

In order to show that the states $|\{\mathbf{r}_k\}, \{\alpha_k\}; \mathbf{k}; \mathcal{A}\rangle$ also form a basis of the Hilbert space, we first show the orthogonality, similar to the procedure for the momentum state in x -direction $|\{\mathbf{r}_k\}, \{\alpha_k\}; k_x; \mathcal{A}\rangle$. It is again obvious that momentum states generated by reference states whose anyon configurations can not be made to agree with each other by applying T_x - and T_y -operators are orthogonal. Thus, we assume in the following that the considered momentum states are generated by the same reference state. The overlap between two such momentum

states with momenta $\mathbf{k} = (k_x, k_y)$ and $\mathbf{k}' = (k'_x, k'_y)$ is given by

$$\begin{aligned}
 & \langle \{\mathbf{r}_k\}, \{\alpha_k\}; \mathbf{k}' | \mathcal{A}' | \{\mathbf{r}_k\}, \{\alpha_k\}; \mathbf{k}; \mathcal{A} \rangle \\
 &= \frac{1}{N_{xy}} \sum_{j,j'=0}^{L_x-1} \sum_{l,l'=0}^{L_y-1} e^{i(jk_x-j'k'_x)+i(lk_y-l'k'_y)} \langle \{\mathbf{r}_k\}, \{\alpha_k\}; \mathcal{A}' | T_y^{l-l'} T_x^{j-j'} | \{\mathbf{r}_k\}, \{\alpha_k\}; \mathcal{A} \rangle \\
 &= \frac{L_x^2 L_y^2 / p_x p'_y}{N_{xy}} \delta_{k_x k'_x} \delta_{k_y k'_y} \langle \mathcal{A}' | \mathcal{A} \rangle.
 \end{aligned} \tag{A.16}$$

One can carry out a calculation similar to the one in (A.6): Using the definition of the translation operators and the relations (A.5), (A.14) and (A.15), the sums over j, j' and l, l' yield $\delta_{k_x k'_x} L_x^2 / p_x$ and $\delta_{k_y k'_y} L_y^2 / p'_y$ and the sheet amplitude vectors' scalar product. p'_y appears instead of p_y since in the definition of the mixed periodicity in (A.10), we first minimize w.r.t. the translations in y -direction. The momentum states $|\{\mathbf{r}_k\}, \{\alpha_k\}; \mathbf{k}; \mathcal{A}\rangle$ are thus orthonormal.

There is also an argument that the total number of these momentum states agrees with the total number of basis states $|\{\mathbf{r}_k\}, \{\alpha_k\}; \mathcal{A}\rangle$. For a given anyon configuration, each combination of translations in x - and y -direction is also contained in the latter basis, where the number of translations in x - and y -direction have to be smaller than p_x and p'_y , respectively, to avoid double counting. If we now use this very anyon configuration (or an arbitrary translation of it) as reference state to generate all allowed momentum states, it can be seen from the constraints (A.5), (A.14) and (A.15) that exactly $p_x p'_y$ momentum states with distinct momentum quantum numbers can be constructed, which agrees with the number of states $|\{\mathbf{r}_k\}, \{\alpha_k\}; \mathcal{A}\rangle$ that have this anyon configuration modulo translations. A similar result is obtained when also considering the sheet amplitude vectors. As T_x and T_y are unitary and commute, these operators can be simultaneously diagonalized in sheet space. It follows that the number of (physical) eigenvectors agrees with the dimension of the physical sheet space and thus also with the number of states $|\{\mathbf{r}_k\}, \{\alpha_k\}; \mathcal{A}\rangle$. Due to the unitarity of T_x and T_y , it is also clear that the number of (physical) sheet amplitude vectors is the same for each translation of the anyon configuration and thus, the total number of momentum states $|\{\mathbf{r}_k\}, \{\alpha_k\}; \mathbf{k}; \mathcal{A}\rangle$ is independent of the choices of reference states and agrees with the total number of basis states $|\{\mathbf{r}_k\}, \{\alpha_k\}; \mathcal{A}\rangle$. Using this result and the orthonormality, it is shown that the momentum states with momentum in x - and y -direction indeed form another basis of the Hilbert space.

B. Equivalence of the Generalized Algorithm to the Algorithm in Section 2.1 for Abelian Anyons

Here, the equivalence of the generalized algorithm presented in section 4.2 to the algorithm for abelian anyons in [17] that was discussed in section 2.1 is shown. The latter simulates N abelian anyons a torus, where all anyons possess the same charge and a phase of θ is acquired upon exchanging two of them, with $e^{i2\theta N} = 1$. Translating an anyon around the torus along a non-contractible loop is modelled using two $M \times M$ matrices, where M is the smallest positive integer fulfilling $e^{i2\theta M} = 1$, i.e. $\theta = \pi p/M$ with p and M being coprime integers. We show that these matrices are also obtained from the generalized algorithm introduced in this thesis. Furthermore, all the phases acquired due to the anyons moving on the lattice (without being dragged along a non-contractible loop) are shown to be the same, proving that the presented algorithm can indeed be understood as a generalization to arbitrary abelian and non-abelian anyon models.

First, we have to take a look at the anyonic charges of the given anyon model: From the string rules in [17] / section 2.1.2, one can see that when fusing two anyons and exchanging this fusion product with another anyon, a phase of 2θ is picked up since the phases associated to the fusion product's string correspond to twice the phases associated to an initial anyon's string. Thus, M anyons fuse to the vacuum charge and as this is the minimal number of anyons to do so, there are overall M anyonic charges in the anyon model which will be referred to as $[a]_M$, $[a]_M \in \{0, \dots, M-1\}$, where $[a]_M = 0$ refers to the vacuum charge and $[a]_M = 1$ is the charge of the anyons being simulated on the lattice. Note that for convenience, the notation of the vacuum charge here differs from the one used in the main part of the thesis. Due to the abelian nature, we can already see that there are M sheets in total, agreeing with the dimensionality of the $M \times M$ matrices in equation (2.9). For the description of the anyon model to be discussed, we follow the relevant part in Bonderson's PhD thesis [50]. In the above notation, the fusion rules are given by

$$[a]_M \times [b]_M = [a + b]_M, \quad (\text{B.1})$$

where sums of anyon charges are always taken mod M . From now on, the brackets $[]_M$ will only be written where they are not obvious. The F - and R -moves are given by

$$\left[F_{a+b+c}^{a,b,c} \right]_{a+b,b+c} = e^{i \frac{\pi}{M} a([b]_M + [c]_M - [b+c]_M)} \quad \text{and} \quad R_{a+b}^{a,b} = e^{i\theta ab}, \quad (\text{B.2})$$

where it was assumed that the anyon model containing the appropriate R -moves is $\mathbb{Z}_M^{n+1/2}$ for some $n \in \{0, 1, \dots, M-1\}$ and M even. The other abelian anyon models that include M distinct charges, \mathbb{Z}_M^n (with $n \in \{0, 1, \dots, M-1\}$), have trivial F -moves and will be discussed later on. As all of these anyon models feature different R -moves, the correct anyon model containing the same anyons as simulated by the algorithm for abelian anyons, i.e. with $R_{a+b}^{a,b} = e^{i\theta ab}$, is unique, given the anyonic charge 1 indeed corresponds to the simulated anyons. Finally, we note that the entries of the modular S -matrix (which is the punctured torus S -matrix $S^{(z)}$ for $z = 0$) are given by

$$S_{a,b} = \frac{1}{\sqrt{M}} e^{i2\theta ab}. \quad (\text{B.3})$$

In order to show the equivalence to the algorithm for abelian anyons, we show that the matrices τ_i , ρ_i and σ_j with $i \in \{1, \dots, N\}$, $j \in \{1, \dots, N-1\}$ naturally arise from the rules in our generalized algorithm. Consider a state with N anyons in which the coordinates of the i -th anyon are given by x_i and y_i and fulfil $x_{i+1} > x_i$ and $y_{i+1} > y_i$ for $i = 1, \dots, N-1$ (Fig. 1 in [17] and Fig. 2.1 in section 2.1). Here, we of course assume that the lattice is big enough. The operators corresponding to τ_i and ρ_i drag the i -th anyon along a non-contractible loop in positive x - and y -direction (without any translations in the perpendicular direction), respectively. σ_j corresponds to a counter-clockwise exchange of the j -th and $(j+1)$ -th anyon.

For the latter operation, no cut has to be crossed, i.e., the corresponding operator according to the first rule in Fig. 4.3 is simply given by

$$\left[B_{j+1}^{j-1,1,1} \right]_{j,j} \mathbb{1}_M = R_2^{1,1} \mathbb{1}_M = e^{i\theta} \mathbb{1}_M, \quad (\text{B.4})$$

in agreement with (2.5). Using this result and the rules in Figs. 4.4 and 4.5, it can be seen that $\tau_{j+1} = e^{-i2\theta} \tau_j = e^{-i2\theta j} \tau_1$ and $\rho_{j+1} = e^{i2\theta} \rho_j = e^{i2\theta j} \rho_1$, which also follows from the more general relations $\tau_{j+1} = \sigma_j^{-1} \tau_j \sigma_j^{-1}$ and $\rho_{j+1} = \sigma_j \rho_j \sigma_j$ [17, 21]. τ_1 can be computed by using Fig. 4.4 and (4.9):

$$\begin{aligned} (\tau_1)_{[a-1]_M, a} &= e^{i\theta(N-1)} \left[F_{[-a]_M}^{M-1,1,[-a]_M} \right]_{0,[-a+1]_M} \left[F_{[-a+1]_M}^{1,M-1,[-a+1]_M} \right]_{[-a]_M,0}^{-1} \\ &\quad \times \prod_{j=0}^{N-4} \left[F_{[N-j]_M}^{1,[N-2-j]_M,1} \right]_{[N-1-j]_M,[N-1-j]_M}^{-1} \left[F_{[3]_M}^{1,1,1} \right]_{[2]_M,[2]_M}^{-1} \\ &= e^{i\theta(N-1)} e^{i\frac{\pi}{M} \{M([-a]_M - [-a+1]_M) - (2-[2]_M) - \sum_{j=0}^{N-4} ([N-2-j]_M + 1 - [N-1-j]_M)\}} \\ &= e^{i\theta(N-1)} e^{i\pi(1 + \lfloor (N-3)/M \rfloor)} e^{-i\theta(2-[2]_M)}, \end{aligned} \quad (\text{B.5})$$

where $e^{i\theta(N-1)}$ originates from the braid operators B and $N > 2$ and $M \geq 2$ was assumed. It was further used that $[N]_M = 0$. The contribution $([-a]_M - [-a+1]_M)$ is either -1 or $M-1$ and due to M being even, both cases yield the same result. In the intermediate step, the sum in the exponent was found to equal $-M \lfloor (N-3)/M \rfloor$, where $\lfloor x \rfloor$ denotes the largest integer smaller than or equal to x . In the initial state, charge a is moving along the non-contractible loop, whereas in the final state, that charge is $[a-1]_M$. All other entries are zero, i.e. τ_1 is a

$M \times M$ matrix that is given by

$$\tau_1 = e^{i\theta(N-1)} e^{i\pi(1+\lfloor(N-3)/M\rfloor)} e^{-i\theta(2-\lfloor 2 \rfloor_M)} \begin{pmatrix} 0 & 1 & & \\ \vdots & 0 & \ddots & \\ 0 & & \ddots & 1 \\ 1 & 0 & \dots & 0 \end{pmatrix} \quad (\text{B.6})$$

For $M = N = 2$, the prefactor is given by $-e^{i\theta}$ and thus also agrees with the above result. By using Fig. 4.5, ρ_1 is computed to be

$$\begin{aligned} (\rho_1)_{jk} &= e^{-i2\theta(N-1)} \frac{1}{M} \sum_{a,b} S_{ja}^{(0)\dagger} (\tau_1)_{ab} S_{bk}^{(0)} \\ &= e^{-i\theta(N-1)} e^{i\pi(1+\lfloor(N-3)/M\rfloor)} e^{-i\theta(2-\lfloor 2 \rfloor_M)} \frac{1}{M} \sum_a e^{-i2\theta ja} e^{i2\theta[a+1]_M k} \\ &= e^{-i\theta(N-1)} e^{i\pi(1+\lfloor(N-3)/M\rfloor)} e^{-i\theta(2-\lfloor 2 \rfloor_M)} \frac{1}{M} \sum_a e^{i2\theta(k-j)a} e^{i2\theta k(1-M\lfloor(a+1)/M\rfloor)} \\ &= e^{-i\theta(N-1)} e^{i\pi(1+\lfloor(N-3)/M\rfloor)} e^{-i\theta(2-\lfloor 2 \rfloor_M)} e^{i2\theta k} \delta_{jk}, \end{aligned} \quad (\text{B.7})$$

where we used the fact that the translation across cut A can be obtained by transforming the translation across cut B via $S^{(z)}$ ($z = 0$ for abelian anyons). The prefactor $e^{-i2\theta(N-1)}$ compensates the factor $e^{i\theta(N-1)}$ in (B.5) and accounts for the other braids according to (4.5). Further, it was used that $2\theta M = 2\pi$ and $[a+1]_M = a+1 - M\lfloor(a+1)/M\rfloor$, which is straight forward to verify. This result is again valid for $N \geq 2$ and $M \geq 2$. Written as matrix, ρ_1 takes the form

$$\rho_1 = e^{-i\theta(N-1)} e^{i\pi(1+\lfloor(N-3)/M\rfloor)} e^{-i\theta(2-\lfloor 2 \rfloor_M)} \begin{pmatrix} 1 & & & \\ & e^{i2\theta} & & \\ & & \ddots & \\ & & & e^{i2\theta(M-1)} \end{pmatrix}. \quad (\text{B.8})$$

The two matrices (B.6) and (B.8) agree with the respective matrices in (2.9), except for the prefactor. This is however of no concern as we can always choose to introduce fluxes in both directions that compensate the differences in phase.

In addition to the operators τ_i , ρ_i and σ_j , for the algorithm simulating abelian anyons, one final rule is needed. If an anyon is translated across cut A , the wave function picks up an additional factor of $e^{i\theta}$ for each anyon located in the same column as the anyon that is translated. This relative phase is naturally contained in the rule from Fig. 4.5 in our algorithm. It thus follows that our generalized algorithm agrees with the one for abelian anyons for the an accordingly chosen anyon model.

Until now, we assumed that the appropriate abelian anyon model is given by $\mathbb{Z}_M^{n+1/2}$ for some n . However, if the appropriate anyon model turns out to be \mathbb{Z}_M^n for some n , a very similar result is obtained: Due to the F -moves being trivial, the prefactor in (B.6) is changed to $e^{i\theta(N-1)}$ and

the prefactor in (B.8) becomes $e^{-i\theta(N-1)}$. All other results remain unaffected. This implies that also for these models, the two matrices can be made to agree with those in (2.9) by introducing fluxes.

With this, it is shown that the newly developed, generalized algorithm simplifies to the algorithm discussed in [17] and section 2.1 for an appropriately chosen abelian anyon model, implying that it is indeed a generalization to arbitrary abelian and non-abelian anyon models. It is to be stressed that the two algorithms use different conventions for external fluxes, which has to be kept in mind when verifying their equivalence for abelian anyons numerically.

We note again that argueably, our approach seems to be more natural since the phases merely arise from braids and the anyon model's basic data, i.e. there are no artificially added contributions. In [17] on the other hand, the fluxes are fixed by the condition that dragging the first particle around either direction does only yield non-trivial phases for non-zero fluxes (for ρ_1 , this is of course only true on one of the sheets), see (2.9). The reason behind this convention is a generalization from anyons on an annulus [16]. For us, it is questionable to what extent this generalization does actually apply to the torus.

C. Derivation of Equation (6.9)

The starting point of the derivation is the particle-particle distance dependent parts of the two-particle wave functions, $\psi(r)$ and $\bar{\psi}(r)$, which correspond to the solutions to the Schrödinger equations (2.30) for interactions of the form $V(r)$ and $V(r) + P(r)$ that are given by

$$r^2 \bar{\psi}(r) \left(-\frac{d^2}{dr^2} - \frac{\beta}{r} \frac{d}{dr} + V(r) - \Omega \right) \psi(r) = 0 \quad (\text{C.1})$$

$$\text{and } r^2 \psi(r) \left(-\frac{d^2}{dr^2} - \frac{\beta}{r} \frac{d}{dr} + V(r) + P(r) - \bar{\Omega} \right) \bar{\psi}(r) = 0. \quad (\text{C.2})$$

Here, the potentials and eigenenergies Ω and $\bar{\Omega}$ have been renormalized by \hbar^2/m (or alternatively, those quantities can be thought of as being set to unity like in equation (6.8)) and additional factors of $r^2 \bar{\psi}(r)$ and $r^2 \psi(r)$ have been multiplied from the left, respectively. Further, we suppressed the energy dependency of the wave functions for convenience and the parameter β was introduced in order to adjust the dimension in which the Schrödinger equations hold, with $\beta = 1$ for 2D and $\beta = 2$ for 3D.

Integrating equation (C.1) from r' to ∞ yields the relation

$$\begin{aligned} \int_{r'}^{\infty} dr'' (r'')^2 \bar{\psi}(r'') \psi(r'') (V(r'') - \Omega) &= -(r')^2 \bar{\psi}(r') \frac{d}{dr'} \psi(r') \\ &+ \int_{r'}^{\infty} dr'' \left\{ (\beta - 2) r'' \bar{\psi}(r'') \frac{d}{dr''} \psi(r'') - (r'')^2 \left(\frac{d}{dr''} \bar{\psi}(r'') \right) \left(\frac{d}{dr''} \psi(r'') \right) \right\}. \end{aligned} \quad (\text{C.3})$$

A similar result is obtained after integrating equation (C.2) from r' to ∞ , which also arises from equation (C.3) via the substitutions $\psi(r'') \rightarrow \bar{\psi}(r'')$, $\bar{\psi}(r'') \rightarrow \psi(r'')$ and $V(r'') - \Omega \rightarrow V(r'') + P(r'') - \bar{\Omega}$. Subtracting equation (C.3) from this counterpart yields

$$\begin{aligned} \int_{r'}^{\infty} dr'' (r'')^2 \bar{\psi}(r'') \psi(r'') (P(r'') + \Omega - \bar{\Omega}) &= (r')^2 \bar{\psi}(r') \frac{d}{dr'} \psi(r') - (r')^2 \psi(r') \frac{d}{dr'} \bar{\psi}(r') \\ &+ (2 - \beta) \int_{r'}^{\infty} dr'' r'' \left(\bar{\psi}(r'') \frac{d}{dr''} \psi(r'') - \psi(r'') \frac{d}{dr''} \bar{\psi}(r'') \right). \end{aligned} \quad (\text{C.4})$$

Then, dividing by $(r'\psi(r'))^2$ and integrating both sides from r to ∞ results in

$$\begin{aligned} \left[-\frac{\bar{\psi}(r')}{\psi(r')} \right]_{r'=r}^{r'=\infty} &= \int_r^\infty \frac{dr'}{(r'\psi(r'))^2} \int_{r'}^\infty dr'' (r''\psi(r''))^2 (P(r'') + \Omega - \bar{\Omega}) \frac{\bar{\psi}(r'')}{\psi(r'')} \\ &\quad + (2 - \beta) \int_r^\infty \frac{dr'}{(r'\psi(r'))^2} \int_{r'}^\infty dr'' r''\psi(r'')^2 \frac{d}{dr''} \frac{\bar{\psi}(r'')}{\psi(r'')}. \end{aligned} \quad (\text{C.5})$$

In the final step, the energies are set to be equal $\Omega = \bar{\Omega}$ and $\lim_{r \rightarrow \infty} \bar{\psi}(r)/\psi(r) = 1$ is used, assuming that the leading order of the wave function in the large r limit is not affected by the interaction $P(r)$ and therefore

$$\begin{aligned} \frac{\bar{\psi}(r)}{\psi(r)} &= 1 + \int_r^\infty \frac{dr'}{(r'\psi(r'))^2} \int_{r'}^\infty dr'' (r''\psi(r''))^2 P(r'') \frac{\bar{\psi}(r'')}{\psi(r'')} \\ &\quad + (2 - \beta) \int_r^\infty \frac{dr'}{(r'\psi(r'))^2} \int_{r'}^\infty dr'' r''\psi(r'')^2 \frac{d}{dr''} \frac{\bar{\psi}(r'')}{\psi(r'')}. \end{aligned} \quad (\text{C.6})$$

In 3D (i.e. $\beta = 2$), equation (C.6) simplifies to the formula used in Wigner's argument [43] and in the 2D case (i.e. $\beta = 1$), the formula used in the discussion in section 6.2.2 is obtained, where the above assumption $\lim_{r \rightarrow \infty} \bar{\psi}(r)/\psi(r) = 1$ is also discussed.

D. Changes in the Asymptotic Behavior Due to Interactions of the Form $U/r^{2+\epsilon}$

Applying an interaction $U/r^{2+\epsilon}$ with $\epsilon > 0$ changes the large r asymptotics of the wave function. The aim of this section is to compute the order at which such changes occur for the first time. Starting point is the Schrödinger equation (6.8) with $l = 0$ and suppressed Ω -dependency in the wave function for convenience:

$$\left(-\frac{d^2}{dr^2} - \frac{1}{r} \frac{d}{dr} + \frac{\alpha^2}{r^2} + \frac{U}{r^{2+\epsilon}} - \Omega\right) \psi(r) = 0. \quad (\text{D.1})$$

The leading order for large r of the solution for $U = 0$ is given by [46]

$$\psi(r) \propto \frac{e^{i\sqrt{\Omega}r}}{\sqrt{r}} \left(1 + \mathcal{O}(r^{-1})\right). \quad (\text{D.2})$$

The second, linear independent solution to (D.1) is the complex conjugate of (D.2). Since for $r \rightarrow \infty$, the term $\propto r^{-2}$ dominates over the interaction $\propto r^{-2-\epsilon}$ for $\epsilon > 0$ in the Schrödinger equation, the leading order of the asymptotic expansion is not expected to change. Thus, an iterative ansatz will be used in order to find the first corrections to the leading order. Assuming that the solution takes the form

$$\psi(r) \propto \frac{e^{i\sqrt{\Omega}r}}{\sqrt{r}} f(r), \quad (\text{D.3})$$

an equation for $f(r)$ can be derived by plugging (D.3) into (D.1). Using

$$\frac{d}{dr} \frac{e^{i\sqrt{\Omega}r}}{\sqrt{r}} f(r) = \frac{e^{i\sqrt{\Omega}r}}{\sqrt{r}} \left(i\sqrt{\Omega} f(r) - \frac{1}{2} \frac{f(r)}{r} + f'(r) \right) \quad \text{and} \quad (\text{D.4})$$

$$\frac{d^2}{dr^2} \frac{e^{i\sqrt{\Omega}r}}{\sqrt{r}} f(r) = \frac{e^{i\sqrt{\Omega}r}}{\sqrt{r}} \left\{ \left(-\Omega - \frac{i\sqrt{\Omega}}{r} + \frac{3}{4} \frac{1}{r^2} \right) f(r) + \left(2i\sqrt{\Omega} - \frac{1}{r} \right) f'(r) + f''(r) \right\}, \quad (\text{D.5})$$

the constraint for $f(r)$ can be computed:

$$\left(\frac{\alpha^2 - \frac{1}{4}}{r^2} + \frac{U}{r^{2+\epsilon}} \right) f(r) - 2i\sqrt{\Omega} f'(r) - f''(r) = 0. \quad (\text{D.6})$$

For the iterative procedure, $f(r) = 1 + cr^{-\gamma}$ is plugged into (D.6) and only orders in $1/r$ up to the one fixing the parameters c and γ are considered. Higher orders will successively be dealt with if one chooses to expand $f(r)$ further, i.e. $f(r) = 1 + cr^{-\gamma} + dr^{-\delta}$, and repeating the procedure.

In principle, there is no need to compute the parameters c and γ before adding additional terms. But as in this case the calculations become messier, the iterative manner is used here. For $f(r) = 1 + cr^{-\gamma}$, equation (D.6) can be written as

$$\frac{\alpha^2 - \frac{1}{4}}{r^2} + \frac{U}{r^{2+\epsilon}} + c\frac{\alpha^2 - \frac{1}{4}}{r^{2+\gamma}} + c\frac{U}{r^{2+\epsilon+\gamma}} + 2i\sqrt{\Omega}\frac{c\gamma}{r^{1+\gamma}} - \frac{c\gamma(\gamma+1)}{r^{2+\gamma}} = 0 \quad (\text{D.7})$$

and after discarding all contributions that are not needed to determine the parameters c and γ

$$\frac{\alpha^2 - \frac{1}{4}}{r^2} + 2i\sqrt{\Omega}\frac{c\gamma}{r^{1+\gamma}} = 0 \quad (\text{D.8})$$

is obtained. Thus, the parameters are $\gamma = 1$ and $c = i(\alpha^2 - 1/4)/2\sqrt{\Omega}$. This result agrees with the first correction of the asymptotic expansion for $U = 0$ as neither γ nor c depend on U or ϵ . Therefore, the change in the asymptotic behavior appears at higher orders.

Expanding $f(r)$ further, $f(r) = 1 + cr^{-\gamma} + dr^{-\delta}$, yields the condition

$$\frac{U}{r^{2+\epsilon}} + \frac{i(\alpha^2 - \frac{1}{4})(\alpha^2 - \frac{9}{4})}{2\sqrt{\Omega}r^3} + \frac{i(\alpha^2 - \frac{1}{4})U}{2\sqrt{\Omega}r^{3+\epsilon}} + d\frac{\alpha^2 - \frac{1}{4}}{r^{2+\delta}} + d\frac{U}{r^{2+\epsilon+\delta}} + 2i\sqrt{\Omega}\frac{d\delta}{r^{1+\delta}} - \frac{d\delta(\delta+1)}{r^{2+\delta}} = 0. \quad (\text{D.9})$$

The relation needed to solve for the newly introduced parameters depends on the choice of ϵ . For $\epsilon < 1$, the relation is

$$\frac{U}{r^{2+\epsilon}} + 2i\sqrt{\Omega}\frac{d\delta}{r^{1+\delta}} = 0 \quad (\text{D.10})$$

and the results are thus $\delta = 1 + \epsilon$ and $d = iU/2\sqrt{\Omega}(1 + \epsilon)$. This is the first order at which deviations from the $U = 0$ asymptotics can be seen. In fact, it is straight forward to see from this approach that also for $\epsilon \geq 1$, the first deviation in $f(r)$ can be observed at the order $\mathcal{O}(r^{-(1+\epsilon)})$.

List of Figures

2.1. Generators $\tilde{\sigma}_i$, $\tilde{\rho}_j$ and $\tilde{\tau}_j$ of $B_N(\mathcal{T})$. The particles are numbered from the left to the right.	4
2.2. Choice of cuts A and B on a lattice containing four anyons numbered from one to four. The phases associated to the anyons' strings are θ for the vertical and 2θ for the horizontal parts.	6
2.3. $\phi_{long}(xL_x, 0)$ and $\tilde{\phi}_{long}(x/L_x, 0)$ as function of x with $U = 1$, $L_x = 40$ and $n = 3$	12
3.1. Torus with the three charges associated to the punctures fusing to charge e which then fuses with the anyonic charge f moving along a non-contractible loop, which is hereby defined to follow the negative x -direction; the black loop being threaded by f hence follows the (positive) y -direction. The fusion order of the charges indicated here is used as the conventional fusion order for braiding.	18
4.1. (a): Choice of cuts A and B on a lattice containing three anyons corresponding to diagram (3.15) if the sheet is chosen accordingly. (b): Choice of fusion order. Anyons with small x -coordinates fuse first; among those with the same x -coordinate, anyons with smaller y -coordinates come first.	23
4.2. Depiction of all allowed fusion diagrams for (a) one Fibonacci anyon and (b)-(d) two Fibonacci anyons.	25
4.3. Illustration of the braid rules for translating anyons in positive x -direction without crossing cut B . The lattice on the left shows an anyon configuration and indicates which anyon is to be translated. On the right, the effect of the translation on the fusion diagram is depicted.	26
4.4. Illustration of the braid rules for translating anyons in positive x -direction across cut B . The lattice on the left shows an anyon configuration and indicates which anyon is to be translated. On the right, the effect of the translation on the fusion diagram is depicted.	31
4.5. Illustration of the braid rules for translating anyons in positive y -direction across cut A . The lattice on the left shows an anyon configuration and indicates which anyon is to be translated. On the right, the effect of the translation on the fusion diagram is depicted.	32
5.1. $P(r)$ for fermions on a 40×2 lattice, HCBs with a rung coupling of $r_\perp = 0.5$ on a 40×2 lattice, semions on a 32×2 lattice and Fibonacci anyons on a 22×2 lattice in the $k_x = k_y = 1$ sector together with the Poisson and GOE distributions.	36

5.2.	Initial ladder configuration for the quench. $N = 4$ particles of type α are localized in the middle of the ladder in a zigzag pattern in order to avoid unnecessary blocking.	37
5.3.	Particle density per rung $\langle n_i(t) \rangle$ for fermions (upper left), HCBs (upper right), semions (lower left) and Fibonacci anyons (lower right) on a 30×2 ladder. Initially, the $N = 4$ particles are localized in the middle of the ladder in a zigzag pattern (see Fig. 5.2), the initial sheet amplitude vector is $\mathcal{A}_i = n_s^{-1/2}(1, 1, \dots, 1)^\top$. For HCBs, the rung coupling was set to $r_\perp = 0.5$	38
5.4.	$\frac{1}{L_x} \sum_i \frac{1}{\bar{n}_i^2 T} \int_0^T dt (\langle n_i(t) \rangle - \bar{n}_i(T_{max}))^2 \approx \Delta(T)$ for fermions, HCBs, semions and Fibonacci anyons on a ladder with $L_x = 22, 26, 30$ and $L_y = 2$. Smaller system sizes correspond to brighter tones. In the initial state, $N = 4$ particles are localized in the middle of the ladder as depicted in Fig. 5.2. The initial sheet amplitude vector is $\mathcal{A}_i = n_s^{-1/2}(1, 1, \dots, 1)^\top$. For HCBs, the rung coupling was set to $r_\perp = 0.5$ again.	39
5.5.	Variance of $\bar{n}_i(T)$ for fermions, HCBs, semions and Fibonacci anyons on a ladder with $L_x = 22, 26, 30$ and $L_y = 2$. Smaller system sizes correspond to brighter tones. In the initial state, $N = 4$ particles are localized in the middle of the ladder as depicted in Fig. 5.2. The initial sheet amplitude vector is $\mathcal{A}_i = n_s^{-1/2}(1, 1, \dots, 1)^\top$. For HCBs, the rung coupling was set to $r_\perp = 0.5$ again.	40
6.1.	Simulated threshold behavior of $S(\mathbf{q} = \mathbf{0}, \omega)$ for non-interacting fermions and semions on a 40×40 lattice and expected threshold behavior at low energies (dashed).	45
6.2.	Simulated threshold behavior of $S(\mathbf{q} = \mathbf{0}, \omega)$ for non-interacting fermions and semions from numerically solving the differential equation and the expected threshold behavior at low energies order (dashed).	46
6.3.	Simulated behavior of $S(\mathbf{q}=\mathbf{0}, \omega)$ for semions with an additional interaction Ur^{-2} for $U = 0, 0.25, 0.5, 1$ on a 40×40 lattice and the corresponding expected threshold behaviors (dashed).	48
6.4.	Simulated behavior of $S(\mathbf{q}=\mathbf{0}, \omega)$ for semions with an additional interaction Ur^{-2} for $U = 0, 0.25, 0.5, 1$ obtained by numerically solving the Schrödinger equation and the corresponding expected threshold behaviors (dashed).	49
6.5.	Simulated behavior of $S(\mathbf{q}=\mathbf{0}, \omega)$ for semions with an additional interaction Ur^{-3} for $U = 0, 0.25, 0.5, 1$ on a 40×40 lattice, which is expected to agree with the non-interacting threshold behavior (dashed) in the low-energy limit.	50
6.6.	Simulated behavior of $S(\mathbf{q}=\mathbf{0}, \omega)$ for semions with an additional interaction Ur^{-3} for $U = 0, 0.25, 0.5, 1$ obtained by numerically solving the Schrödinger equation, which is expected to agree with the non-interacting threshold behavior (dashed) in the low-energy limit.	51
6.7.	Simulated threshold behavior of $S(\mathbf{q}=\mathbf{0}, \omega)$ for semions with an additional interaction Ur^{-1} for $U = 0, 0.25, 0.5, 1$ on a 40×40 lattice, which is expected to deviate from the non-interacting behavior (dashed) in the low-energy limit.	53

6.8. Simulated threshold behavior of $S(\mathbf{q}=\mathbf{0}, \omega)$ for semions with an additional interaction Ur^{-1} for $U = 0, 0.25, 0.5, 1$ obtained by numerically solving the Schrödinger equation, which is expected to deviate from the non-interacting behavior (dashed) in the low-energy limit.	54
6.9. Deviation of the local energy dependence from the non-interacting expectation a_0 (dashed), $\text{dln}(S(\mathbf{q}=\mathbf{0}, \omega))/\text{dln}(\omega) - a_0$, for semions ($a_0 = 0.5$) with interaction Ur^{-1} , $U = 0.001, 0.005, 0.01$, obtained from numerically solving the Schrödinger equation and taking the mentioned derivative.	55
6.10. $\frac{\text{dln}(S(\mathbf{q}=\mathbf{0}, \omega))}{\text{dln}(\omega)} - a_0 = \Delta$ for $\Delta = 0$ and $ \Delta \leq 0.025, 0.05$ as function of U for fermions (upper plot) and semions (lower plot) interacting with Ur^{-1} , obtained from numerically solving the Schrödinger equation and analyzing the mentioned derivative.	56
6.11. Simulated threshold behavior of $S(\mathbf{q}=\mathbf{0}, \omega)$ for non-interacting Fibonacci anyons on a 40×40 lattice. The threshold behavior was found to agree with $\omega^{11/15}$ for the sheet distributions of $O(\mathbf{R}) \psi_i\rangle$ being $\mathcal{A}_i = (1, 1, 1)^\top/\sqrt{3}$. For $\mathcal{A}'_i = (1, i, 0)^\top/\sqrt{2}$, it agrees with $\alpha' = 4/5$	58

References

- [1] C. Nayak, S. H. Simon, A. Stern, M. Freedman, and S. Das Sarma, *Rev. Mod. Phys.* **80**, 1083 (2008).
- [2] Y.-S. Wu, *Phys. Rev. Lett.* **52**, 2103 (1984).
- [3] B. Field and T. Simula, *Quantum Science and Technology* **3**, 045004 (2018).
- [4] R. S. K. Mong, D. J. Clarke, J. Alicea, N. H. Lindner, P. Fendley, C. Nayak, Y. Oreg, A. Stern, E. Berg, K. Shtengel, and M. P. A. Fisher, *Phys. Rev. X* **4**, 011036 (2014).
- [5] A. Kitaev, *Annals of Physics* **303**, 2 (2003).
- [6] L. Hormozi, G. Zikos, N. E. Bonesteel, and S. H. Simon, *Phys. Rev. B* **75**, 165310 (2007).
- [7] S. Trebst, M. Troyer, Z. Wang, and A. W. W. Ludwig, *Progress of Theoretical Physics Supplement* **176**, 384 (2008).
- [8] N. E. Bonesteel, L. Hormozi, G. Zikos, and S. H. Simon, *Phys. Rev. Lett.* **95**, 140503 (2005).
- [9] M. H. Freedman, M. J. Larsen, and Z. Wang, *Communications in Mathematical Physics* **228**, 177 (2002).
- [10] A. Feiguin, S. Trebst, A. W. W. Ludwig, M. Troyer, A. Kitaev, Z. Wang, and M. H. Freedman, *Phys. Rev. Lett.* **98**, 160409 (2007).
- [11] J. Engquist, *Nuclear Physics B* **816**, 356 (2009).
- [12] S. Trebst, E. Ardonne, A. Feiguin, D. A. Huse, A. W. W. Ludwig, and M. Troyer, *Phys. Rev. Lett.* **101**, 050401 (2008).
- [13] A. W. W. Ludwig, D. Poilblanc, S. Trebst, and M. Troyer, *New Journal of Physics* **13**, 045014 (2011).
- [14] E. Ardonne, J. Gukelberger, A. W. W. Ludwig, S. Trebst, and M. Troyer, *New Journal of Physics* **13**, 045006 (2011).
- [15] R. N. C. Pfeifer, P. Corboz, O. Buerschaper, M. Aguado, M. Troyer, and G. Vidal, *Phys. Rev. B* **82**, 115126 (2010).
- [16] Y. Hatsugai, M. Kohmoto, and Y.-S. Wu, *Phys. Rev. B* **43**, 2661 (1991).
- [17] Y. Hatsugai, M. Kohmoto, and Y.-S. Wu, *Phys. Rev. B* **43**, 10761 (1991).
- [18] C. Kallin, *Phys. Rev. B* **48**, 13742 (1993).
- [19] S. Singh, R. N. C. Pfeifer, G. Vidal, and G. K. Brennen, *Phys. Rev. B* **89**, 075112 (2014).

- [20] S. C. Morampudi, A. M. Turner, F. Pollmann, and F. Wilczek, *Phys. Rev. Lett.* **118**, 227201 (2017).
- [21] T. Einarsson, *Phys. Rev. Lett.* **64**, 1995 (1990).
- [22] A. Bernevig and T. Neupert, *Topological superconductors and category theory*, (2015)
- [23] H. Reid, *18.330 lecture notes: ewald summation*, Apr. 2014.
- [24] J. J. Benedetto and G. Zimmermann, *Journal of Fourier Analysis and Applications* **3**, 505 (1997).
- [25] F. Wilczek, *Phys. Rev. Lett.* **49**, 957 (1982).
- [26] D. P. Arovas, R. Schrieffer, F. Wilczek, and A. Zee, *Nuclear Physics B* **251**, 117 (1985).
- [27] P. Bonderson, *Physical Review Research* **3**, 033110 (2021).
- [28] P. Bonderson, K. Shtengel, and J. Slingerland, *Annals of Physics* **323**, 2709 (2008).
- [29] P. Bonderson, C. Knapp, and K. Patel, *Annals of Physics* **385**, 399 (2017).
- [30] A. Kitaev, *Annals of Physics* **321**, January Special Issue, 2 (2006).
- [31] O. Derzhko, *Journal of Physical Studies* **5**, 49 (2001).
- [32] V. Oganesyan and D. A. Huse, *Phys. Rev. B* **75**, 155111 (2007).
- [33] C. Kollath, G. Roux, G. Biroli, and A. M. Läuchli, *Journal of Statistical Mechanics: Theory and Experiment* **2010**, P08011 (2010).
- [34] L. D’Alessio, Y. Kafri, A. Polkovnikov, and M. Rigol, *Advances in Physics* **65**, 239 (2016).
- [35] Y. Y. Atas, E. Bogomolny, O. Giraud, and G. Roux, *Phys. Rev. Lett.* **110**, 084101 (2013).
- [36] R. Steinigeweg, F. Heidrich-Meisner, J. Gemmer, K. Michielsen, and H. De Raedt, *Phys. Rev. B* **90**, 094417 (2014).
- [37] A. Polkovnikov, K. Sengupta, A. Silva, and M. Vengalattore, *Rev. Mod. Phys.* **83**, 863 (2011).
- [38] M. Srednicki, *Journal of Physics A: Mathematical and General* **32**, 1163 (1999).
- [39] S. Goldstein, J. L. Lebowitz, R. Tumulka, and N. Zanghì, *The European Physical Journal H* **35**, 173 (2010).
- [40] M. Rigol and M. Srednicki, *Phys. Rev. Lett.* **108**, 110601 (2012).
- [41] T. M. Wright, M. Rigol, M. J. Davis, and K. V. Kheruntsyan, *Phys. Rev. Lett.* **113**, 050601 (2014).
- [42] V. Zatloukal, L. Lehman, S. Singh, J. K. Pachos, and G. K. Brennen, *Phys. Rev. B* **90**, 134201 (2014).
- [43] E. P. Wigner, *Phys. Rev.* **73**, 1002 (1948).
- [44] “Magnetic neutron scattering”, in *Modern techniques for characterizing magnetic materials*, edited by Y. Zhu (Springer US, Boston, MA, 2005), pp. 3–64.

- [45] K. A. Hallberg, *Phys. Rev. B* **52**, R9827 (1995).
- [46] C. Müller, *Analysis of spherical symmetries in euclidean spaces* (Springer-Verlag New York, 1998).
- [47] B. M. Ayeni, S. Singh, R. N. C. Pfeifer, and G. K. Brennen, *Phys. Rev. B* **93**, 165128 (2016).
- [48] E. M. Luks, F. Rákóczi, and C. R. Wright, *Journal of Symbolic Computation* **23**, 335 (1997).
- [49] G. Fischer, *Lernbuch Lineare Algebra und Analytische Geometrie*, 4. (Springer-Verlag, 2019), pp. 211–214.
- [50] P. H. Bonderson, “Non-abelian anyons and interferometry”, PhD thesis (2007).